

Adjoint-based optimization of thermal components using a CAD-based parametrization Development of methods and application to aerospace-grade heat exchangers

Pai Raikar, P.P.

10.4233/uuid:d3416525-9081-4d9e-890c-90de6b09144d

Publication date

Document Version

Final published version

Citation (APA)
Pai Raikar, P. P. (2025). Adjoint-based optimization of thermal components using a CAD-based parametrization: Development of methods and application to aerospace-grade heat exchangers. [Dissertation (TU Delft), Delft University of Technology]. https://doi.org/10.4233/uuid:d3416525-9081-4d9e-890c-90de6b09144d

Important note

To cite this publication, please use the final published version (if applicable). Please check the document version above.

Copyright
Other than for strictly personal use, it is not permitted to download, forward or distribute the text or part of it, without the consent of the author(s) and/or copyright holder(s), unless the work is under an open content license such as Creative Commons.

Takedown policy

Please contact us and provide details if you believe this document breaches copyrights. We will remove access to the work immediately and investigate your claim.

ADJOINT-BASED OPTIMIZATION OF THERMAL COMPONENTS USING A CAD-BASED PARAMETRIZATION

Development of methods and application to aerospace-grade heat exchangers

ADJOINT-BASED OPTIMIZATION OF THERMAL COMPONENTS USING A CAD-BASED PARAMETRIZATION

DEVELOPMENT OF METHODS AND APPLICATION TO AEROSPACE-GRADE HEAT EXCHANGERS

Dissertation

for the purpose of obtaining the degree of doctor at Delft University of Technology, by the authority of the Rector Magnificus, Prof.dr.ir. T.H.J.J. van der Hagen, chair of the Board for Doctorates, to be defended publicly on Thursday, 13 November 2025 at 10:00 o'clock

by

Praharsh Pravin PAI RAIKAR

This dissertation has been approved by the promotors.

Composition of the doctoral committee:

Rector Magnificus, Chairperson

Dr. ir. M. Pini, Delft University of Technology, *promotor*Dr. C.M. De Servi, Delft University of Technology, *copromotor*

Independent members:

Prof. dr. ir. R. De Breuker, Delft University of Technology

Prof. dr. ir. J.R.R.A. Martins, University of Michigan, United States of America

Prof. dr. ir. T. Verstraete, von Karman Institute, Belgium

Dr. ir. N. Beishuizen,

Bosch thermotechnology, NL / TU Eindhoven, NL

Prof. dr. ir. L.L.M. Veldhuis,

Delft University of Technology, reserve member

Other members:

Dr. ir. N. Anand VITO NV, Belgium

The research presented in this dissertation was funded by VITO NV through project number 2010489.





Copyright © 2025 by Praharsh Pravin Pai Raikar ISBN 978-94-6384-867-1
Cover design by Harsh Kamat
Printed by Haveka B.V.

An electronic version of this dissertation is available at http://repository.tudelft.nl/.



CONTENTS

Su	mma	ary		ix	
Sa	men	vatting	g	хi	
1		Background			
2	2.1 2.2	Introd	tt optimization of multiple heat transfer surfaces luction	22 23 23 24 24 24	
	2.3	2.3.1 2.3.2 2.3.3 2.3.4	surfaces	26 26 27 28 29 31 31 32	
3		Introd Metho 3.2.1	Entropy generation analysis Pitch optimization usions. zation of heat sink fins duction odology Geometry modeler CHT solver	39 39 47 48 50 51	

viii Contents

	3.3	3.3.1 Heat sink geometry	54 54
		3.3.2 Numerical model	54
		3.3.3 Grid independence study and model validation	56
			57
	3.4	Results	58
	3.5	Conclusions	68
			70
		8	70
	App	endix 3.C: Optimization with the CP-LS formulation	72
4	Tow		77
	4.1		78
	4.2	8)	80
	4.3	,	80
		· · · · · · · · · · · · · · · · · · ·	81
			83
		· · · · · · · · · · · · · · · · · · ·	84
	4.4		85
		The state of the s	85
		r r r r r r r r r r r r r r r r r r r	86
		4.4.3 Shape optimization and performance improvements at both con-	
	4.5		89
	4.5	Conclusions	92
5	Con	clusions and Outlook	99
A	Soft	ware 10	05
Ac	knov	dedgements	07
Cı	ırricı	lum Vitæ 10	09
Li	st of]	Publications	11

SUMMARY

Decarbonizing aviation requires the development of novel propulsion systems that would be powered by renewable energy stored in batteries, green hydrogen, and e-SAF (a type of sustainable aviation fuel). To increase the viability of these carbon-neutral solutions, minimizing mission energy consumption will remain the key driver of the design of next-generation aircraft systems and their components. Additionally, increasing importance is placed on thermal energy recovery and thermal management, which necessitates the design of high-performance thermal components, namely heat exchangers and heat sinks

This dissertation documents research on shape optimization using the discrete adjoint method and CAD-based parametrization for the design of aerospace-grade heat exchangers. The main outcome of this work is the development of the optimization framework to concurrently optimize multiple heat transfer surfaces parametrized using a CAD method based on Non-Uniform Rational Basis Splines (NURBS) and the discrete adjoint method in the open-source computational fluid dynamics (CFD) software SU2. The application of the design method is demonstrated for two-dimensional and three-dimensional heat transfer surfaces in configurations representative of aircraft condensers and evaporators, as well as heat sinks for thermal management. In this regard, two formulations of surface sensitivity are proposed such that the resulting optimal solutions can feature identical shapes using averaged sensitivities or non-identical shapes when optimized concurrently, albeit independently. Additionally, the feasibility of integrating the CFD-based method in system-level design and its potential for enhancing system performance are investigated.

The results obtained using the design method show that the application of this framework can achieve geometries of thermal components with reduced pressure drop and enhanced heat transfer coefficient compared to conventional designs. The automated design chain applied to a two-dimensional configuration representing tubular heat exchangers reduced the pressure drop significantly while constraining the heat transfer rate. Using three-dimensional shape optimization of pin-fins with conjugate heat transfer resulted in an unconventional fin shape that led to a simultaneous reduction in total pressure losses and an increase in heat transfer coefficient. These performance improvements of about 20% corresponding to optimal geometries obtained from shape optimization can lead to significant gains in the performance of the system, as demonstrated by its application in the early phase of system-level design reported in this work. Future developments on such a design method have the potential to conceive designs of the next-generation heat exchangers that could be deployed in propulsion systems, enabling carbon-neutral aviation.

SAMENVATTING

Het koolstofvrij maken van de luchtvaart vereist de ontwikkeling van nieuwe propulsiesystemen die worden aangedreven door hernieuwbare energie, opgeslagen in batterijen, groene waterstof en e-SAF (een type duurzame vliegtuigbrandstof). Om de levensvatbaarheid van deze koolstofneutrale oplossingen te vergroten, blijft het minimaliseren van het energieverbruik tijdens de missie de belangrijkste drijfveer bij het ontwerp van de volgende generatie vliegtuigsystemen en hun componenten. Daarnaast groeit het belang van thermische energieterugwinning en thermisch beheer, wat de ontwikkeling van hoogwaardige thermische componenten zoals warmtewisselaars en koellichamen noodzakelijk maakt.

Dit proefschrift documenteert onderzoek naar vormoptimalisatie met behulp van de discrete adjointmethode en CAD-gebaseerde parametrisatie voor het ontwerp van hoogwaardig warmtewisselaars voor de lucht- en ruimtevaart. Het belangrijkste resultaat van dit werk is de ontwikkeling van een optimalisatiekader om gelijktijdig meerdere warmteoverdrachtsoppervlakken te optimaliseren. Deze oppervlakken worden geparametriseerd met een CAD-methode gebaseerd op Non-Uniform Rational Basis Splines (NURBS) en de discretadjointe methode in de open-source computational fluid dynamics (CFD) software SU2. De ontwerpmethode wordt gedemonstreerd voor twee- en driedimensionale warmteoverdrachtsoppervlakken in configuraties die representatief zijn voor vliegtuigcondensors en -verdampers, evenals koellichamen voor thermisch beheer. In dit verband worden twee formuleringen van oppervlaktesensitiviteiten voorgesteld, zodat de resulterende optimale oplossingen identieke vormen kunnen hebben bij gebruik van gemiddelde gevoeligheden, of niet-identieke vormen wanneer ze gelijktijdig, zij het onafhankelijk, worden geoptimaliseerd. Daarnaast wordt de haalbaarheid van de integratie van de op CFD-gebaseerde methode in het systeemontwerp onderzocht, evenals het potentieel ervan voor het verbeteren van de systeemprestaties.

De resultaten van de ontwerpmethode laten zien dat dit kader kan leiden tot thermische componenten met een lagere drukval en een hogere warmteoverdrachtscoëfficiënt dan conventionele ontwerpen. De geautomatiseerde ontwerpketen, toegepast op een tweedimensionale configuratie van buiswarmtewisselaars, vermindert de drukval aanzienlijk, terwijl de warmteoverdracht als beperking behouden bleef. Het gebruik van driedimensionale vormoptimalisatie van pin-fins met geconjugeerde warmteoverdracht resulteerde in een onconventionele vinvorm die zowel de totale drukverliezen verminderde als de warmteoverdrachtscoëfficiënt verhoogde. De prestatieverbeteringen van ongeveer 20%, behaald met de (optimale geometrieën uit de) vormoptimalisatie kunnen aanzienlijke winsten in systeemprestatie opleveren, indien toegepast in de vroege fase van het systeemontwerp. Toekomstige ontwikkelingen van deze ontwerpmethode bieden het potentieel om ontwerpen te realiseren voor de volgende generatie warmtewisselaars in voortstuwingssystemen en daarmee bij te dragen aan koolstofneutrale luchtvaart.

Introduction

1.1. BACKGROUND

Decarbonizing aviation is challenging [1]: unlike other sectors where techno-economically viable solutions based on renewable energy are already available, technical options for eliminating carbon emissions from aviation remain absent or are still in the early stages of development. This continued dependence on fossil fuels is primarily driven by the need to minimize weight and volume onboard aircraft, which demands the adoption of fuels of high gravimetric and volumetric energy density [2]. Currently, aviation accounts for 2-3% of annual anthropogenic carbon emissions. With demand for air transport projected to grow at 4% annually, and in the absence of carbon-neutral alternatives, aviation sector emissions are estimated to double by 2050 (see Figure 1.1). Taking into account the expected decarbonization of other sectors, climate model simulations project that the share of the aviation sector in global carbon emissions per year could increase to 10–46% in 2050 [3]. Furthermore, the climate footprint of aviation is significantly underestimated if only CO₂ emissions are considered, as radiative forcing effects caused by contrails and the emission of NO_x at high altitude substantially amplify its overall warming impact. Therefore, in addition to incentivizing social measures to promote the use of alternative modes of transportation (e.g., replacing flights with trains on short-to-medium routes) and implementing policy mechanisms to facilitate investments in low emission technologies (e.g., carbon pricing), the development of novel propulsion system concepts is key to making aviation carbon-neutral [4].

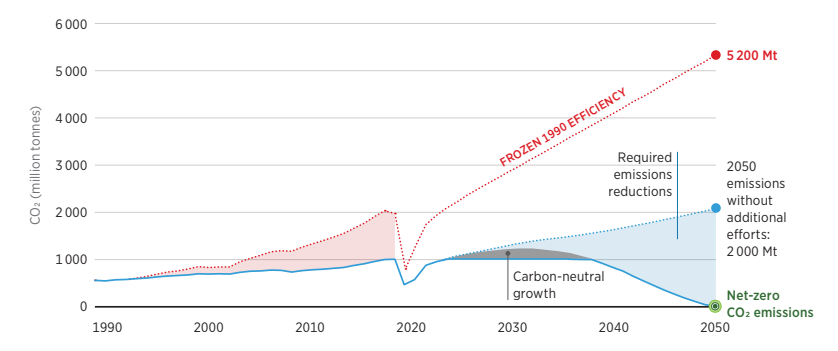


Figure 1.1: Time evolution of carbon emissions by the aviation sector, including a scenario for net-zero emissions, adapted from [1].

Propulsion systems for carbon-neutral aviation will be powered by renewable energy stored in batteries, green hydrogen, and sustainable aviation fuels (for example, e-SAF, produced from green hydrogen and carbon captured from air) [5]. Battery-powered aircraft, commonly referred to as battery-electric or hybrid electric aircraft, are better suited for short-range flights because of the current low energy density of batteries. In contrast, aircraft powered by green hydrogen and e-SAF are more suitable for longer-range flights. At the same time, the primary energy consumption associated with these technologies varies significantly: as a quantitative estimate, for every 1 MJ of energy carried onboard, approximately 1.17 MJ, 2.18 MJ, and 3.85 MJ of electricity produced with renewable energy sources is needed for electric, hydrogen-powered, and e-SAF-based aircraft, respectively [6].

To increase the viability of deploying carbon-neutral energy carriers, minimizing mission energy consumption will remain the primary driver in the design of aircraft systems and components. A common characteristic across the novel propulsion and power technologies currently investigated is the increased relevance of heat transfer equipment. Examples of novel propulsion concepts developed for conventional fuel or SAF include ultra-high bypass ratio geared turbofans (UHBR GTF) and the recuperated or combined cycle (CC) engines, such as the water-enhanced turbofan engine (WET) [7] and those that integrate a waste heat recovery unit. This last solution can be based either on the organic Rankine cycle (ORC) [8] or the supercritical carbon dioxide (sCO₂) Brayton cycle [9] concepts. While the primary requirement in CC engines is to achieve efficient thermal energy recovery through compact heat exchangers, one of the main challenges in the realization of UHBR engines is the effective cooling of the gearbox to ensure operational safety and component lifetime. The waste heat from an exemplary 75 MW gearbox for UHBR GTF is estimated to be 750 kW, requiring a dedicated cooling system [10].

Propulsion systems that require more adaptations at aircraft level are those based on hybrid electric powertrains. In hybrid electric aircraft (HEA), thermal management systems are essential to control the operational temperature of electric propulsion components, including electric motors, batteries, and avionics [11], see Figure 1.2. Effective dissipation of waste heat from these components is critical to preventing performance degradation and system failure. For example, batteries must ideally operate in the temperature range of 0–40°C [12], and excessive overheating can cause thermal runaway. For electric aircraft concepts such as SUSAN Electrofan [13] and ECO-150R [14], heat loads of up to 1.5 MW have been estimated. The mass of the thermal management system can be estimated as 1 kg per kW of rejected heat [15]. Furthermore, with the energy density of batteries projected to more than double by 2035, the thermal loads and associated heat flux values are expected to rise further [16].

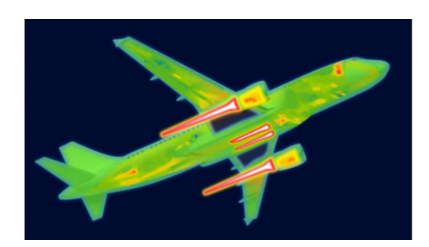




Figure 1.2: Illustration of high-exergy (left) and low-exergy (right) heat sources aboard an aircraft. Image taken from Ref. [11].

In hydrogen(H_2)-powered aircraft, the role of the thermal management system is even more central as both the propulsion and fuel systems [17] require temperature control. For H_2 -based propulsion using fuel cells, the thermal management requirements of electric motors and avionics are similar to those of HEA; however, significantly higher heat loads are expected for fuel cell stacks since half of the fuel chemical energy is converted into heat in these devices [18]. Furthermore, independently of the chosen propulsion technology, the storage of liquid H_2 at a cryogenic temperature of -253°, along with its subsequent

vaporization and preheating prior to delivery to the propulsion system, requires advanced thermal management strategies [19]. An example of such strategies is the integration of the fuel handling system with a heat recovery unit. This can be achieved by recovering thermal energy from the prime mover via, for instance, a H_2 direct expansion cycle [20].

Figure 1.3 depicts a process flow diagram of an exemplary thermal management system for a future hybrid-electric aircraft. It comprises various components such as heat exchangers, pumps, piping, valves, etc. The system configuration and its components must be designed to meet the thermal requirements while minimizing power consumption, system weight, and the drag associated with the use of ram air for rejecting thermal energy into the environment.

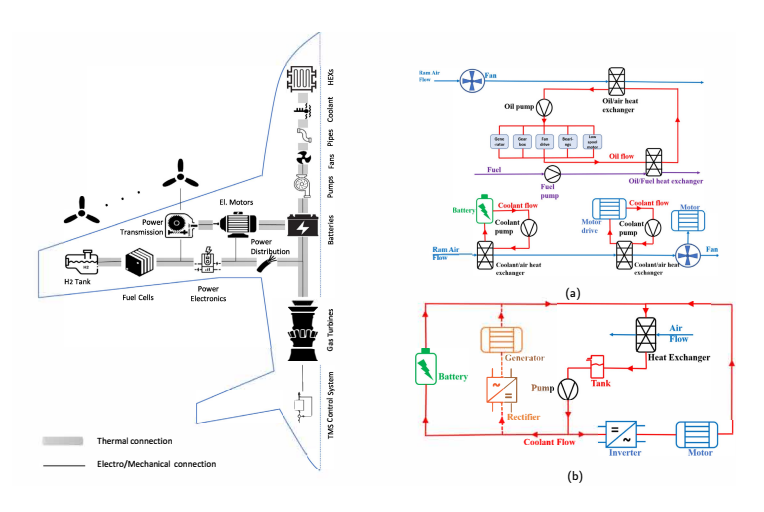


Figure 1.3: Thermal management system (TMS) of a hybrid-electric propulsion concept along with its components (left) and process flow diagrams of two exemplary TMS architectures, adapted from [17].

1.2. AEROSPACE-GRADE HEAT EXCHANGERS

Among the components of thermal management systems, the bulkiest and arguably the most critical components are the heat exchangers. The same consideration applies to airborne thermal energy recovery units. Regarding current aerospace applications, heat exchangers (HEXs) are an integral part of gas turbine engines, the environmental control system, and other thermal management loops [21], as summarized in Figure 1.4. HEXs can be classified on the basis of their process functions, such as evaporators, condensers, recuperators, etc. A simplified form of HEX is the so-called cold-plate, a thermal component with only one fluid, generally used for cooling of surfaces with high heat loads. In addition, HEXs can be classified on the basis of their topologies, compactness, arrangements, number of fluids, etc. Refer to Ref. [22] for a comprehensive classification.

Figure 1.5 illustrates the typical HEX topologies considered for aircraft applications: plate-fin HEX, microchannel HEX, and tubular HEX. Plate-fin HEXs, such as the one shown in Figure 1.5(a), are widely used in engine oil cooling systems due to their compactness and lightweight design. These HEXs feature extended surfaces, which may have



Figure 1.4: Examples of heat exchangers utilized in aerospace systems, adapted from Ref. [21]. The classification of HEXs adopted here is based on their process function.

various geometries – such as rectangular fin, wavy fin, offset strip fin, and louvered fin – to enhance heat transfer. In case of liquid-to-gas heat transfer and limited space availability, micro-channel HEXs are the preferred option due to their higher compactness. An example is shown in Figure 1.5(b). This type of HEX is also suitable for use as a condenser or evaporator in aircraft environmental control systems based on the vapor compression cycle technology. Tubular HEXs, such as the one depicted in Figure 1.5(c), are instead considered for the recuperators of combined cycle engines to minimize the pressure drop in the exhaust gases.

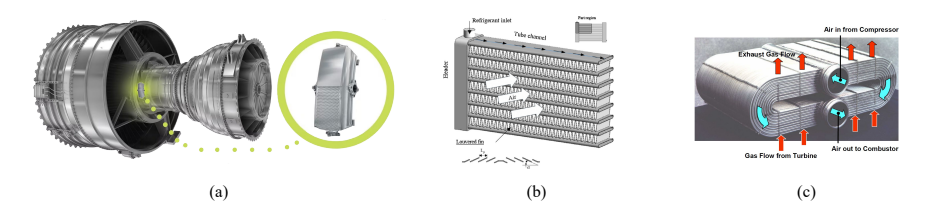


Figure 1.5: Heat exchangers for aeronautical applications manufactured using conventional methods. Images taken from Ref. [23–25].

A common characteristic of the HEXs presented in Figure 1.5 is that they are manufactured using conventional methods, such as extrusion, milling, sheet metal forming, brazing, etc. Recently, additive manufacturing (AM), popularly known as 3D printing, has been introduced in the production of aerospace HEXs, enabling designs with higher compactness and improved thermal performance. AM provides greater design freedom by facilitating the realization of complex geometries that are difficult or impossible to manufacture using conventional methods. This capability enables the manufacturing of conventional HEX topologies with miniaturized dimensions, and the fabrication of entirely new layouts and heat transfer surface geometries. Figure 1.6(a) depicts a microchannel HEX manufactured via AM consisting of bare tubes with unconventional shapes. This design achieves the same heat transfer rate of a conventional louvered fin microchannel HEX with flat tubes while offering approximately a 15% decrease in air-side pressure drop and a $\sim 25\%$ reduction in volume [26]. Figure 1.6(b) and (c) show innovative internal channel geometries and heat exchanger topologies, as documented in Ref. [27], which allow for a better integration of the HEX within the overall system. Thus,

advanced additive manufacturing techniques can bring substantial improvements in the performance of aerospace heat exchangers.

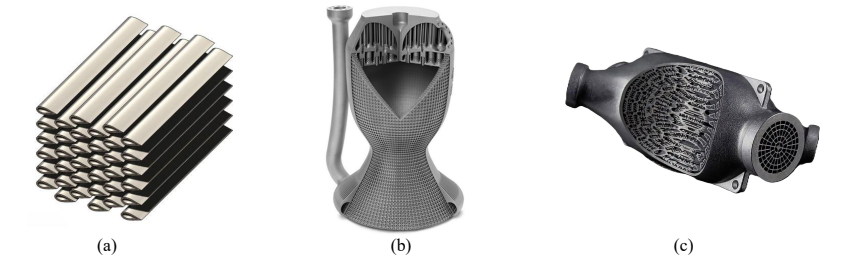


Figure 1.6: Heat transfer devices realized by additive manufacturing-based methods. Images taken from Ref. [26, 27].

Characterization of HEX performance: High-performance aerospace heat exchangers should feature high effectiveness, compact size, low weight, and minimal pressure losses. The effectiveness of a heat exchanger (ϵ) is defined as the ratio between the heat transfer rate and the maximum heat transfer rate, based on the theoretical maximum temperature difference between the two fluid streams of the heat exchanger. Surface compactness - defined as the heat transfer area per unit volume - is a key factor in achieving a high thermal power density (defined as the heat transfer rate per volume) and consequently a high effectiveness within a compact volume. The actual heat transfer rate from a surface depends not only on the temperature difference with respect to the bulk flow, but also on the heat transfer coefficient h. For a given level of surface compactness, higher heat transfer coefficients enable reductions in both weight and volume or an enhancement of effectiveness. The reduction in weight is particularly important for aerospace applications because of its direct impact on the mission energy consumption. This imposes stringent requirements for heat rejection per unit weight, which are currently in the range of 1-5 kW/kg and are projected to reach 5-20 kW/kg by 2050 [28]. For a given heat duty, material properties, and surface compactness, this translates into the requirement of a higher heat transfer coefficient. Therefore, the thermal performance of a compact HEX is primarily characterized by the heat transfer coefficient and the associated non-dimensional numbers, namely the Nusselt number Nu and the Colburn factor j. Similarly, hydraulic performance in terms of pressure losses can be characterized by the friction factor f. However, the maximization of the overall heat transfer coefficient and the minimization of the friction factor are objectives that are in trade-off, as an increase of h is generally accompanied by an increase of f. Therefore, to enhance the performance of aerospace HEXs, especially considering the design freedom offered by modern manufacturing methods, advanced computational methods capable of dealing with industrial-strength design problems need to be developed.

1.3. Models and methods for HEX design and analysis

The design and analysis of HEXs are performed using analytical, empirical, and numerical models and methods. A model is a simplified representation of the physical processes occurring in the HEX using mathematical equations, whereas a method is a sequence of

steps or procedures followed to achieve the goal of HEX performance rating or design. In performance rating problems, a HEX model is employed to estimate the performance of the device given a fixed geometry and specific operating conditions. In sizing or design problems, the design method integrates an HEX model to determine the geometry required to achieve the desired performance.

Models for HEXs can be broadly classified into lumped-parameter models, which rely on analytical equations and empirical correlations to predict heat transfer coefficients and friction factors, and higher-fidelity models, such as those based on computational fluid dynamics (CFD), which involve the solution of the partial differential equations describing the flow and heat transfer phenomena in an HEX.

Lumped-parameter models are generally derived based on the assumption of uniform fluid thermo-physical properties throughout the HEX or a portion of it. In these models, the heat transfer rate depends on the overall heat transfer coefficient (U), heat transfer area (A), flow arrangement, and the HEX operating conditions. The overall heat transfer coefficient is calculated based on the convective heat transfer coefficients (h) on the sides of the hot and cold fluid, also possibly accounting for the presence of fouling and the thermal resistance of the wall. However, the assumption of constant thermo-physical properties or thermal resistances within the overall HEX results in large inaccuracies in applications where one or both fluids undergo a phase change or a large temperature variation. The change in thermo-physical properties along the streamwise direction can be captured by relying on more advanced formulations of lumped-parameter models, such as those based on thermal circuit representations [29], ordinary differential equations [30], or discretization of the HEX geometry in multiple control volumes [31]. However, all of these models still depend on simplified analytical approximations and empirical correlations for estimating the heat transfer coefficients and friction factors, which thus limit the model applicability to relatively simple geometries and to operating conditions that fall within the validity range of the same experimental correlations.

In contrast, CFD-based models enable the evaluation of HEX performance across a wide range of geometries and flow conditions while capturing local variations in flow characteristics and thermo-physical properties. However, the full-scale CFD simulation of an entire HEX remains computationally prohibitive even with access to modern supercomputers, due to the vast range of length scales and turbulence structures, as well as the multiphysical nature of the phenomena involved. Consequently, CFD-based models of HEXs often employ various geometric simplifications and reduced-order modeling strategies, as illustrated in Figure 1.7 for single-phase flow applications.

CFD models often exploit symmetry or periodicity in the geometry to reduce the computational domain. Models based on periodicity can be categorized into spanwise and streamwise periodic unit models. When spanwise periodicity is modeled, the computational domain is reduced by assuming identical flow patterns across parallel channels, allowing the simulation of a representative portion of the HEX. With streamwise periodicity modeling, the computational domain is reduced to only a unit cell – i.e., a repeating geometrical element of the HEX – under the assumption that periodic flow and heat transfer are established sufficiently downstream from the inlet. This modeling approach requires appropriate modifications to the governing equations [32]. Moreover, the solution obtained from these periodic unit models can be used to estimate, to a

8

first approximation, the macro-scale performance of the HEX [33]. Alternatively, some CFD models treat the HEX core as a porous medium, with the heat transfer coefficient and pressure drop computed by source terms based on semi-empirical correlations or calibrated with ad hoc CFD simulations [34].

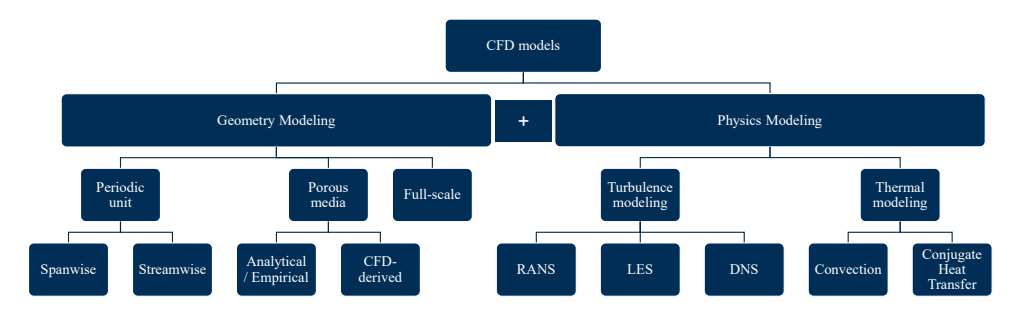


Figure 1.7: Overview of CFD models for heat exchangers with single-phase fluids.

Alongside geometric simplification, appropriate turbulence and thermal models are selected based on the available computational resources and the required fidelity. Turbulent flows are most commonly modeled using Reynolds-Averaged Navier-Stokes (RANS) equations, though Large Eddy Simulation (LES) is increasingly used [35], while Direct Numerical Simulation (DNS) remains limited to simplified or small-scale problems [36]. In addition, there are numerous hybrid models, which combine elements of different modeling strategies, such as hybrid RANS-LES models [37]. The modeling of the heat transfer process is generally simplified by assuming constant temperature or constant heat flux at the flow domain boundaries. This simplification allows for the analysis of convective heat transfer on only one side of a HEX. Constant temperature boundaries are typically used for components such as condensers and evaporators, while constant heat flux conditions are typically more appropriate for balanced HEXs or heat sinks. However, conjugate heat transfer modeling becomes necessary when the wall temperature profile or heat flux is strongly influenced by the thermal gradients established in the solid structure of the HEX. Another approach to reduce computational resources while retaining accuracy is to develop surrogate models, such as those based on Kriging or artificial neural networks, trained on data generated from detailed CFD simulations.

The models mentioned above are integrated into various methodologies for HEX design, which can be broadly classified as sizing, parametric study, and optimization methods. Sizing methods, such as the effectiveness–NTU (ϵ -NTU) and Log Mean Temperature Difference (LMTD) methods [38], involve estimating the required heat transfer area given the main geometric characteristics of the flow passages. Parametric study and optimization-based methods are used to obtain HEX designs with improved thermohydraulic performance. In a parametric study, geometric parameters are varied systematically within a pre-defined design space to identify configurations maximizing performance. In contrast, optimization-based methods use numerical algorithms to efficiently find an optimal design solution. These algorithms can be classified as gradient-free (zeroth-order) or gradient-based. In general, methods based on CFD models and optimization algorithms, and embedded into automated design chains, have the potential

to yield novel and unconventional heat exchanger designs with superior performance.

1.4. RESEARCH MOTIVATION AND OBJECTIVES

The optimization of the shape of HEXs is a complex task involving the modeling of the heat transfer surfaces by means of a large number of design variables. Shape optimization methods [39], based on CFD and surrogate models coupled with gradient-free algorithms, such as genetic algorithms, are not suitable for dealing with problems characterized by a number of design variables typically exceeding 30 [40, Ch. 1]. Adjoint-based design methods are not limited by such constraint and have recently been applied to heat transfer problems in which the mesh coordinates of the design surfaces themselves are treated as design variables [41, 42], or in which the surfaces are parameterized using free-form deformation (FFD) boxes, with their control points as design variables [43–45]. Despite their flexibility, adjoint methods based on FFD parametrization of the HEX geometry are not well suited to deal with geometric constraints and often require post-processing steps to convert the optimized shape back into a CAD-compatible format [46, 47]. This reconstruction step can result in suboptimal geometries from a manufacturing perspective. An alternative approach involves integrating a CAD-based representation of the design surface directly within the optimization loop, enabling the enforcement of complex geometric constraints [48]. This is particularly beneficial to comply with manufacturing requirements, including those associated with additive manufacturing (AM) [49]. Furthermore, CAD-based methods provide full control over the surface geometry, ensuring smoothness and design consistency [50]. While such a methodology is largely adopted in the automated design of turbomachinery [48, 51, 52], its application to HEX design remains almost unexplored.

The overarching goal of the research documented in this dissertation is the conception, development, and application of a shape optimization method based on the discrete adjoint and CAD-based parametrization for the optimal design of aerospace-grade HEXs. The method leverages the open-source software SU2 for CFD modeling based on RANS equations and for the solution of the associated discrete adjoint equations. The key objectives of the work can be summarized as follows.

- To develop a gradient-based optimization framework for heat transfer surfaces based on CAD parametrization and the discrete adjoint method implemented in the open-source CFD software SU2.
- To apply the framework to HEX design problems, including those involving conjugate heat transfer and 3D configurations relevant to thermal components of next-generation aircraft.
- To investigate the feasibility of integrating CFD-based HEX optimization in a systemlevel design procedure.

Original contributions from this work in the pursuit of the research objectives are, in summary:

 a CAD parametrization method based on Non-Uniform Rational Basis Splines (NURBS) originally developed for turbomachinery optimization was extended to

optimize heat transfer geometries that represent tubular heat exchangers and pin fins. Relevant geometric constraints and design bounds were imposed through CAD parametrization. Notably, the CAD-based approach was integrated with the SU2-based adjoint optimization framework to simultaneously optimize the shape and layout of multiple heat transfer geometries.

- The optimization framework can be applied to the design of both 2D and 3D heat transfer surfaces. The gradients obtained via the adjoint method were verified against those computed using a first-order finite-difference method. The capability of the design framework was demonstrated for representative applications, including aircraft condensers/evaporators and heat sinks for thermal management. Furthermore, this method was applied in combination with a system-level preliminary design model to demonstrate the potential improvements in system performance achievable by introducing advanced design techniques for HEXs already in an early phase of system design.
- Two approaches for shape sensitivity computation namely, consistent parametrization with averaged sensitivities (CP-AS) and consistent parametrization with local sensitivities (CP-LS) were proposed and applied to optimize multiple heat transfer surfaces (i.e., tubes) concurrently. The advantage of the CP-LS approach is that it enables the optimization of each surface independently, thus leading to solutions with non-identical geometries, while the CP-AS method facilitates optimization convergence with fewer design iterations and achieves identical geometries at the cost of a limited reduction in the performance improvement. A possible strategy to retain the advantages of both approaches consists of applying them sequentially: first performing an optimization using the CP-AS method to obtain an initial design, and then using this solution to initialize a subsequent optimization with the CP-LS approach.

1.5. OUTLINE

This dissertation is based on the material published in peer-reviewed journals and conference proceedings. Its content is organized into five chapters, which are summarized below.

Chapter 2 presents the methodology to perform adjoint-based shape optimization of multiple heat transfer surfaces using CAD-based parametrization. The framework is applied to optimize a 2D representation of a bare-tube HEX configuration. The thermal-hydraulic performance of the optimal solutions obtained using two sensitivity computation methods is compared.

Chapter 3 reports the application of the framework to a 3D design of pin fins in heat sinks with conjugate heat transfer. The optimized design features an unconventional fin shape that enables both an increase in the heat transfer coefficient and a reduction in total pressure losses. An in-depth analysis is then carried out to understand the flow phenomena that lead to this performance improvement.

Chapter 4 documents the integration of the shape optimization framework into a system-

level design method. The considered case study is the design of a combined cycle auxiliary power unit, whose condenser thermo-hydraulic performance is improved through the application of the shape optimization method developed in this work.

Chapter 5 summarizes the key outcomes of this research and provides recommendations for future work.

BIBLIOGRAPHY

- [1] International Renewable Energy Agency (IRENA), *Decarbonising Hard-to-Abate Sectors with Renewables: Perspectives for the G7*. Abu Dhabi: International Renewable Energy Agency, 2024.
- [2] C. Bergero, G. Gosnell, D. Gielen, S. Kang, M. Bazilian, and S. J. Davis, "Pathways to net-zero emissions from aviation", *Nature Sustainability*, vol. 6, no. 4, pp. 404–414, 2023. DOI: 10.1038/s41893-022-01046-9.
- [3] International Civil Aviation Organization, "Report on the feasibility of a long-term aspirational goal for international civil aviation CO2 emission reductions appendix R3: Results in the climate science context", International Civil Aviation Organization, Tech. Rep., Mar. 2022.
- [4] International Energy Agency, "Net zero by 2050: A roadmap for the global energy sector", International Energy Agency, Paris, Tech. Rep., 2021.
- [5] R. Sacchi *et al.*, "How to make climate-neutral aviation fly", *Nature Communications*, vol. 14, no. 1, 2023. DOI: 10.1038/s41467-023-39749-y.
- [6] E. J. Adler and J. R. Martins, "Energy demand comparison for carbon-neutral flight", *Progress in Aerospace Sciences*, vol. 152, p. 101051, 2025, ISSN: 0376-0421. DOI: 10.1016/j.paerosci.2024.101051.
- [7] S. Kaiser, O. Schmitz, P. Ziegler, and H. Klingels, "The Water-Enhanced Turbofan as Enabler for Climate-Neutral Aviation", *Applied Sciences*, vol. 12, no. 23, 2022, ISSN: 2076-3417. DOI: 10.3390/app122312431.
- [8] C. De Servi, L. Azzini, M. Pini, A. Gangoli Rao, and P. Colonna, "Exploratory assessment of a combined-cycle engine concept for aircraft propulsion", in *Proceedings of the 1st Global Power and Propulsion Forum*, Article GPPF-2017-78, Zurich, Switzerland, Jan. 2017.
- [9] L. Guo, L. Pang, X. Yang, J. Zhao, and D. Ma, "A power and thermal management system for long endurance hypersonic vehicle", *Chinese Journal of Aeronautics*, vol. 36, no. 2, pp. 29–40, 2023, ISSN: 1000-9361. DOI: 10.1016/j.cja.2022.07.01 2.
- [10] A. van Heerden, D. Judt, S. Jafari, C. Lawson, T. Nikolaidis, and D. Bosak, "Aircraft thermal management: Practices, technology, system architectures, future challenges, and opportunities", *Progress in Aerospace Sciences*, vol. 128, p. 100767, 2022, ISSN: 0376-0421. DOI: 10.1016/j.paerosci.2021.100767.

14 BIBLIOGRAPHY

1

- [11] T. J. Hendricks, C. Tarau, and R. W. Dyson, "Hybrid electric aircraft thermal management: Now, new visions and future concepts and formulation", in 2021 20th IEEE Intersociety Conference on Thermal and Thermomechanical Phenomena in Electronic Systems (iTherm), 2021, pp. 467–476. DOI: 10.1109/ITherm51669.202 1.9503205.
- [12] B. Tarhan, O. Yetik, and T. H. Karakoc, "Hybrid battery management system design for electric aircraft", *Energy*, vol. 234, p. 121 227, Nov. 2021, ISSN: 0360-5442. DOI: 10.1016/j.energy.2021.121227.
- [13] R. Jansen *et al.*, "Subsonic single aft engine (SUSAN) transport aircraft concept and trade space exploration", in *AIAA SCITECH 2022 Forum*, American Institute of Aeronautics and Astronautics, Jan. 2022. DOI: 10.2514/6.2022-2179.
- [14] B. T. Schiltgen and J. Freeman, "Aeropropulsive interaction and thermal system integration within the ECO-150: A turboelectric distributed propulsion airliner with conventional electric machines", in *16th AIAA Aviation Technology, Integration, and Operations Conference*, American Institute of Aeronautics and Astronautics, Jun. 2016. DOI: 10.2514/6.2016-4064.
- [15] R. de Vries, R. E. Wolleswinkel, M. Hoogreef, and R. Vos, "A new perspective on battery-electric aviation, part ii: Conceptual design of a 90-seater", in *AIAA Scitech 2024 Forum*, American Institute of Aeronautics and Astronautics, 2024, p. 1490. DOI: 10.2514/6.2024-1490.
- [16] B. J. Brelje and J. R. Martins, "Electric, hybrid, and turboelectric fixed-wing aircraft: A review of concepts, models, and design approaches", *Progress in Aerospace Sciences*, vol. 104, pp. 1–19, 2019, ISSN: 0376-0421. DOI: 10.1016/j.paerosci.2018.06.004.
- [17] M. Asli *et al.*, "Thermal management challenges in hybrid-electric propulsion aircraft", *Progress in Aerospace Sciences*, vol. 144, p. 100 967, 2024. DOI: 10.1016/j.paerosci.2023.100967.
- [18] E. J. Adler and J. R. Martins, "Hydrogen-powered aircraft: Fundamental concepts, key technologies, and environmental impacts", *Progress in Aerospace Sciences*, vol. 141, p. 100 922, 2023, Special Issue on Green Aviation, ISSN: 0376-0421. DOI: 10.1016/j.paerosci.2023.100922.
- [19] M. Coutinho *et al.*, "A review on the recent developments in thermal management systems for hybrid-electric aircraft", *Applied Thermal Engineering*, vol. 227, p. 120 427, 2023. DOI: 10.1016/j.applthermaleng.2023.120427.
- [20] P. Liu *et al.*, "Thermodynamic analysis of power generation thermal management system for heat and cold exergy utilization from liquid hydrogen-fueled turbojet engine", *Applied Energy*, vol. 365, p. 123 290, 2024, ISSN: 0306-2619. DOI: 10.1016/j.apenergy.2024.123290.
- [21] B. Sundén and J. Fu, "Chapter 6 aerospace heat exchangers", in *Heat Transfer in Aerospace Applications*, B. Sundén and J. Fu, Eds., Academic Press, 2017, pp. 89–115, ISBN: 978-0-12-809760-1. DOI: 10.1016/B978-0-12-809760-1.00006-5.

- [22] R. K. Shah and D. P. Sekulic, "Classification of heat exchangers", in *Fundamentals of Heat Exchanger Design*. John Wiley & Sons, Ltd, 2003, ch. 1, pp. 1–77, ISBN: 9780470172605. DOI: 10.1002/9780470172605.ch1.
- [23] F. Careri, R. H. Khan, C. Todd, and M. M. Attallah, "Additive manufacturing of heat exchangers in aerospace applications: A review", *Applied Thermal Engineering*, vol. 235, p. 121387, 2023, ISSN: 1359-4311. DOI: 10.1016/j.applthermaleng.2023.121387.
- [24] U. Han, H. Kang, H. Lim, J. Han, and H. Lee, "Development and design optimization of novel polymer heat exchanger using the multi-objective genetic algorithm", *International Journal of Heat and Mass Transfer*, vol. 144, p. 118 589, 2019, ISSN: 0017-9310. DOI: 10.1016/j.ijheatmasstransfer.2019.118589.
- [25] S. Boggia and K. Rüd, "Intercooled recuperated gas turbine engine concept", in *41st AIAA/ASME/SAE/ASEE Joint Propulsion Conference & Exhibit*, 2005. DOI: 10.2514/6.2005-4192.
- [26] D. Bacellar, V. Aute, Z. Huang, and R. Radermacher, "Design optimization and validation of high-performance heat exchangers using approximation assisted optimization and additive manufacturing.", *Science and Technology for the Built Environment*, vol. 23, no. 6, pp. 896–911, 2017. DOI: 10.1080/23744731.2017.13 33877.
- [27] B. Blakey-Milner et al., "Metal additive manufacturing in aerospace: A review", Materials & Design, vol. 209, p. 110 008, 2021, ISSN: 0264-1275. DOI: 10.1016/j.ma tdes.2021.110008.
- [28] A. Link, M. Staggat, and S. de Graaf, "Characterisation of thermal management specific heat rejection for electric propulsion architectures", in *Proceedings of the Aerospace Europe Conference EUCASS CEAS 2023*, 2023. DOI: 10.13009 /EUCASS2023-262.
- [29] S.-Y. Zhao and Q. Chen, "A thermal circuit method for analysis and optimization of heat exchangers with consideration of fluid property variation", *International Journal of Heat and Mass Transfer*, vol. 99, pp. 209–218, Aug. 2016, ISSN: 0017-9310. DOI: 10.1016/j.ijheatmasstransfer.2016.03.124.
- [30] Z. Guo, X. Liu, W. Tao, and R. Shah, "Effectiveness–thermal resistance method for heat exchanger design and analysis", *International Journal of Heat and Mass Transfer*, vol. 53, no. 13–14, pp. 2877–2884, Jun. 2010, ISSN: 0017-9310. DOI: 10.101 6/j.ijheatmasstransfer.2010.02.008.
- [31] F. Beltrame, D. Krempus, P. Colonna, and C. De Servi, "Reduced order modelling of optimized heat exchangers for maximum mass-specific performance of airborne ORC waste heat recovery units", in *Proceedings of the 7th International Seminar on ORC Power Systems*, International Seminar on ORC Power Systems, Seville, Spain, 2023.
- [32] S. Patankar, C. Liu, and E. M. Sparrow, "Fully developed flow and heat transfer in ducts having streamwise-periodic variations of cross-sectional area.", *Journal of Heat Transfer*, vol. 99, pp. 180–187, 1977. DOI: 10.1115/1.3450666.

BIBLIOGRAPHY

- [33] G. Buckinx, "Macro-scale flow and heat transfer in systems with periodic solid structures", Ph.D. dissertation, KU Leuven, Belgium, 2017.
- [34] K. Sbutega, D. Geb, and I. Catton, "Modeling of multiscale heat transfer systems using volume averaging theory", in *Advances in Heat Transfer*. Elsevier, 2015, pp. 1–165. DOI: 10.1016/bs.aiht.2015.08.001.
- [35] A. K. Saha and S. Acharya, "Unsteady simulation of turbulent flow and heat transfer in a channel with periodic array of cubic pin-fins", *Numerical Heat Transfer, Part A: Applications*, vol. 46, no. 8, pp. 731–763, Nov. 2004, ISSN: 1521-0634. DOI: 10.1080 /104077890504465.
- [36] S. Harikrishnan and S. Tiwari, "Unsteady flow and heat transfer characteristics of primary and secondary corrugated channels", *Journal of Heat Transfer*, vol. 142, no. 3, Jan. 2020, ISSN: 1528-8943. DOI: 10.1115/1.4045751.
- [37] S. Heinz, "A review of hybrid RANS-LES methods for turbulent flows: Concepts and applications", *Progress in Aerospace Sciences*, vol. 114, p. 100597, Apr. 2020, ISSN: 0376-0421. DOI: 10.1016/j.paerosci.2019.100597.
- [38] R. K. Shah and D. P. Sekulic, "Basic thermal design theory for recuperators", in *Fundamentals of Heat Exchanger Design*. John Wiley & Sons, Ltd, 2003, ch. 3, pp. 97–231, ISBN: 9780470172605. DOI: 10.1002/9780470172605.ch3.
- [39] J. Tancabel, V. C. Aute, and R. Radermacher, "Review of shape and topology optimization for design of air-to-refrigerant heat exchangers", in *Proceedings of the International Refrigeration and Air Conditioning Conference*, Paper 1965, 2018.
- [40] J. R. R. A. Martins and A. Ning, Engineering Design Optimization. Cambridge, UK: Cambridge University Press, Jan. 2022, ISBN: 9781108833417. DOI: 10.1017/97811 08980647.
- [41] R. Zhang and X. Qian, "Parameter-free Shape Optimization of Heat Sinks", in *Proceedings of Intersociety Conference on Thermal and Thermomechanical Phenomena in Electronic Systems, ITherm*, Jul. 2020, pp. 756–765, ISBN: 9781728197647. DOI: 10.1109/ITherm45881.2020.9190501.
- [42] K. Wang, X. Y. Zhang, Z. D. Zhang, and C. H. Min, "Three-dimensional shape optimization of fins in a printed circuit recuperator using S-CO2 as the heat-transfer fluid", *International Journal of Heat and Mass Transfer*, vol. 192, p. 122910, Aug. 2022, ISSN: 00179310. DOI: 10.1016/j.ijheatmasstransfer.2022.122910.
- [43] K. T. Gkaragkounis, E. M. Papoutsis-Kiachagias, and K. C. Giannakoglou, "Adjoint-assisted Pareto front tracing in aerodynamic and conjugate heat transfer shape optimization", *Computers & Fluids*, vol. 214, p. 104753, 2021, ISSN: 0045-7930. DOI: 10.1016/j.compfluid.2020.104753.
- [44] J. L. Anibal, C. A. Mader, and J. R. Martins, "Aerodynamic shape optimization of an electric aircraft motor surface heat exchanger with conjugate heat transfer constraint", *International Journal of Heat and Mass Transfer*, vol. 189, p. 122689, 2022, ISSN: 0017-9310. DOI: 10.1016/j.ijheatmasstransfer.2022.122689.

- [45] J. L. Anibal and J. R. Martins, "Adjoint-based shape optimization of a plate-fin heat exchanger using CFD", *Applied Thermal Engineering*, vol. 252, p. 123570, 2024, ISSN: 1359-4311. DOI: 10.1016/j.applthermaleng.2024.123570.
- [46] S. Vitale, M. Pini, and P. Colonna, "Multistage turbomachinery design using the discrete adjoint method within the open-source software SU2", *Journal of Propulsion and Power*, vol. 36, no. 3, pp. 465–478, 2020, ISSN: 1533-3876. DOI: 10.2514/1.B37 685.
- [47] L. Mueller and T. Verstraete, "CAD integrated multipoint adjoint-based optimization of a turbocharger radial turbine", *International Journal of Turbomachinery, Propulsion and Power*, vol. 2, no. 3, 2017, ISSN: 2504186X. DOI: 10.3390/ijtpp203 0014.
- [48] S. Xu, D. Radford, M. Meyer, and J.-D. Müller, "CAD-Based Adjoint Shape Optimisation of a One-Stage Turbine With Geometric Constraints", in *Proceedings of Turbo Expo: Power for Land, Sea, and Air*, vol. Volume 2C: Turbomachinery, Jun. 2015, V02CT45A006. DOI: 10.1115/GT2015-42237.
- [49] M. K. Thompson *et al.*, "Design for additive manufacturing: Trends, opportunities, considerations, and constraints", *CIRP Annals*, vol. 65, no. 2, pp. 737–760, 2016, ISSN: 0007-8506. DOI: 10.1016/j.cirp.2016.05.004.
- [50] N. Anand, S. Vitale, M. Pini, and P. Colonna, "Assessment of FFD and CAD-based shape parametrization methods for adjoint-based turbomachinery shape optimization.", in *Proceedings of Global Power and Propulsion Society, Montreal, Canada*, 2018, pp. 1–8. DOI: 10.5281/zenodo.1344595.
- [51] R. Agromayor, N. Anand, M. Pini, and L. O. Nord, "Multirow Adjoint-Based Optimization of NICFD Turbomachinery Using a Computer-Aided Design-Based Parametrization", *Journal of Engineering for Gas Turbines and Power*, vol. 144, no. 4, 2022, ISSN: 15288919. DOI: 10.1115/1.4052881.
- [52] A. Châtel and T. Verstraete, "Multidisciplinary optimization of the SRV2-O radial compressor using an adjoint-based approach", *Structural and Multidisciplinary Optimization*, vol. 66, no. 5, pp. 1–13, 2023, ISSN: 16151488. DOI: 10.1007/s00158-023-03556-2.

CONCURRENT OPTIMIZATION OF MULTIPLE HEAT TRANSFER SURFACES

Parts of this chapter have been published in:

P. Pai Raikar, N. Anand, M. Pini, and C. De Servi, *Concurrent optimization of multiple heat transfer surfaces using adjoint-based optimization with a CAD-based parametrization*, International Journal of Heat and Mass Transfer 236 (2025) 126230. DOI:10.1016/j.ijheatmasstransfer.2024.126230.

Abstract

Heat exchangers are key components of thermal energy conversion systems, however, their optimal design is still based on reduced order models relying on semi-empirical heat transfer correlations. CFD-based design optimization emerged as a viable method to provide a significant improvement in performance at an affordable cost. This chapter presents a framework to optimize multiple heat transfer surfaces concurrently using the adjoint method. The heat transfer surfaces are parametrized using a CAD-based parametrization method, and their performance is evaluated using a RANS solver complemented by its discrete adjoint counterpart for gradient computation. The optimization framework is applied to minimize the pressure drop across a bare-tube heat exchanger while constraining the heat transfer rate. Two variants of the same optimization problem are formulated: in the first one, the sensitivities are averaged and the tubes are constrained to maintain the same shape, while in the second variant, the shape of the tubes can vary, resulting in an optimum solution with non-identical tube shapes. The results show that the optimized geometry reduces the pressure drop by 19% if the tube shapes are identical, and by 25% in the case of non-identical shapes, compared to the baseline. To identify the physical mechanisms contributing to the fluid-dynamic losses, entropy generation along the flow path was investigated. The results reveal that the major loss reduction observed for the case of non-identical tube shapes is due to the better thermo-hydraulic performance of the first and last tubes.

2.1. Introduction

Heat exchangers (HEXs) are ubiquitous in thermal energy conversion systems, and they find application in transportation, industrial processes, and residential systems. In aviation, heat exchangers will be the key enabling components of future propulsion and power systems. Examples are condensers of engines enabling carbon-neutral aviation [1], evaporators or condensers in waste-heat recovery systems based on the organic Rankine cycle (ORC) [2], and radiators used to reject low-temperature thermal energy in fuel-cells-based propulsion systems or electric motors/generators [3]. Given that HEXs are arguably the bulkiest components in all these novel technologies, maximizing the thermal-hydraulic performance and reducing their weight and volume is, therefore, decisive to meet the requirement of compactness needed in airborne applications [3].

The standard design practice of heat exchangers is based on reduced-order models (e.g., models based on lumped-parameter or one-dimensional methods), making use of correlations based on dimensionless numbers (e.g., the Nusselt number or Colburn factor) for the computation of the heat transfer coefficient and pressure drop [4]. In recent years, parametric studies based on Computational Fluid Dynamics (CFD) have been used to analyze several designs for identifying the optimal HEX geometry [5–12]. These studies investigated the influence of geometric parameters such as tube radius and layout, or fin pitch, thickness, louvered angle, height, and spacing on the performance of the heat exchangers.

Recently, various studies performing shape optimization on heat transfer surfaces have demonstrated the potential of CFD-based automated design methods in improving HEX performance. For example, Ranut et al. [13] optimized the shape of tubular heat exchangers using a multi-objective genetic algorithm (MOGA). The computational

cost of the CFD simulation used to evaluate HEX performance was reduced using the streamwise periodic flow approach documented in Ref. [14]. Furthermore, CFD-based meta-models were used to reduce the overall cost of the optimization. Likewise, Bacellar et al. [15] employed Kriging as a surrogate model for reducing the computational expense of CFD-based shape optimization. In the same study, it was established that optimized bare-tube heat exchangers performed better than conventional louvered-fin mini/micro-channel heat exchangers. This paved the way for further studies on the design of bare-tube HEX [16–18] using the same methodology described in Ref. [15]. Besides optimizing bare-tube HEXs, MOGA has been used to design shell-and-tube HEXs, microfins, and heat sinks, utilizing metamodels based on the Kriging method [19–24] and, more recently, neural networks [25, 26]. However, surrogate-based methods are suited to handle problems with a limited number of design variables. Therefore, optimizing multiple heat transfer surfaces is unsuitable because of the challenges associated with a larger number of design variables and the computational cost of generating the surrogate models.

For optimization problems characterized by a large number of design variables, gradient-based methods relying on the computation of the sensitivities with the discrete adjoint method are more appropriate [27, Ch. 1]. A gradient-based method requires fewer iterations to achieve optimization convergence than a gradient-free method. Furthermore, the discrete adjoint method enables the calculation of gradients of objective functions that require the solution of RANS equations at a cost similar to that of the flow solver, irrespective of the number of design variables. Shape optimization based on the adjoint method has been recently applied to the automated design of heat transfer elements, in combination with different geometry parametrization techniques. Zhang and Qian [28] performed a parametrization-free shape optimization of multiple fins, in which the design variables were the mesh nodes of the design surfaces. The optimized fins provided a 75% increase in the outlet temperature for the same pressure drop of the baseline design. Wang et al. [29] utilized the adjoint method for parametrization-free 3D shape optimization of fins in recuperators of Brayton power cycles using supercritical carbon dioxide. The computational domain was simplified to include only a single fin per cold and hot sides, and the design variables were the nodes of the fin surface mesh. A method used to parametrize the HEX geometry is through the so-called free-form deformation (FFD) boxes. Anibal et al. [30] employed FFD for optimizing novel heat sinks for the thermal management of electric motors in aerospace applications. In more recent work, Anibal and Martins [31] applied the same optimization framework to optimize plate-fin heat exchangers for aerospace applications with the objective of minimizing drag and weight. FFD boxes based on volumetric B-splines offer better control on the geometry than conventional FFD and parameter-free approaches. Gkaragkounis et al. [32] performed a multi-objective shape optimization of 3D fins to obtain a Pareto front with respect to two objective functions: the minimization of pressure losses and the maximization of the heat transfer rate. Albeit FFD boxes can be used to parameterize arbitrarily complex shapes, they are less straightforward to employ for imposing the geometric constraints that are needed to guarantee that the optimal geometry can eventually be manufactured [33, 34]. Conversely, a CAD-based parametrization of the design surface, defined by NURBS control points, provides a much better definition of the design surface and a complete control over it [35, 36]. Constrained optimization with CAD-based parametrization has been successfully applied for the optimal design of turbomachinery blades. For example, Xu et al. [36] applied CAD-based parametrization to the optimization of a one-stage turbine with geometric constraints on blade thickness and trailing edge radius. Agromayor et al. [37] developed a CAD-based blade parametrization method suitable for axial and radial turbomachines that was used to perform adjoint-based shape optimization with the open-source software SU2 [38, 39]. Châtel and Verstraete [40] utilized a CAD-based parametrization along with the discrete adjoint method to perform constrained aero-structural optimization of a radial compressor.

Application of adjoint-based shape optimization with the CAD representation of the design surface embedded in the automated design chain has been mostly confined to the design of single geometries, and studies dealing with the concurrent design of multiple surfaces remain limited: Gkaragkounis et al. [41] optimized a 2D representation of the internal cooling channels of a gas turbine blade, though only the blade profile and the location of the cooling channels were varied. This study aims to establish a methodology to perform adjoint-based shape optimization of multiple heat transfer surfaces using CAD-based parametrization. An automated design chain developed for this purpose encompasses the open-source CFD suite SU2 [38] – to perform CFD simulations, adjoint evaluations, and mesh deformation – and a python-based CAD parametrization tool [37, 42] – to parametrize the heat transfer surfaces using NURBS. The design chain is applied to the optimization of an array of two-dimensional tubes, representing a simplified configuration of a bare-tube heat exchanger, as described in Ref. [15]. Two optimization problems are formulated: one in which the sensitivities are averaged to impose the same shape deformation to the various tubes, and the other in which the tubes are concurrently optimized, albeit independently. The optimized designs are compared to the baseline case in terms of flow and heat transfer characteristics. Entropy generation along the flow path is finally investigated to identify the physical mechanisms contributing to loss.

2.2. METHODOLOGY

The optimization framework encompasses the open-source CFD software SU2 [38] embedding a discrete adjoint method for gradient calculation, a solver for mesh deformation, a CAD-based parametrization tool [37, 42], and a gradient-based optimizer.

The overall optimization framework is illustrated by means of the XDSM diagram [43] shown in Figure 2.1. The heat transfer design surfaces, such as heat exchanger tubes or fins, are parametrized through curves controlled by a set of design variables (α). At each design iteration, the surface coordinates (\mathbf{X}_{surf}) defined by the parametric curves, are generated. The corresponding volume mesh (\mathbf{X}_{vol}) is obtained by deforming the initial mesh. The value of the objective function (J) and the flow-related constraints (c_{f}), like the heat transfer rate \dot{Q} , are then computed with SU2. Next, the gradients of the cost functions with respect to the mesh coordinates $\left(\frac{\mathrm{d}J}{\mathrm{d}\mathbf{X}_{\text{vol}}}, \frac{\mathrm{d}c_{\text{f}}}{\mathrm{d}\mathbf{X}_{\text{vol}}}\right)$, are computed using the adjoint solver. Finally, the gradient values of the cost functions with respect to the design variables (α) are obtained by applying the chain rule of differentiation. The sensitivity of the objective function with respect to the design variables can be therefore written as

$$\frac{\mathrm{d}J}{\mathrm{d}\boldsymbol{\alpha}} = \frac{\mathrm{d}J}{\mathrm{d}\mathbf{X}_{\mathrm{vol}}} \cdot \frac{\mathrm{d}\mathbf{X}_{\mathrm{vol}}}{\mathrm{d}\mathbf{X}_{\mathrm{surf}}} \cdot \frac{\mathrm{d}\mathbf{X}_{\mathrm{surf}}}{\mathrm{d}\boldsymbol{\alpha}},\tag{2.1}$$

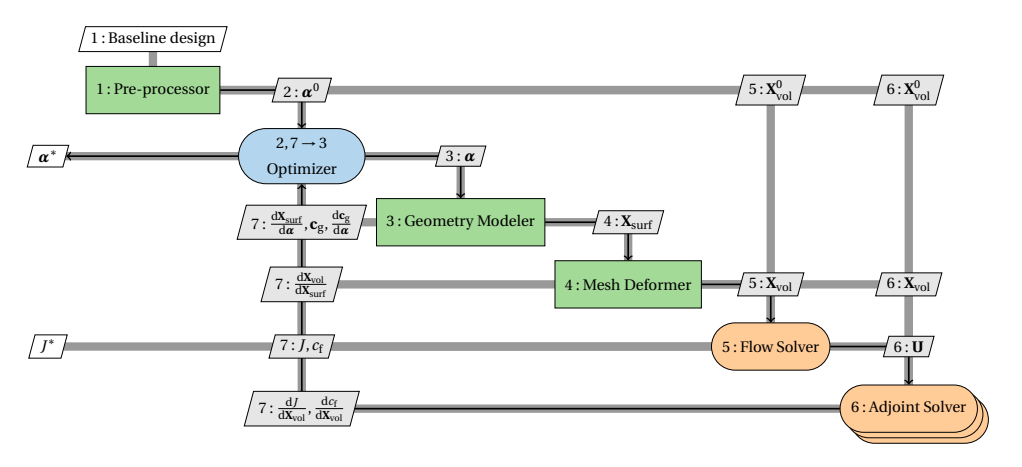


Figure 2.1: XDSM diagram depicting the inter-dependencies among the blocks of the optimization framework.

where $\frac{dX_{vol}}{dX_{surf}}$ is the sensitivity of the mesh coordinates with respect to the mesh nodes of design surfaces and $\frac{dX_{surf}}{d\alpha}$ represents the sensitivity of the mesh nodes of the design surfaces with respect to the design variables.

The methods underlying the various blocks of the optimization framework illustrated in Figure 2.1 are presented in the following.

2.2.1. OPTIMIZER

The gradient-based optimization method Sparse Nonlinear OPTimizer (SNOPT) [44], interfaced by means of the open-source python package pyOptSparse [45], is adopted. SNOPT is suited for constrained shape optimization problems involving multiple design surfaces because of its advantages in handling large-scale problems with sparse matrices.

2.2.2. GEOMETRY MODELER

The heat transfer design surfaces are constructed using the CAD-based parametrization method from Ref. [37]. This method facilitates the parametrization of a broad range of geometries of HEX tubes and fins, ranging from conventional shapes, such as circular and elliptical, to more unconventional designs, such as tear-drop and airfoil-type geometries, also in the case of 3D features. For 2D geometries, each design surface is represented by three NURBS curves: the camber line, the upper side, and the lower side, as shown in Figure 2.2. The upper and the lower sides are generated by imposing thickness distributions on the camber line, see Figure 2.2. Considering uniform weights for the NURBS control points, the camber line is defined as a cubic B-spline curve, while the upper and lower sides are B-spline curves of fourth order. These curves are defined by the design variables tabulated in Table 2.1, and the equations describing them are documented in Ref. [37]. In the case of 3D geometries, the camber surface is defined using a bi-quartic B-spline. Similarly, the upper and lower sides of the 3D geometry are defined using B-spline surfaces of fourth order.

The sensitivities of the design surfaces with respect to the design variables, namely the

CAD sensitivities $\left(\frac{dX_{surf}}{d\alpha}\right)$, are computed using the complex-step method [46] that guarantees second-order accuracy. Thanks to the CAD parametrization, arbitrary geometric constraints (\mathbf{c}_g) can be defined based on the NURBS curves, and their sensitivities $\left(\frac{d\mathbf{c}_g}{d\alpha}\right)$ can be obtained using the complex-step method.

Table 2.1: Design variables for the 2D camber-thickness parametrization.

Variable name	Symbol(s)
Leading edge abscissa and ordinate	$x_{\rm in}, y_{\rm in}$
Axial chord length	c_{ax}
Stagger angle	ξ
Inlet and exit metal angles	$\theta_{ m in}$, $\theta_{ m out}$
Inlet and exit tangent proportions	$d_{\rm in}$, $d_{ m out}$
Inlet and exit radii of curvature	$r_{\rm in}, r_{\rm out}$
Upper and lower thickness distributions	t ^u , t ^l

2.2.3. MESH DEFORMER

Mesh deformation is performed using the linear elasticity equations [47] in which the surface deformation is imposed as a Dirichlet boundary condition. This method, available within SU2, has been proven efficient and robust to handle the deformation of complex meshes. However, for large deformations, the mesh quality may be compromised.

2.2.4. FLOW SOLVER

Incompressible RANS simulations are performed using SU2 [38, 48] to assess the thermal-hydraulic performance of HEXs. The discretized form of the RANS equations is obtained using a finite volume method and density-based approach adopting the artificial compressibility method documented in Ref. [48]. The convective fluxes are reconstructed with the Flux-Difference-Splitting (FDS) method with low-speed preconditioning [49] and the MUSCL [50] approach to achieve second-order accuracy. The spatial gradients are computed using the Green-Gauss [51] method. The turbulence effects are modeled with the Spalart-Allmaras [52] model, and full resolution of the boundary layer is achieved by prescribing $y^+ < 1$ at the heat transfer surfaces. The steady-state solution is achieved using a time-marching scheme with Euler implicit time integration. Overall, the linearized governing equations are solved using the flexible generalized minimum residual (FGMRES) method [53] with an ILU preconditioner.

2.2.5. ADJOINT SOLVER

The sensitivities of the cost functions with respect to the mesh coordinates $\left(\frac{dJ}{dX_{vol}}, \frac{dc_f}{dX_{vol}}\right)$ are computed using the discrete adjoint method, and the numerical derivatives are obtained by means of the reverse mode of the open-source algorithmic differentiation tool CoDiPack [54], available within SU2. The formulation of the adjoint equations and their implementation in SU2 are documented in Ref. [55]. The discretization schemes used for the adjoint equations are the same as those used for the flow equations. The

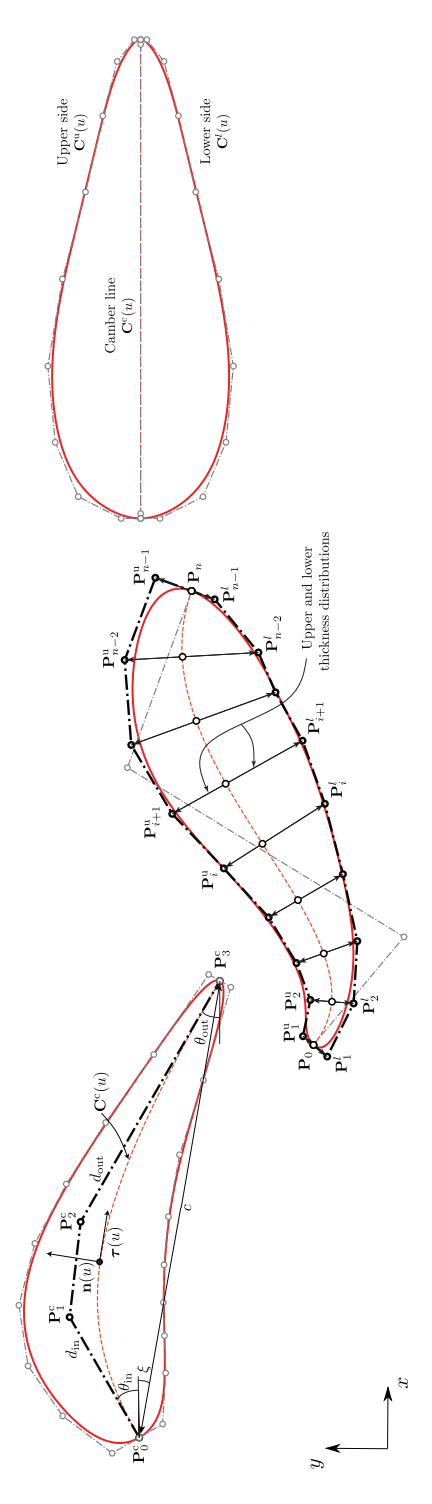


Figure 2.2: Construction of multiple 2D geometries using the camber-thickness approach. The three design surfaces (in red) demonstrate the application of the main three steps of the parametrization procedure, though to different HEX fins/tube shapes. In the first geometry (left), the parameters defining the camber line are highlighted. The middle geometry demonstrates how the thickness distributions are applied around the camber line, while in the final geometry (right), the NURBS curves representing the complete design surface are annotated.

adjoint solver has a computational cost similar to the primal solver in terms of runtime, albeit with higher memory requirements.

2.2.6. SENSITIVITY COMPUTATION FOR OPTIMIZATION OF MULTIPLE HEAT TRANSFER SURFACES

Multiple design surfaces are represented by a consistent parametrization method (CP), i.e., a method exploiting the same set of CAD parameters for each surface. This choice implies that the CAD parameters of a HEX configuration with identical pins or tubes are the same for all surfaces, apart from the leading edge coordinates. When concurrently optimizing multiple surfaces, the design sensitivities of the various surfaces typically differ due to the varying local flow conditions. Therefore, it can be hypothesized that performing shape optimization in which each heat transfer surface is separately optimized can provide significantly improved HEX performance. In order to verify such a hypothesis, two formulations of the same optimization problem are conceived, termed consistent parametrization with local sensitivities (CP-LS) and consistent parametrization with averaged sensitivities (CP-AS). In the CP-LS formulation, each geometry is optimized independently from the others, in accordance with the computed values of the gradient. Conversely, in the CP-AS, the sensitivities of the cost functions are averaged, yielding to

$$\frac{\mathrm{d}f}{\mathrm{d}\boldsymbol{\alpha}_i} = \frac{1}{N} \sum_{j=1}^N \frac{\mathrm{d}f}{\mathrm{d}\boldsymbol{\alpha}_i^j},\tag{2.2}$$

where f is the cost function, i indicates the design variable, N is the total number of design surfaces, and j denotes the design surface. Note that, with this method, identical shapes are obtained if the initial HEX configuration features the same geometry of pins or tubes.

Additionally, sensitivity averaging is performed to prevent asymmetric tube shapes during the optimization due to numerical inaccuracies and discretization errors. To this purpose, the sensitivities corresponding to the design variables of the upper and lower thickness distributions are averaged using the following equation

$$\frac{\mathrm{d}f}{\mathrm{d}\boldsymbol{\alpha}_{i}} = \frac{1}{2} \left(\frac{\mathrm{d}f}{\mathrm{d}\boldsymbol{\alpha}_{i}^{u}} + \frac{\mathrm{d}f}{\mathrm{d}\boldsymbol{\alpha}_{i}^{l}} \right) \tag{2.3}$$

where i is the index of the design variable in the thickness distribution array, and superscripts u, l indicate the upper and lower surface of the tube.

2.3. CASE STUDY

2.3.1. TUBULAR HEAT EXCHANGER GEOMETRY

The optimization framework is applied to a bare-tube air-to-fluid heat exchanger configuration. Bare tube heat exchangers, used as radiators, evaporators, and condensers, are promising in automotive and aerospace applications because of their lower weight and pressure drop compared to the conventional mini/micro-channel HEX [15, 16]. The focus in this case study is on improving the air-side performance of such HEX given that their design is largely driven by the heat transfer and pressure losses in the airflow. The

2.3. CASE STUDY 27

test case is inspired by the bare-tube radiator in Ref. [15] for which experimental data is available. The tubes are arranged in a staggered layout, resulting in a design that delivers a heat load comparable to that of conventional mini/micro-channel HEX while having a lower air-side pressure drop. The geometry arrangement consists of 7 ranks of tubes in the streamwise direction, as shown in Figure 2.3, while Table 2.2 presents the dimensions of the baseline geometry.

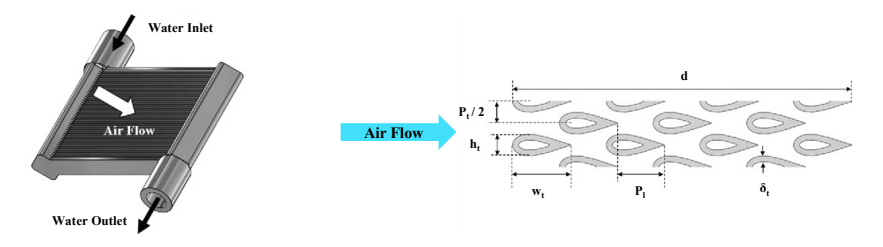


Figure 2.3: Illustration of tubular heat exchanger geometry from Ref. [15].

Table 2.2: Parameters defining	the tube bundle conf	iguration of the case study.

Design Variable	Description	Value [×10 ⁻³ m]
h_t	Height	1.1
w_t	Width	3.0
$\delta_{ m t}$	Thickness	0.3
P_l	Longitudinal tube pitch	2.4
P_t	Transverse tube pitch	2.2
d	HEX width	17.4

2.3.2. Numerical model

Since the case study focuses on improving the hydraulic performance of the air-side of the radiator and the temperature change of the working fluid inside the tubes is much lower than that of the airflow, isothermal wall boundary conditions are applied on the external surface of the tubes. Figure 2.4 depicts the computational domain with the boundary markers. The inflow $(1w_t)$ and outflow $(3w_t)$ boundaries of the domain were placed sufficiently far from the tubes to avoid any flow disturbance.

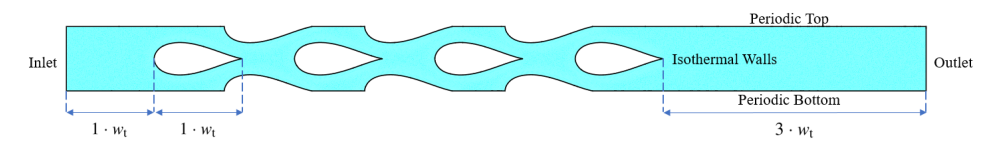


Figure 2.4: Computational domain (with boundary markers) corresponding to the baseline design of the selected test case.

The boundary conditions for this case study correspond to an air volume flow rate

of 0.03 m³/s. A velocity of 3 m/s and a temperature of 300 K were prescribed at the inlet. At the inlet, the turbulent to laminar viscosity ratio was 10. At the outlet boundary, a gauge pressure value of 0 Pa was set to imply atmospheric pressure, while the top and bottom boundaries were set as periodic boundaries. At the tube walls, a constant temperature of 350 K and no-slip boundary conditions were imposed. Overall, the test case is characterized by a Reynolds number of 530 by taking as characteristic length the major axis of the tube and as velocity the free-stream velocity. In all simulations, the fluid properties were assumed to be constant. Table 2.3 shows the values of the fluid properties at ambient pressure and a temperature of 313 K, which is approximately the average temperature value in the computational domain.

Table 2.3: Thermo-physical properties of air at 313K.

Density (ρ)	Specific Heat (C_p)	Viscosity (μ)	Thermal Conductivity (k)
[kg/m ³]	$[J/(kg \cdot K)]$	[Pa·s]	$[W/(m \cdot K)]$
1.1275	1006.9	1.9148×10^{-5}	0.0271

The flow around the tube bundle was solved by means of RANS equations using the numerical schemes described in subsection 2.2.4. A CFL number of 10 was selected for the optimization study to ensure the stability of the convergence process. The maximum number of iterations per cycle of the FGMRES linear solver was set to 10 with a convergence tolerance of 10^{-4} . The flow simulations were terminated once the residuals of the governing equations were reduced by 5 orders of magnitude.

2.3.3. GRID INDEPENDENCE STUDY AND MODEL VERIFICATION

The variation of the performance parameters - pressure drop and heat transfer rate - with mesh density was investigated. For this purpose, five unstructured hybrid meshes were generated using a commercial meshing tool [56]. The meshes comprise quadrilateral elements around the walls and triangular elements in the rest of the domain, see Figure 2.6. The mesh refinement strategy was such that the average element size was halved while the inflation layer thickness and progression were kept consistent across the different meshes. This was done to cluster the mesh cells to guarantee y⁺ values less than 1 close to walls. The air-side pressure drop in the heat exchanger was estimated from the pressure difference between the inlet and the outlet in the computational domain using Equation 2.4, while the heat transfer rate of the heat exchanger was calculated from the average temperature increase from the inlet to the outlet using Equation 2.5. The variation of the estimated pressure drop and heat transfer rate with the mesh density is shown in Figure 2.5, where a monotonic convergence of both quantities can be observed. For the purpose of the study, the mesh with about 94,000 elements was selected (shown in Figure 2.6) as the deviations of pressure drop and heat transfer rate compared to the finest mesh are approximately 0.8% and 0.2%, respectively.

$$\Delta P_{\text{air}} = P_{\text{in}} - P_{\text{out}}.\tag{2.4}$$

$$\dot{Q} = \dot{m}C_{\rm p}(T_{\rm out} - T_{\rm in}). \tag{2.5}$$

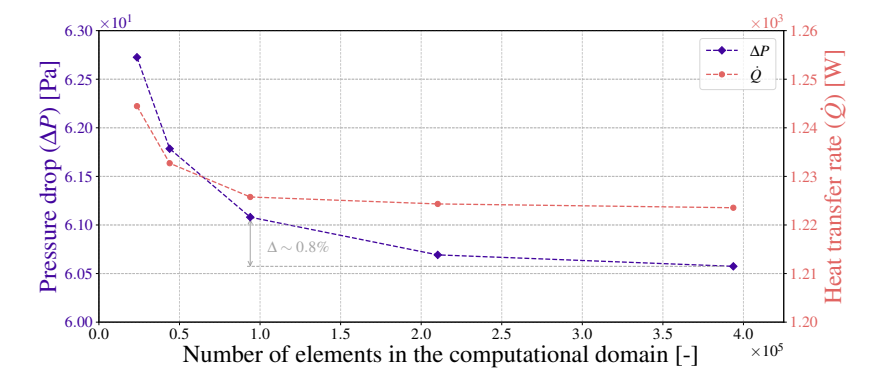


Figure 2.5: Variation of performance parameters with mesh density.

Furthermore, comparing the simulation output using the selected mesh to the experimental and numerical results published in Ref. [15], it was observed that the pressure drop was under-predicted by about 1.5% and 5%, respectively. Conversely, the heat transfer coefficient was over-predicted by roughly 7.5% and 2%. These discrepancies are relatively low, and they can be attributed to measurement uncertainty as well as the choice of the turbulence model, the assumption of constant air properties, and differences in the numerical setup. It can be concluded that the CFD model is reliable for the application at hand.



(a) Entire domain with labels for the tube design surfaces and lines at which the flow field is analyzed



(b) Enlarged view of the mesh

Figure 2.6: Discretized flow domain selected from the grid independence study.

2.3.4. OPTIMIZATION PROBLEM

The objective of the optimization is to minimize the pressure drop across the heat exchanger while maintaining a minimum required heat transfer rate. The mathematical

formulation of the optimization problem is as follows

$$\min_{\boldsymbol{\alpha}} \quad \Delta P_{\text{air}}(\boldsymbol{\alpha}), \tag{2.6}$$

subject to
$$\dot{Q} \ge \dot{Q}_0$$
, (2.7)

$$a \ge a_0, \tag{2.8}$$

where α represents the design variables, $\Delta P_{\rm air}$ is the air-side pressure drop, \dot{Q} is the heat transfer rate (computed using Eqn. (2.5)), \dot{Q}_0 is the heat transfer rate of the baseline design, a is the area enclosed within each tube and a_0 is the area enclosed within each tube of the baseline geometry. Such area constraint is specified to prevent the pressure drop of the fluid flowing within the tubes (not modeled) from deviating significantly from that of the baseline geometry. A tolerance of 1.5% and 0.5% is assigned to the values of the heat transfer and area constraint to improve the robustness of the optimization.

Two variants of the optimization problem are formulated, which differ in the method adopted for sensitivity computation as described in subsection 2.2.6. The first setup utilizes the CP-AS method, which results in tubes of identical shapes, while the second one adopts the CP-LS method, resulting in non-identical tube configurations.

DESIGN VARIABLES

The design variables are the CAD parameters defining the upper and lower thickness distributions around the camber line. As the tubes are symmetric with respect to the main axis, each design surface is described by eight independent parameters $t_i^{\mathrm{u}/l,j}$ where i denotes the parameter index in the upper/lower distribution array and j denotes the tube number as per the labels shown in Figure 2.6(a). The values of the design variables corresponding to the baseline configuration are listed in Table 2.4. Bounds are imposed on the design variables to avoid unfeasible shapes and issues related to the intersection of the tube surfaces.

Table 2.4: Thickness values for the upper and lower profile of the baseline tube geometry (identical for all tubes).

Design Variable $(t_i^{\text{u/l}})$	Thickness [m]
t_1	3.284×10^{-4}
t_2	2.910×10^{-4}
t_3	5.204×10^{-4}
t_4	6.432×10^{-4}
t_5	3.468×10^{-4}
t_6	3.268×10^{-5}
t_7	1.000×10^{-9}
t ₈	6.391×10^{-6}

CONSTRAINTS

The geometric constraint imposed on the tube cross-section is computed using the shoelace formula [57]. According to this formula, for a given set of p vertices (x_i , y_i) of

any non-intersecting polygon, ordered in a clockwise or counterclockwise manner, the area a can be computed as:

$$a = \frac{1}{2} \left| \sum_{i=1}^{p-1} (x_i y_{i+1} + x_p y_1) - \sum_{i=1}^{p-1} (y_i x_{i+1} + y_p x_1) \right|.$$
 (2.9)

By this method, the area enclosed within a polygon is computed by the sum of the area of the triangles formed by the origin with two vertices of the polygon in a sequential order. Figure 2.7 illustrates the area calculation method for an arbitrary polygon with ten vertices arranged in the counterclockwise direction. The sensitivities of the area constraint with respect to the design variables are computed using the complex-step method.

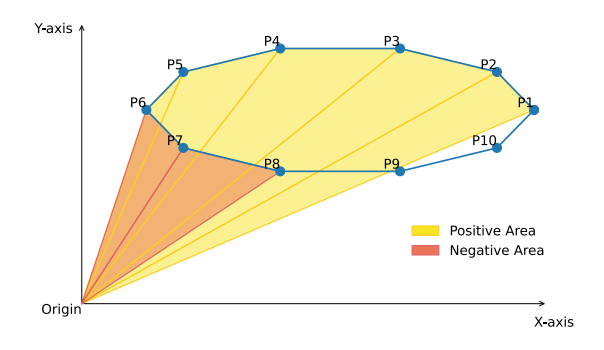


Figure 2.7: Illustration of the use of the shoelace method for calculating area of 2-D enclosed polygon.

2.4. RESULTS

2.4.1. Gradient verification

To verify the gradient values obtained using the adjoint (ADJ) method, they are compared to those computed using the first-order forward finite difference (FD) method. The step sizes chosen for the finite difference method were 0.05% and 0.01% for the cost functions of pressure drop and heat transfer rate, respectively. These values of step sizes were chosen after performing a parametric analysis. The value of the gradients of both the pressure drop and heat transfer rate with respect to the design variables $\left(\frac{\mathrm{d}f}{\mathrm{d}a}\right)$ computed with the two methods are displayed in Figure 2.8.

As seen from Figure 2.8, the gradient values for the cost functions computed by the adjoint method are quantitatively in agreement with those computed by the finite difference method. An average deviation of less than 5% was obtained for all the design variables, apart from $t_7^{u/l,j}$. For the chosen step size, the design variables $t_7^{u/l,j}$ show the largest discrepancies as their values are orders of magnitude smaller than the other design variables (see Table 2.4). Increasing the step size of the FD method would reduce the discrepancy observed for $t_7^{u/l,j}$, but would affect the gradient estimation for the other variables. For example, a step-size study performed for the first tube revealed that for $t_{3-5}^{u/l,1}$, decreasing the step size is required for reducing the discrepancies in the gradient values

for the pressure drop objective. For $t_4^{\mathrm{u/l},1}$, which has the largest discrepancy among design variables of the first tube (excluding $t_7^{\mathrm{u/l},1}$), a step-size reduction by an order of magnitude decreased the discrepancy from about 4.5% to about 0.7%. Overall, the gradients obtained using the design chain are deemed sufficiently accurate for the optimization study.

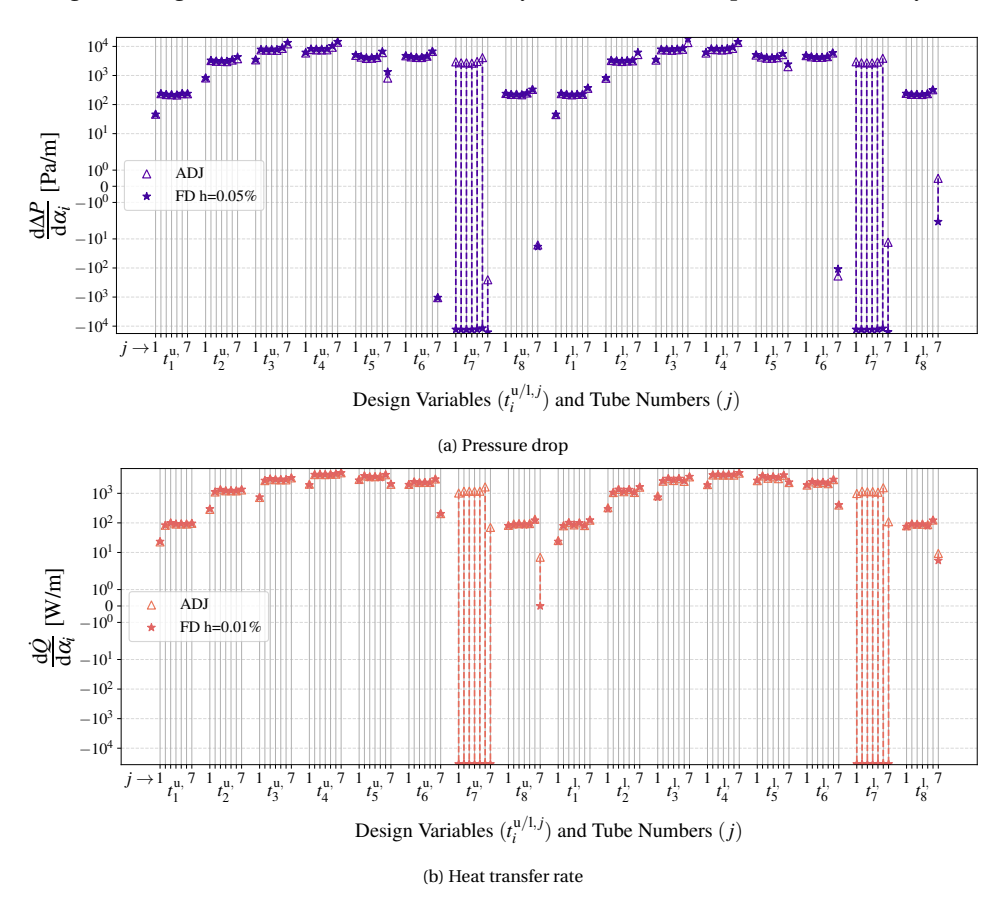


Figure 2.8: Gradient verification plots for the cost functions in the optimization case study.

2.4.2. OPTIMIZATION RESULTS

The optimization results are presented for the two cases described earlier in section 2.3: identical (CP-AS) and non–identical tubes (CP-LS). The plots in Figure 2.9 illustrate the convergence trend of the optimization problem. Both the objective function and the constraints are displayed. As can be observed, for the case with identical tubes, a 19.41% performance improvement is achieved in 11 design iterations. In the second case, instead, a reduction of total pressure loss of about 25% is obtained in 19 design iterations. The optimization converged after the SNOPT optimality tolerance of 10^{-6} was satisfied. The SNOPT feasibility metric reached values on the order of 10^{-9} and 10^{-12} for the identical and non-identical cases, respectively. The computational time required for each flow

33

2

and adjoint simulation was ~ 10 minutes on a workstation with *Intel Xeon Gold 5220R* (2.2 *GHz*) processor having 192 GB memory. The case with identical tubes leads to a faster optimization convergence due to fewer distinct design variables as a result of the sensitivity averaging. Furthermore, Figure 2.9 illustrates that the optimum design in the identical tubes case achieves a heat transfer rate about 0.5% lower than the baseline design, thereby not fully utilizing the allowed tolerance of about 1.5%. In both cases, however, the prescribed constraints on the heat transfer rate and the area enclosed within the tubes are satisfied by the optimization process. Thus, the pumping losses are reduced while maintaining the required heat transfer rate.

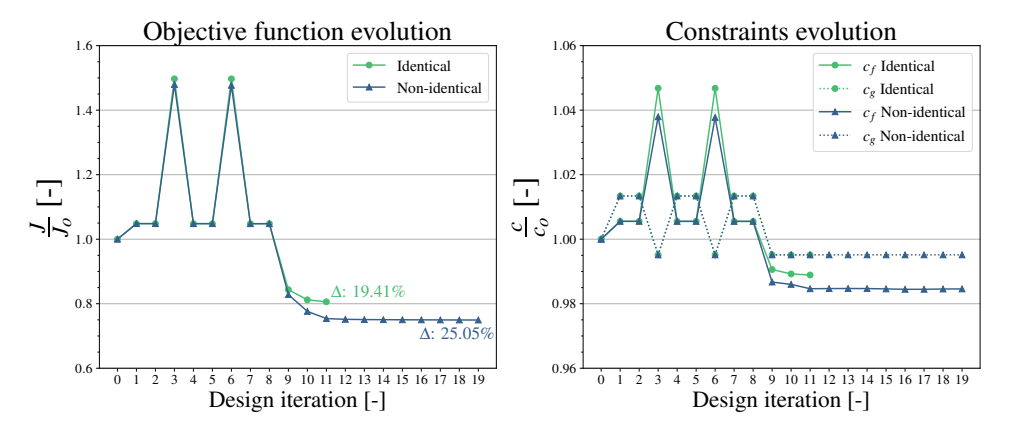


Figure 2.9: Optimization history plots depicting the evolution of cost functions with design iterations.

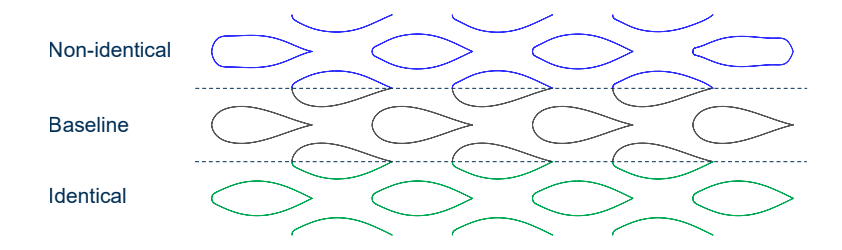


Figure 2.10: Comparison of the baseline tube bundle geometry with optimum designs having identical and non-identical tubes.

Figure 2.10 shows the baseline and optimal tube bundle configurations. Compared to the teardrop tube profile in the baseline design, the optimum solution with identical tubes exhibits a slender profile, leading to a more aerodynamic shape. The flow physics that result in pressure-drop reduction with the optimized design due to gradual thickness increase and reduced metal blockage are described in the subsequent paragraphs. In the non-identical tube case, a similar pattern is obtained for the shapes of tubes 2-6 (see tube labels in Figure 2.6(a)). Tubes 1 and 7 have different shapes, accounting for the local flow conditions, namely the entrance and exit effects for the tube bundle. Note that the optimized profiles of tubes 1 and 7 in the non-identical tube case appear largely mirrored,

apart from the differences at the leading and trailing edges. Tube 1 features a sharper trailing edge, while the leading edge of tube 7 is more rounded, which are the geometric characteristics that stem from the parametrization of the baseline geometry. This reflects the dependency of the optimized geometries on the baseline design, its parametrization, and the formulation of the optimization problem.

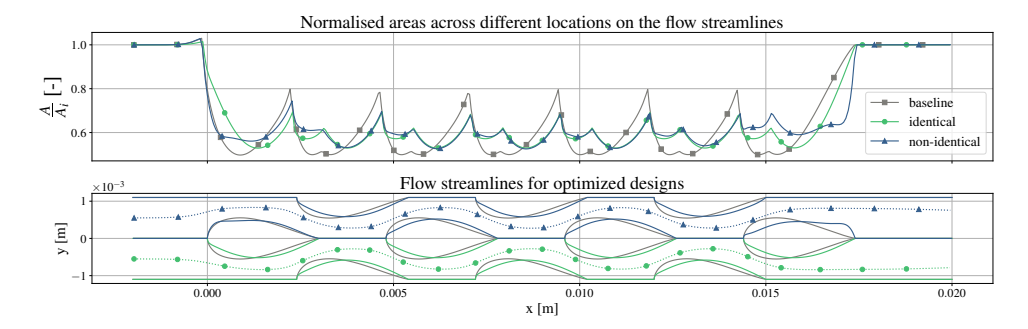


Figure 2.11: Comparison of the normalized flow passage area variation between the baseline design and the optimum designs having identical and non-identical tubes.

Figure 2.11 illustrates the variation of the normalized flow passage area in the streamwise direction for the three designs. As seen from Figure 2.11, the baseline design features a higher metal blockage, which induces higher velocity peaks, thus higher fluid-dynamic losses. The more significant geometrical differences between the two optimal designs are related to the geometry of the last tube, in particular, the slender profile of the last tube (Tube 7) featured in the non-identical configuration guarantees a more gradual flow diffusion process downstream of the tube bundle.

The contours of the flow properties - velocity, pressure, and temperature - for the three designs are shown in Figure 2.12. The velocity contours (see Figure 2.12(b)) substantiate the trends observed by the area-variation plot in Figure 2.11. The baseline design has higher velocities in the flow region between the end of a tube row and the leading edge of the following one compared to the optimum designs. Comparing the local velocities around the upstream half of Tube 7, it can be observed that the local velocity magnitudes are the lowest for the non-identical design. Moreover, the gradual increase of the tube thickness for the optimum designs eliminates the region of adverse pressure gradient observed in the baseline design due to the large curvature at the leading edge for the baseline tube shapes. Figure 2.12(a) depicts the pressure contours for the three designs where the flow stagnation regions can be qualitatively noted. The temperature contours for the designs are shown in Figure 2.12(c). Qualitatively the three different tube geometries result in similar temperature contours, as the heat transfer rate is constrained along with the internal area for each tube.

Furthermore, the flow properties are sampled at various locations along the streamlines as well as the tube surfaces. Figure 2.13 shows the flow properties - velocity, pressure, and temperature - at the locations A to E (see Figure 2.6(a)) in the flow domain. All the locations are equidistant from one another and locations B, C, and D are located at half of the chord length of the tubes 2, 4 and 6, respectively. As observed in the plots of the

2.4. RESULTS 35

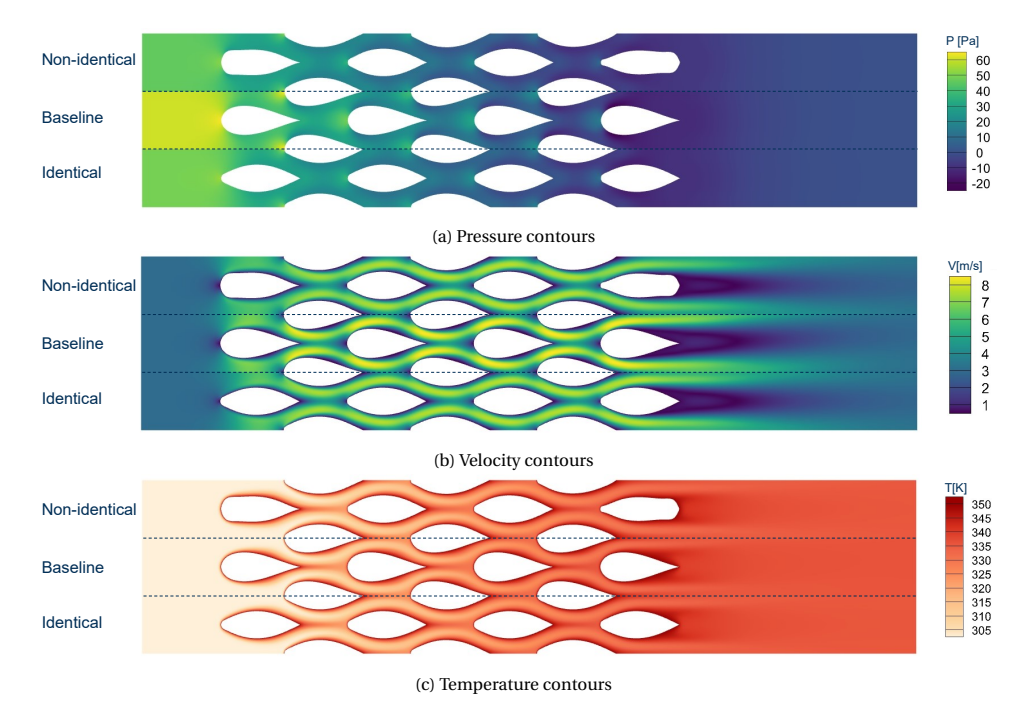


Figure 2.12: Comparison of pressure, velocity, and temperature fields between the baseline design and optimum designs with identical and non-identical tubes.

velocity field, the maximum observed velocity is reached at location D. The maximum velocity is the highest for the baseline design, while it is minimized by the design with non-identical tubes. At location C, the identical and non-identical tubes have similar peak velocity magnitudes which are lower than that estimated for the baseline geometry. The trend in the pressure drop across the tube bundle is the same for all the designs: the pressure drop is highest between locations A and B, and lowest between locations D and E. At locations D and E, the local gauge pressure values are negative, and the pressure recovery occurs after location E. The same consideration is applied to the temperature profiles as shown in Figure 2.13. The temperature rise across the tube ranks is nearly identical for all the designs implying that the average heat transfer coefficient does not change significantly with tube shape as the heat transfer rate is constrained.

The distribution of the pressure coefficient (C_p) and the heat flux (q'') on the surfaces of different tubes is displayed in Figure 2.14. The C_p distribution for the baseline design reveals a sharp drop of this quantity near the leading edge followed by a gradual increase, thus indicating that the region of adverse pressure gradient and flow deceleration extends till the rear-end of the tube. Conversely, for the optimum designs, the C_p decreases smoothly and stays relatively constant in the second half of tubes 3, 5, and 7. Tube 1 of the solution with non-identical tubes exhibits a sharper decrease in C_p at the leading edge than the identical tube, but the extent of the region with adverse pressure gradient is much smaller, resulting in lower drag forces. The heat flux for the optimum designs at

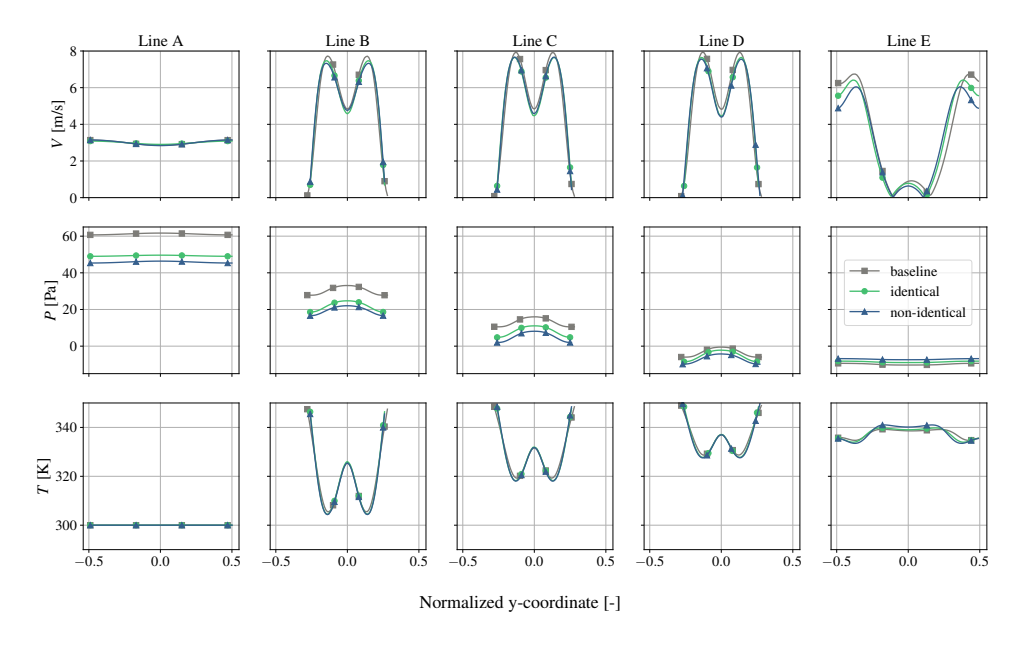


Figure 2.13: Variation of flow properties at different locations (A-E) in the flow domain.

tubes 3 and 5 exhibits overlapping distribution. In the case of tube 1, the average heat flux is the highest for the optimum solution with identical tubes, while for tube 7, the non-identical design results in higher heat flux values, though the difference in heat flux remains small.

2.4.3. Entropy generation analysis

To further compare the optimum designs, the fluid-dynamic performance of the different HEX configurations is characterized by performing a loss breakdown analysis based on entropy generation. The change of entropy along the flow path occurs because of irreversible processes associated with viscous dissipation and heat transfer across finite temperature differences, as well as due to reversible heat transfer. The total rate of entropy generation across an arbitrarily defined control volume can therefore be written as

$$\dot{S}_{\text{total}} = \dot{S}_{\text{irr}} + \dot{S}_{\text{rev}}.$$
 (2.10)

The rate of irreversible entropy generation is the result of two contributions: the first one (\dot{S}_{irr-ht}) due to the fact that the heat transfer occurs over a finite temperature difference, and the second one due to viscous stresses (\dot{S}_{visc}) . Therefore, the irreversible entropy generation can be written as

$$\dot{S}_{irr} = \dot{S}_{irr-ht} + \dot{S}_{visc}. \tag{2.11}$$

These two terms can be estimated for a two-dimensional flow field using the following equations [58],

$$\dot{S}_{\rm irr-ht}^{"'} = \frac{k}{T^2} \left[\left(\frac{\partial T}{\partial x} \right)^2 + \left(\frac{\partial T}{\partial y} \right)^2 \right], \tag{2.12}$$

37

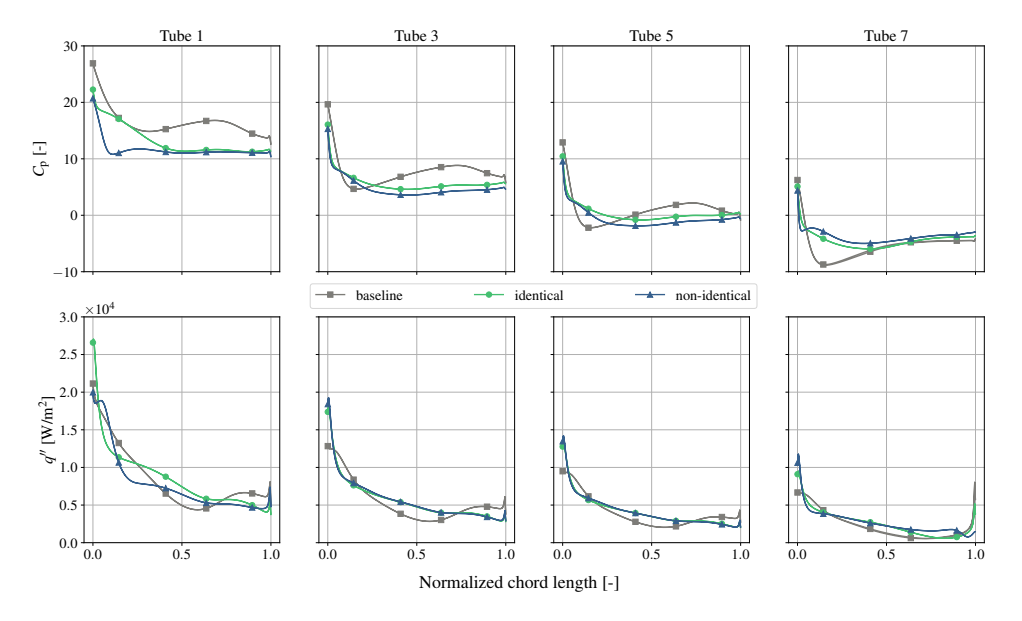


Figure 2.14: Comparison of the variation of pressure coefficient and heat flux on tube surfaces between the baseline design and the optimum designs.

$$\dot{S}_{\text{visc}}^{"'} = \frac{2\mu}{T} \left[\left(\frac{\partial u}{\partial x} \right)^2 + \left(\frac{\partial v}{\partial y} \right)^2 + \frac{1}{2} \left(\frac{\partial u}{\partial y} + \frac{\partial v}{\partial x} \right)^2 \right], \tag{2.13}$$

where \dot{S}''' indicates the volumetric rate of entropy generation, k is the effective thermal conductivity, μ is the effective dynamic viscosity, T is the temperature and (u,v) are the x,y components of velocity. The rate of entropy generation \dot{S} is computed by integrating \dot{S}''' over the control volume of interest. This integration is performed by multiplying local \dot{S}''' values by their corresponding mesh element areas and summing across the entire control volume, considering unit length in the z-direction.

The analysis of entropy generation across the tube bundle provides insight into the loss mechanisms occurring in the flow, the location of the highest irreversibilities, as well as the impact of shape optimization on their reduction. The rate of irreversible entropy generated in the computational domain for the three cases, estimated according to Eqn. (2.12) and Eqn. (2.13), are tabulated in Table 2.5. As can be seen from the table, the difference in \dot{S}_{irr-ht} between the baseline design and the optimum designs is less than 0.75%. This is because the heat transfer does not vary significantly among the design solutions, being constrained to the baseline value in the definition of the optimization problem. However, there is a significant difference in the \dot{S}_{visc} values. For the solution with identical optimum tubes, the entropy generation rate due to viscous dissipation is about 19% lower than that for the baseline, while for the non-identical case, the decrease is almost 25%. The obtained reductions are proportional to the differences in the pressure drop values.

Figure 2.15 shows the contour of the rate of entropy generation due to viscous stresses

Table 2.5: Irreversible entropy generation in the flow solution of the three designs due to heat transfer and viscous stresses

Case	$\dot{S}_{irr,ht}[W/K]$	$\dot{S}_{\rm irr,visc}[W/K]$
Baseline	7.761×10^{-2}	1.158×10^{-3}
Identical	7.727×10^{-2}	9.371×10^{-4}
Non-identical	7.712×10^{-2}	8.699×10^{-4}

 $(\dot{S}_{\mathrm{visc}}^{'''})$ for the three designs. Higher values of $\dot{S}_{\mathrm{visc}}^{'''}$ are observed within boundary layers in proximity of the regions where the flow acceleration is higher. This is especially visible in the region following the leading edges of the tubes. Additionally, the interface between the free stream and the wake features a higher rate of entropy generation, indicating mixing losses. To analyze the irreversible entropy increase along the flow path and the impact of each tube on loss generation, the computational domain is divided into four zones, as shown in Figure 2.15.

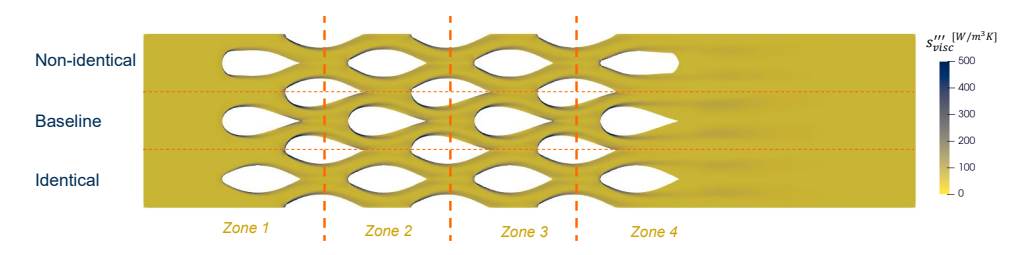


Figure 2.15: Volumetric entropy generation rate due to viscous dissipation and subdivision of the flow domain in the four zones used to analyze the irreversible entropy generation along the airflow path.

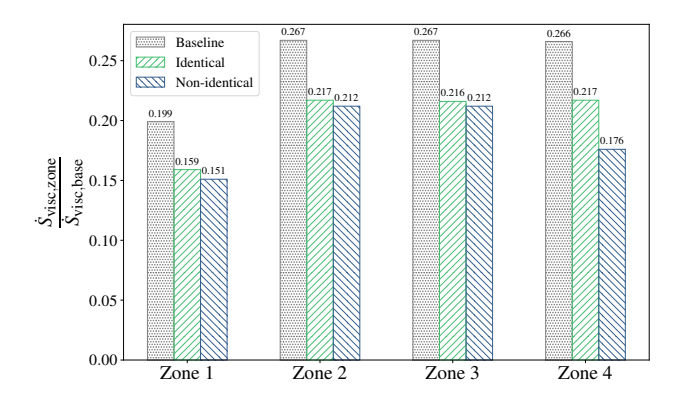


Figure 2.16: Zone-wise irreversible entropy generation due to viscous stresses normalized with respect to one in the entire computational domain for the baseline case.

The results are shown in the bar chart of Figure 2.16. The rate of entropy generation due to viscous effects in each zone ($\dot{S}_{visc,zone}$) and for each design is normalized with

respect to the overall entropy generation rate due to viscous shear computed for the baseline case ($\dot{S}_{visc,base}$). The optimized tube geometries minimize the entropy generation rate in each zone. In Zone 2 and Zone 3, there is no appreciable difference in the reduction of entropy generation for the optimal case with non-identical tubes versus the one with identical tubes. In Zone 1, the entropy generation rate for the optimum configuration with identical tubes is 20% lower compared to the baseline geometry, and 24% lower for that with non-identical tubes. Most of the decrease in entropy generation is attributed to the change of shape of the last tube. The reduction in entropy generation rate is, respectively, 18.4% and 33.8% compared to the baseline case. From these findings, it can be concluded that an adjoint-based optimization method, enabling the simultaneous and independent optimization of bare tubes, can lead to heat exchangers with significantly better thermal-hydraulic performance.

2.4.4. PITCH OPTIMIZATION

The potential of the framework described in section 2.2 to simultaneously optimize the shape and layout of the bare-tube heat exchangers was investigated. The motivation behind this work was to utilize the capability of CAD parametrization in characterizing the layout of the heat exchanger geometry and present the application of gradient-based optimization to design the shape and layout of bare-tube heat exchangers.

This study, documented in Ref. [59], included the longitudinal pitch in the design variables along with the thickness parameters of the tube geometry. The case study considered an in-line configuration of a bare-tube heat exchanger with the baseline design comprising tubes with an elliptical profile. The baseline configuration and the boundary conditions were selected based on the case study reported in section 2.3. The optimization objective was to minimize pressure drop while constraining the heat transfer rate and the internal area of the tubes.

The optimization process reduced the objective function by $\sim\!29\%$ while maintaining the constraint on the heat transfer rate set at 97% of its baseline value. Compared to the baseline design, the resulting optimal solution featured a tube shape with a larger width and shorter height, by about 18.5% each. Moreover, the longitudinal pitch ratio decreased by 25% compared to the baseline, thereby reducing the total volume of the tube bundle. The optimized design resulted in a reduction in the frontal area of the tubes, which led to a lower maximum velocity by about 11%.

While it is feasible to perform optimization of the shape and layout of thermal components in a computationally efficient manner using the proposed method, the key challenge noted was the deterioration of mesh quality due to large changes in the value of the longitudinal pitch. To facilitate the design process of simultaneously optimizing the shape and layout, suitable methods based on mesh regeneration need to be investigated.

2.5. CONCLUSIONS

The objective of this work was to propose a method to perform adjoint-based shape optimization of multiple heat transfer surfaces represented with a CAD-based parametrization. For this purpose, an automated design chain, consisting of the open-source CFD suite SU2 [38] and NURBS-based CAD parametrization [37], and implemented in a python-

based framework, was applied to an exemplary bare-tube heat exchanger. Using such a design chain, multiple heat transfer surfaces were optimized concurrently with the objective of reducing air-side pressure drop while constraining the heat transfer rate and the tube cross-section internal areas. Two variations of the optimization problem are investigated in the study: one utilizing averaged sensitivities and the other utilizing local sensitivities, resulting in an optimum solution with identical and non-identical tube shapes, respectively.

The conclusions from the research presented in this manuscript are as follows:

- 1. Optimum designs were obtained with 11 and 19 design iterations for the case with identical and non-identical tubes, respectively. The case with identical tubes leads to a faster optimization convergence due to fewer distinct design variables as a result of the sensitivity averaging.
- 2. The performance improvements for the cases with identical and non-identical tubes were 19.41% and 25.05% respectively. In the case of non-identical tubes, the first and the last tube in the streamwise direction exhibited a large difference in shape to optimize the flow cross-sectional area variation along the streamwise direction, thus leading to a smoother flow acceleration.
- 3. Zone-wise entropy generation analysis demonstrated that using the second law of thermodynamics helps identify the effect of individual tube shapes on performance improvement. The entropy generation due to viscous dissipation in Zone 4, containing the last full tube in the computational domain, was for the cases of identical and non-identical tubes 18.4% and 33.8% lower than the baseline, respectively.

Overall, using the proposed method, concurrent optimization of tubular HEX using local sensitivities, resulting in non-identical tube shapes, leads to higher design improvement when compared to identical shapes, with limited impact on the computation cost.

A key challenge faced in this study involving many design variables in the optimization process was linked with large mesh deformations in the intermediate design evaluations. One approach to tackle this challenge was setting appropriate bounds on design variables. Moreover, the mesh quality resulting from large mesh deformations is an important aspect that needs to be considered in future studies. Additionally, the layout of the tubes was kept fixed, so the effect of the tube bundle configuration on heat exchanger performance was not investigated in this study.

The next chapter will focus on simulating conjugate heat transfer for 3D shape optimization with CAD-based parametrization of heat transfer surfaces.

- [1] S. Kaiser, O. Schmitz, P. Ziegler, and H. Klingels, "The Water-Enhanced Turbofan as Enabler for Climate-Neutral Aviation", *Applied Sciences*, vol. 12, no. 23, 2022, ISSN: 2076-3417. DOI: 10.3390/app122312431.
- [2] M. Hughes and J. Olsen, "Fuel burn reduction of hybrid aircraft employing an exhaust heat harvesting system", *Journal of Propulsion and Power*, vol. 38, no. 2, pp. 241–253, 2022. DOI: 10.2514/1.B38393.
- [3] B. Sundén and J. Fu, "Chapter 6 aerospace heat exchangers", in *Heat Transfer in Aerospace Applications*, B. Sundén and J. Fu, Eds., Academic Press, 2017, pp. 89–115, ISBN: 978-0-12-809760-1. DOI: 10.1016/B978-0-12-809760-1.00006-5.
- [4] R. K. Shah and D. P. Sekulic, "Overview of heat exchanger design methodology", in *Fundamentals of Heat Exchanger Design*. John Wiley & Sons, Ltd, 2003, ch. 2, pp. 78–96, ISBN: 9780470172605. DOI: 10.1002/9780470172605.ch2.
- [5] M. Ahmadian-Elmi, A. Mashayekhi, S. S. Nourazar, and K. Vafai, "A comprehensive study on parametric optimization of the pin-fin heat sink to improve its thermal and hydraulic characteristics", *International Journal of Heat and Mass Transfer*, vol. 180, p. 121797, 2021, ISSN: 00179310. DOI: 10.1016/j.ijheatmasstransfer.2021.121797.
- [6] N. Tran and C. C. Wang, "Effects of tube shapes on the performance of recuperative and regenerative heat exchangers", *Energy*, vol. 169, pp. 1–17, 2019, ISSN: 03605442. DOI: 10.1016/j.energy.2018.11.127.
- [7] A. Sadeghianjahromi and C. C. Wang, "Heat transfer enhancement in fin-and-tube heat exchangers A review on different mechanisms", *Renewable and Sustainable Energy Reviews*, vol. 137, p. 110 470, 2021, ISSN: 18790690. DOI: 10.1016/j.rser.2020.110470.
- [8] L. Zhao, X. Gu, L. Gao, and Z. Yang, "Numerical study on airside thermal-hydraulic performance of rectangular finned elliptical tube heat exchanger with large row number in turbulent flow regime", *International Journal of Heat and Mass Transfer*, vol. 114, pp. 1314–1330, 2017, ISSN: 0017-9310. DOI: 10.1016/j.ijheatmasstran sfer.2017.06.049.
- [9] W. Xi, J. Cai, and X. Huai, "Numerical investigation on fluid-solid coupled heat transfer with variable properties in cross-wavy channels using half-wall thickness multi-periodic boundary conditions", *International Journal of Heat and Mass Transfer*, vol. 122, pp. 1040–1052, 2018, ISSN: 00179310. DOI: 10.1016/j.ijheatmasstransfer.2018.02.055.

- [10] N. Tran, Y. Chang, J. Teng, and R. Greif, "A study on five different channel shapes using a novel scheme for meshing and a structure of a multi-nozzle microchannel heat sink", *International Journal of Heat and Mass Transfer*, vol. 105, pp. 429–442, 2017, ISSN: 0017-9310. DOI: 10.1016/j.ijheatmasstransfer.2016.09.076.
- [11] N. Tran, J. Liaw, and C. Wang, "Performance of thermofluidic characteristics of recuperative wavy-plate heat exchangers", *International Journal of Heat and Mass Transfer*, vol. 170, p. 121 027, 2021, ISSN: 0017-9310. DOI: 10.1016/j.ijheatmass transfer.2021.121027.
- [12] X. Li, D. Zhu, Y. Yin, A. Tu, and S. Liu, "Parametric study on heat transfer and pressure drop of twisted oval tube bundle with in line layout", *International Journal of Heat and Mass Transfer*, vol. 135, pp. 860–872, 2019, ISSN: 0017-9310. DOI: 10.10 16/j.ijheatmasstransfer.2019.02.031.
- [13] P. Ranut, G. Janiga, E. Nobile, and D. Thévenin, "Multi-objective shape optimization of a tube bundle in cross-flow", *International Journal of Heat and Mass Transfer*, vol. 68, pp. 585–598, 2014, ISSN: 00179310. DOI: 10.1016/j.ijheatmasstransfer.2013.09.062.
- [14] S. Patankar, C. Liu, and E. M. Sparrow, "Fully developed flow and heat transfer in ducts having streamwise-periodic variations of cross-sectional area.", *Journal of Heat Transfer*, vol. 99, pp. 180–187, 1977. DOI: 10.1115/1.3450666.
- [15] D. Bacellar, V. Aute, Z. Huang, and R. Radermacher, "Design optimization and validation of high-performance heat exchangers using approximation assisted optimization and additive manufacturing.", *Science and Technology for the Built Environment*, vol. 23, no. 6, pp. 896–911, 2017. DOI: 10.1080/23744731.2017.13 33877.
- [16] H. Lim, U. Han, and H. Lee, "Design optimization of bare tube heat exchanger for the application to mobile air conditioning systems", *Applied Thermal Engineering*, vol. 165, p. 114 609, 2020, ISSN: 13594311. DOI: 10.1016/j.applthermaleng.2019.114609.
- [17] H. Kang, U. Han, H. Lim, H. Lee, and Y. Hwang, "Numerical investigation and design optimization of a novel polymer heat exchanger with ogive sinusoidal wavy tube", *International Journal of Heat and Mass Transfer*, vol. 166, p. 120785, 2021, ISSN: 00179310. DOI: 10.1016/j.ijheatmasstransfer.2020.120785.
- [18] J. Tancabel *et al.*, "Multi-scale and multi-physics analysis, design optimization, and experimental validation of heat exchangers utilizing high performance, non-round tubes", *Applied Thermal Engineering*, vol. 216, p. 118 965, 2022, ISSN: 13594311. DOI: 10.1016/j.applthermaleng.2022.118965.
- [19] J. Wen, H. Yang, G. Jian, X. Tong, K. Li, and S. Wang, "Energy and cost optimization of shell and tube heat exchanger with helical baffles using Kriging metamodel based on MOGA", *International Journal of Heat and Mass Transfer*, vol. 98, pp. 29–39, 2016, ISSN: 00179310. DOI: 10.1016/j.ijheatmasstransfer.2016.02.084.

[20] C. Liu, W. Bu, and D. Xu, "Multi-objective shape optimization of a plate-fin heat exchanger using CFD and multi-objective genetic algorithm", *International Journal of Heat and Mass Transfer*, vol. 111, pp. 65–82, 2017, ISSN: 0017-9310. DOI: 10.1016/j.ijheatmasstransfer.2017.03.066.

- [21] X. Wang, N. Zheng, Z. Liu, and W. Liu, "Numerical analysis and optimization study on shell-side performances of a shell and tube heat exchanger with staggered baffles", *International Journal of Heat and Mass Transfer*, vol. 124, pp. 247–259, 2018, ISSN: 0017-9310. DOI: 10.1016/j.ijheatmasstransfer.2018.03.081.
- [22] G. W. Mann and S. Eckels, "Multi-objective heat transfer optimization of 2D helical micro-fins using NSGA-II", *International Journal of Heat and Mass Transfer*, vol. 132, pp. 1250–1261, 2019, ISSN: 0017-9310. DOI: 10.1016/j.ijheatmasstransfer.20 18.12.078.
- [23] S. Soleimani and S. Eckels, "Multi-objective optimization of 3D micro-fins using NSGA-II", *International Journal of Heat and Mass Transfer*, vol. 197, p. 123 315, 2022, ISSN: 00179310. DOI: 10.1016/j.ijheatmasstransfer.2022.123315.
- [24] K. Hu, C. Lu, B. Yu, L. Yang, and Y. Rao, "Optimization of bionic heat sinks with self-organized structures inspired by termite nest morphologies", *International Journal of Heat and Mass Transfer*, vol. 202, p. 123735, 2023, ISSN: 00179310. DOI: 10.1016/j.ijheatmasstransfer.2022.123735.
- [25] Y. A. Manaserh, A. R. Gharaibeh, M. I. Tradat, S. Rangarajan, B. G. Sammakia, and H. A. Alissa, "Multi-objective optimization of 3D printed liquid cooled heat sink with guide vanes for targeting hotspots in high heat flux electronics", *International Journal of Heat and Mass Transfer*, vol. 184, p. 122 287, 2022, ISSN: 00179310. DOI: 10.1016/j.ijheatmasstransfer.2021.122287.
- [26] M. E. Polat and S. Cadirci, "Artificial neural network model and multi-objective optimization of microchannel heat sinks with diamond-shaped pin fins", *International Journal of Heat and Mass Transfer*, vol. 194, p. 123 015, 2022, ISSN: 00179310. DOI: 10.1016/j.ijheatmasstransfer.2022.123015.
- [27] J. R. R. A. Martins and A. Ning, Engineering Design Optimization. Cambridge, UK: Cambridge University Press, Jan. 2022, ISBN: 9781108833417. DOI: 10.1017/97811 08980647.
- [28] R. Zhang and X. Qian, "Parameter-free Shape Optimization of Heat Sinks", in *Proceedings of Intersociety Conference on Thermal and Thermomechanical Phenomena in Electronic Systems, ITherm*, Jul. 2020, pp. 756–765, ISBN: 9781728197647. DOI: 10.1109/ITherm45881.2020.9190501.
- [29] K. Wang, X. Y. Zhang, Z. D. Zhang, and C. H. Min, "Three-dimensional shape optimization of fins in a printed circuit recuperator using S-CO2 as the heat-transfer fluid", *International Journal of Heat and Mass Transfer*, vol. 192, p. 122910, Aug. 2022, ISSN: 00179310. DOI: 10.1016/j.ijheatmasstransfer.2022.122910.
- [30] J. L. Anibal, C. A. Mader, and J. R. Martins, "Aerodynamic shape optimization of an electric aircraft motor surface heat exchanger with conjugate heat transfer constraint", *International Journal of Heat and Mass Transfer*, vol. 189, p. 122 689, 2022, ISSN: 0017-9310. DOI: 10.1016/j.ijheatmasstransfer.2022.122689.

[31] J. L. Anibal and J. R. Martins, "Adjoint-based shape optimization of a plate-fin heat exchanger using CFD", *Applied Thermal Engineering*, vol. 252, p. 123570, 2024, ISSN: 1359-4311. DOI: 10.1016/j.applthermaleng.2024.123570.

- [32] K. T. Gkaragkounis, E. M. Papoutsis-Kiachagias, and K. C. Giannakoglou, "Adjoint-assisted Pareto front tracing in aerodynamic and conjugate heat transfer shape optimization", *Computers & Fluids*, vol. 214, p. 104753, 2021, ISSN: 0045-7930. DOI: 10.1016/j.compfluid.2020.104753.
- [33] S. Vitale, M. Pini, and P. Colonna, "Multistage turbomachinery design using the discrete adjoint method within the open-source software SU2", *Journal of Propulsion and Power*, vol. 36, no. 3, pp. 465–478, 2020, ISSN: 1533-3876. DOI: 10.2514/1.B37 685.
- [34] L. Mueller and T. Verstraete, "CAD integrated multipoint adjoint-based optimization of a turbocharger radial turbine", *International Journal of Turbomachinery, Propulsion and Power*, vol. 2, no. 3, 2017, ISSN: 2504186X. DOI: 10.3390/ijtpp203 0014.
- [35] N. Anand, S. Vitale, M. Pini, and P. Colonna, "Assessment of FFD and CAD-based shape parametrization methods for adjoint-based turbomachinery shape optimization.", in *Proceedings of Global Power and Propulsion Society, Montreal, Canada*, 2018, pp. 1–8. DOI: 10.5281/zenodo.1344595.
- [36] S. Xu, D. Radford, M. Meyer, and J.-D. Müller, "CAD-Based Adjoint Shape Optimisation of a One-Stage Turbine With Geometric Constraints", in *Proceedings of Turbo Expo: Power for Land, Sea, and Air*, vol. Volume 2C: Turbomachinery, Jun. 2015, V02CT45A006. DOI: 10.1115/GT2015-42237.
- [37] R. Agromayor, N. Anand, J. D. Muller, M. Pini, and L. O. Nord, "A unified geometry parametrization method for turbomachinery blades.", *Computer Aided Design*, vol. 133, no. 102987, pp. 1–16, 2021. DOI: 10.1016/j.cad.2020.102987.
- [38] T. D. Economon, F. Palacios, S. R. Copeland, T. W. Lukaczyk, and J. J. Alonso, "SU2: An open-source suite for multiphysics simulation and design", *AIAA Journal*, vol. 54, no. 3, pp. 828–846, 2016. DOI: 10.2514/1.J053813.
- [39] R. Agromayor, N. Anand, M. Pini, and L. O. Nord, "Multirow Adjoint-Based Optimization of NICFD Turbomachinery Using a Computer-Aided Design-Based Parametrization", *Journal of Engineering for Gas Turbines and Power*, vol. 144, no. 4, 2022, ISSN: 15288919. DOI: 10.1115/1.4052881.
- [40] A. Châtel and T. Verstraete, "Multidisciplinary optimization of the SRV2-O radial compressor using an adjoint-based approach", *Structural and Multidisciplinary Optimization*, vol. 66, no. 5, pp. 1–13, 2023, ISSN: 16151488. DOI: 10.1007/s00158-023-03556-2.
- [41] K. Gkaragkounis, E. Papoutsis-Kiachagias, and K. Giannakoglou, "The continuous adjoint method for shape optimization in conjugate heat transfer problems with turbulent incompressible flows", *Applied Thermal Engineering*, vol. 140, pp. 351–362, 2018.
- [42] Various Authors, Parablade, version v1.0, 2020. DOI: 10.5281/zenodo.3894778.

[43] A. B. Lambe and J. R. R. A. Martins, "Extensions to the Design Structure Matrix for the Description of Multidisciplinary Design, Analysis, and Optimization Processes", *Structural and Multidisciplinary Optimization*, vol. 46, pp. 273–284, 2012. DOI: 10.1007/s00158-012-0763-y.

- [44] P. E. Gill, W. Murray, and M. A. Saunders, "SNOPT: An SQP algorithm for large-scale constrained optimization", *SIAM Review*, vol. 47, no. 1, pp. 99–131, 2005. DOI: 10.1137/S0036144504446096.
- [45] N. Wu, G. Kenway, C. A. Mader, J. Jasa, and J. R. R. A. Martins, "pyOptSparse: A Python framework for large-scale constrained nonlinear optimization of sparse systems", *Journal of Open Source Software*, vol. 5, no. 54, p. 2564, 2020. DOI: 10.211 05/joss.02564.
- [46] W. Squire and G. Trapp, "Using complex variables to estimate derivatives of real functions", *SIAM Review*, vol. 40, no. 1, pp. 110–112, 1998. DOI: 10.1137/S003614 459631241X.
- [47] R. Dwight, "Robust mesh deformation using the linear elasticity equations", in *Computational Fluid Dynamics* 2006, Jan. 2009, pp. 401–406, ISBN: 978-3-540-92778-5. DOI: 10.1007/978-3-540-92779-2_62.
- [48] T. D. Economon, "Simulation and adjoint-based design for variable density incompressible flows with heat transfer", *AIAA Journal*, vol. 58, no. 2, pp. 757–769, 2020, ISSN: 00011452. DOI: 10.2514/1.J058222.
- [49] J. M. Weiss and W. A. Smith, "Preconditioning applied to variable and constant density flows", *AIAA Journal*, vol. 33, no. 11, pp. 2050–2057, Nov. 1995, ISSN: 1533-385X. DOI: 10.2514/3.12946.
- [50] B. van Leer, "Towards the ultimate conservative difference scheme. V. A second-order sequel to Godunov's method", *Journal of Computational Physics*, vol. 32, no. 1, pp. 101–136, 1979, ISSN: 0021-9991. DOI: 10.1016/0021-9991(79)90145-1.
- [51] J. Blazek, *Computational Fluid Dynamics: Principles and Applications*, Third. Oxford: Butterworth-Heinemann, 2015, pp. 163–165, ISBN: 978-0-08-099995-1. DOI: 10.1016/B978-0-08-099995-1.00005-1.
- [52] P. R. Spalart and S. R. Allmaras, "A one-equation turbulence model for aerodynamic flows", in *Proceedings of 30th Aerospace Sciences Meeting and Exhibit*, 1992, pp. 5–21. DOI: 10.2514/6.1992-439.
- [53] Y. Saad, *Iterative Methods for Sparse Linear Systems*, Second. Society for Industrial and Applied Mathematics, 2003. DOI: 10.1137/1.9780898718003.
- [54] M. Sagebaum, T. Albring, and N. R. Gauger, "High-Performance Derivative Computations using CoDiPack", *ACM Trans. Math. Softw.*, vol. 45, no. 4, 2019, ISSN: 0098-3500. DOI: 10.1145/3356900.
- [55] T. A. Albring, M. Sagebaum, and N. R. Gauger, "Efficient aerodynamic design using the discrete adjoint method in SU2", in *Proceedings of 17th AIAA/ISSMO Multidisci- plinary Analysis and Optimization Conference*, AIAA, 2016, ch. Shape and Topology Optimization III, pp. 1–15. DOI: 10.2514/6.2016–3518.

9

46 BIBLIOGRAPHY

[56] I. Pointwise, *Pointwise*, https://www.pointwise.com, version 18.5 R2, [Computer software], 2022.

- [57] B. Braden, "The surveyor's area formula", *The College Mathematics Journal*, vol. 17, no. 4, pp. 326–337, 1986. DOI: 10.1080/07468342.1986.11972974.
- [58] A. Bejan, "The thermodynamic design of heat and mass transfer processes and devices", *International Journal of Heat and Fluid Flow*, vol. 8, no. 4, pp. 258–276, 1987, ISSN: 0142727X. DOI: 10.1016/0142-727X(87)90062-2.
- [59] P. Pai Raikar, C. De Servi, O. Bociar, and N. Anand, "Shape and Layout Optimization of Bare-Tube Heat Exchangers Using the Adjoint Method and CAD-based Parametrization", in *Proceedings of the 9th World Congress on Momentum, Heat and Mass Transfer*, ser. MHMT 2024, Avestia Publishing, Apr. 2024. DOI: 10.11159/enfht24.219.

3

3D OPTIMIZATION OF HEAT SINK FINS

Parts of this chapter have been published in:

P. Pai Raikar, N. Anand, M. Pini, and C. De Servi, 3D optimization of heat sink fins using adjoint-based optimization with a CAD-based parametrization, International Journal of Heat and Mass Transfer 255 (2026) 127722. DOI: 10.1016/j.ijheatmasstransfer.2025.12772

Abstract

This chapter presents an automated shape optimization method for heat sinks. The computational framework has been developed by combining a conjugate heat transfer solver with adjoint capabilities, a CAD parametrization tool, and a gradient-based optimizer. The test case considers the design optimization of a water-cooled heat sink with pin fins, with the goal of concurrently enhancing heat transfer and minimizing pressure losses. Results show that the optimized fin geometry leads to an improvement of the average heat transfer coefficient by 24% while the pressure drop is lowered by 19%. The optimal fin array features an unconventional shape with an enlarged cross-section at the hub and the top with respect to mid-span, and a variation of the pin profile in the streamwise direction. The net effect is a reduction in flow blockage, an increase in fin efficiency, and a lower and more uniform temperature distribution in the heat sink base plate.

3.1. Introduction

The electrification of aircraft propulsion and power systems offers a promising solution for reducing carbon emissions in aviation [1]. However, to realize the potential of aircraft electrification, challenges related to the dissipation of thermal power generated by electric motors, batteries, and other electronic components must be addressed [2]. Thus, effective thermal management systems (TMS) are essential to enable the more electric aircraft of the future. The heat exchangers and heat sinks in such TMS must, therefore, be designed to handle significantly high thermal loads (estimated to be 2-10 kW/m 2 for batteries and 10-50 kW/m 2 for motors) while having minimum drag, low weight, and compact footprint [3].

The optimal design of heat exchangers and heat sinks of TMS is nowadays supported by high-fidelity numerical simulations, used either in parametric analyses or adopted in optimization studies [4]. The thermal-hydraulic performance of the components is evaluated with conjugate heat transfer (CHT) models, whereby relevant flow quantities (e.g., pressure drop, flow maldistribution) and heat transfer rates are predicted using three-dimensional RANS modeling [5], while the temperature distribution within the solid medium is determined by solving the energy equation [6].

Recently, the application of CHT models in parametric studies has led to the discovery of unconventional heat sink geometries with superior thermal-hydraulic performance. For example, Ahmadian-Elmi et al. [7] investigated the effect of pin fin geometric parameters – such as height, diameter, pitch, and taper angle – on the heat sink performance, defined as a function of the overall heat transfer coefficient and pressure drop. The results indicated that the fin shape has a major influence on the convective heat transfer coefficient and the pressure drop. More specifically, tapered pin fins showcased a performance improvement of 17% over conventional cylindrical pin fins. Similarly, Kim et al. [8] performed a parametric study to identify an optimum shape for the fins of the oil cooler of an aero gas-turbine engine. The fin geometry leading to the highest performance featured a forward-slanted profile that accelerated the flow near the bottom of the fin and enhanced local heat transfer. However, parametric studies such as the ones documented in Ref. [7, 8] are impractical to explore comprehensively all the design options.

Optimized designs of heat transfer components can be achieved by coupling CHT simulations with an optimization algorithm. Two coupling strategies are generally pursued

49

3

to limit the computational burden of the optimization problem. The first one requires the derivation of a surrogate of the CFD or CHT model of the heat transfer device under design. The optimization is then performed using a gradient-free evolutionary algorithm. The second strategy consists of directly coupling a 3D CHT model with a gradient-based optimization algorithm. The first approach provides a suitable trade-off between accuracy and computational cost for optimization problems with a number of design variables in the order of 10-20, as the computational time required to generate the dataset for the implementation of the surrogate model significantly increases with the number of design variables. Hu et al. [9] optimized a 3D heat sink using a gradient-free method based on an evolutionary algorithm to reduce pressure drop along with temperature hotspots and non-uniformities. More recently, Nguyen et al. [10] utilized a surrogate model constructed with the machine-learning algorithm called random decision forests to optimize the three-dimensional shape of pin fins. The design variables consisted of the radii along the pin span, and the optimization resulted in funnel-shaped fins featuring a 20% higher heat transfer coefficient compared to the conventional cylindrical pins for the same pressure drop. Other studies have employed surrogate models based on artificial neural networks to design heat sinks with elliptical [11] and diamond-shaped [12] pin fins.

Gradient-based optimization methods with sensitivities obtained using the adjoint method are known to be very efficient for large-scale design problems with constraints [13]. In the context of shape optimization for conjugate heat transfer problems, Gkaragkounis et al. [14] developed a continuous adjoint CHT solver for turbulent flows and applied it to perform the 2D and 3D optimization of cooling channels of turbines blades and piston-engines. Using the same adjoint-based computational framework, Gkaragkounis et al. [15] performed the multi-objective shape optimization of 3D heat sink fins, minimizing pressure drop and temperature hotspots. The result of the numerical exercise was a Pareto front constituted by a set of novel fin designs. Conversely, Anibal et al. [16] used the discrete adjoint formulation to compute the sensitivities and to carry out the optimal design of heat sinks for thermal management of electric motors in aerospace applications. The results highlighted the importance of modeling the thermal interaction between the solid and the fluid with a conjugate heat transfer solver, as opposed to approaches modeling the fluid domain only. Similarly, Burghardt et al. [17] developed a discrete adjoint methodology for performing shape optimization in conjugate heat transfer problems, and implemented it leveraging the open-source software SU2. The method was applied to the optimal design of the 2D profile of a pin fin array and the cooling slots of a turbine blade. Recently, He et al. [18] applied discrete adjoint-based shape optimization to improve the cooling of battery cells. The CFD model domain encompassed an airflow channel and the aluminum casing surrounding each cell. To solve the corresponding aerothermal problem, a conjugate heat transfer analysis was performed by integrating a finite-volume fluid dynamics solver for the fluid domain with a conduction heat transfer solver for the solid domain, using the OpenMDAO-based MPhys framework. The optimized casing geometry reduces both the pumping losses associated with the airflow and the weight of the unit compared to the baseline cylindrical design, while still satisfying the constraints on the maximum temperature of the battery cells.

In all the aforementioned adjoint-based studies, the design surfaces were parameter-

ized using methods based on Free-Form Deformation (FFD) boxes, which provide large design flexibility. However, parametrization based on FFD boxes does not easily allow imposing geometric constraints, such as those required for manufacturability [19, 20]. In contrast, CAD-based parametrization with NURBS control points offers precise control and accurate representation of the design surface to define geometric constraints [21, 22]. Yet, limited studies have focused on the application of CAD-based adjoint optimization in conjugate heat transfer problems. Chávez-Modena et al. [23] utilized a 2D parametrization based on control points to design a heat exchanger using a framework that sequentially optimizes the layout of the fins and then their shape. The optimized geometry was then extruded in 3D and simulated with a conjugate heat transfer solver, demonstrating a performance improvement of more than 10%. Imam-Lawal [24] optimized a U-bend internal cooling channel, whose thermal-hydraulic performance was computed with a CHT solver and its 3D geometry was parametrized by NURBS and rational Bezier curves. In a recent work, Pai Raikar et al. [25] proposed a CAD-based adjoint optimization framework to concurrently design multiple heat transfer surfaces and applied it to the optimal design of bare-tube heat exchangers, with the goal of minimizing pressure drop while constraining the heat transfer rate. However, the optimization framework in Ref. [25] neglected the modeling of the temperature distribution within the solid surfaces. In summary, the potential of CHT-based adjoint optimization for the optimal design of 3D heat transfer surfaces with CAD-based parametrization has not been investigated yet.

This study presents an adjoint-based optimization method relying on a conjugate heat transfer solver implemented in the open-source CFD software SU2 [26] and a CAD-based parametrization tool [27] based on NURBS to identify the optimal 3D shape of heat sinks. The objective is achieved by extending the automated design framework presented in Ref. [25] to conjugate heat transfer problems. The test case considered in this study involves the application of the shape optimization method to the design of a heat sink with pin fins, with the objective of concurrently maximizing the heat transfer coefficient and minimizing total pressure losses.

3.2. METHODOLOGY

The optimization framework encompasses the open-source CFD software SU2 [26] for conjugate heat transfer simulation and gradient calculation with the discrete adjoint method, a mesh deformation algorithm, a CAD-based parametrization tool [27, 28], and a gradient-based optimizer.

The XDSM diagram [29] as shown in Figure 3.1 illustrates the optimization framework. The framework is similar to the one reported in Chapter 2, with the addition of conjugate heat transfer (CHT) simulation capabilities, leveraging the partitioned approach in SU2, whereby the solid and the fluid domains are discretized with two distinct grids. In the design chain, the heat transfer design surfaces, such as pin fins, are parametrized by a set of design variables (α). The design surfaces at the interface of the fluid and solid domain, i.e. $\mathbf{X}_{\text{surf,f}}$ and $\mathbf{X}_{\text{surf,s}}$, respectively, are updated at each design iteration. The corresponding volume meshes ($\mathbf{X}_{\text{vol,f}},\mathbf{X}_{\text{vol,s}}$) are obtained by deforming the initial grids, i.e., those generated for meshing the solid and fluid domain. CHT simulation is performed with SU2 to compute the values of the objective function (J) and constraints (\mathbf{c}). Next, the adjoint variables ($\boldsymbol{\Phi}_{\mathbf{f}},\boldsymbol{\Phi}_{\mathbf{s}}$) are computed using the coupled CHT adjoint solver. Finally, the

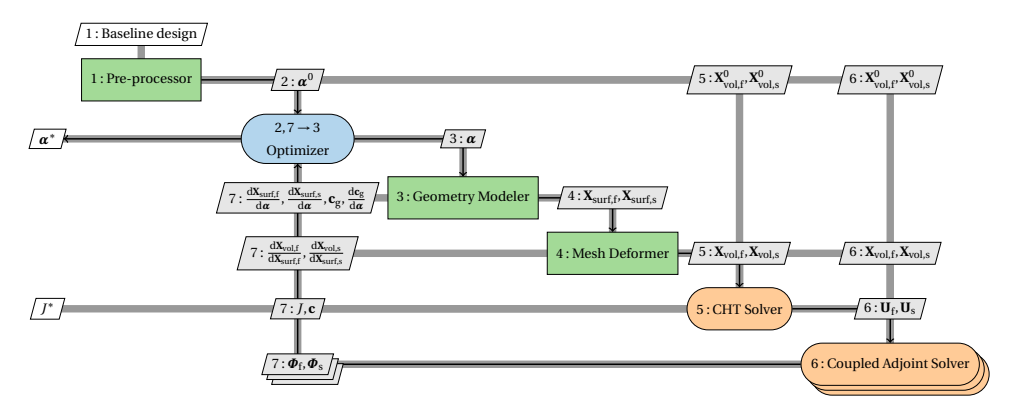


Figure 3.1: XDSM diagram depicting the inter-dependencies among the blocks of the optimization framework.

gradient values of the cost functions with respect to the design variables (α) are computed by applying the chain rule of differentiation, described in subsection 3.2.3.

The gradient-based optimizer used in the design chain is the Sparse Nonlinear OPTimizer (SNOPT) [30], which is interfaced by means of the open-source python package *pyOptSparse* [31]. Mesh deformation is performed for each domain by solving the linear elasticity equations [32] with the surface displacements of the corresponding design surfaces imposed as a Dirichlet boundary condition. For brevity, only the methods at the basis of the functional blocks concerning 3D CHT problems, namely, the Geometry Modeler, the CHT Solver, and the Coupled Adjoint Solver, are described in detail. Further details are documented in Ref. [25, 27].

3.2.1. GEOMETRY MODELER

The CAD-based parametrization method from Ref. [27] is applied to model 3D geometries of heat transfer surfaces such as fins. The parametrization method enables the construction of a variety of geometries with NURBS surfaces that satisfy G-2 continuity. Figure 3.2 illustrates the geometry construction method for an exemplary pin fin: a design surface is characterized by two independent thickness distributions imposed perpendicular to a camber surface. The camber surface is defined as a bi-quartic B-Spline surface [33] defined by a set of control points, the number of which can be selected based on the complexity of the geometry. Likewise, the thickness distributions determine the upper and lower profiles built around that camber surface. These profiles are defined using fourth-order B-spline surfaces whose parameters are listed in Table 3.1. Note that the control point weights are set to unity in this study. The sensitivities of a pin surface with respect to the design variables are computed using the second-order accurate complex-step method. The equations defining the surfaces parametrized through the CAD modeler are documented in Ref. [27]. These analytical expressions are also used to compute the values of the geometric constraints (\mathbf{c}_g) and their sensitivities $\left(\frac{d\mathbf{c}_g}{d\pmb{\alpha}}\right)$. The adopted CAD parametrization method is suitable for modeling geometries such as cylindrical, elliptical, and tapered fins, as well as unconventional heat transfer surfaces like teardrop and airfoiltype profiles, including three-dimensional variations of these shapes. However, it should be noted that this method is not applicable for parameterizing the geometry of perforated pins, wavy or louvered fins, and more complex topological structures such as fractal fins.

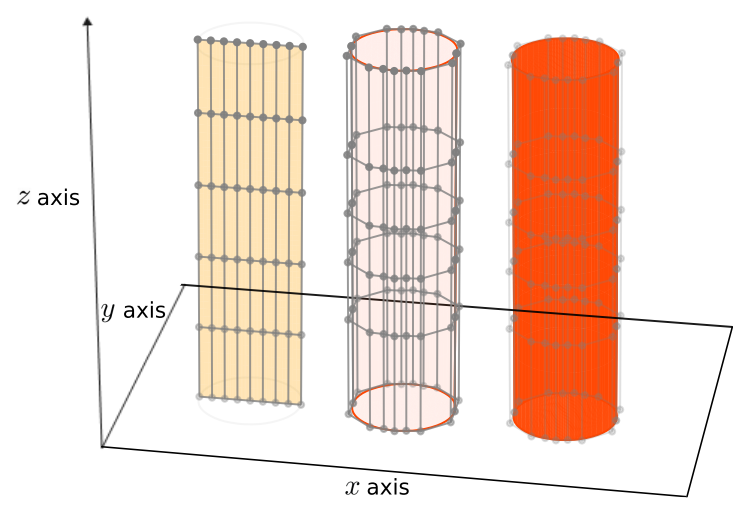


Figure 3.2: Construction of the 3D geometry of an exemplary pin fin using the camber-thickness CAD parametrization approach. The camber surface (left) is characterized by the design variables associated with the coordinates of its control points, in particular those at the leading and trailing edge $(x_{le}, z_{le}, y_{le}, x_{te}, z_{te})$. The thickness distributions (t^u, t^l) determine the control points of the lower and upper pin profiles (middle) that characterize the overall design surface (right).

3.2.2. CHT SOLVER

The conjugate heat transfer analyses are performed leveraging the partitioned approach in SU2 for solving coupled solid-fluid problems. In this approach, the flow is simulated using the incompressible RANS solver with the density-based approach, while heat conduction within the solid is computed by solving the energy equation. At the interface between the fluid and solid domain, the coupling conditions are represented by the Dirichlet boundary condition in the fluid domain, which prescribes a temperature equal to that of the solid at the interface, and the Robin boundary condition in the solid domain, which sets a heat flux proportional to a priori heat transfer coefficient and a temperature difference between the fluid and solid side [34]. The discretized form of the equations is obtained using the finite volume method with various numerical schemes available within SU2, as reported in Ref. [35]. The CHT solution state $\mathbf{U} = (\mathbf{U_f}, \mathbf{U_s})$ is obtained using the block-Gauss-Sieldel algorithm till convergence is reached for the coupled system.

3.2.3. COUPLED ADJOINT SOLVER

The gradient computation is performed by using a discrete adjoint method for the coupled system, developed using the reverse mode of the open-source algorithmic differentiation (AD) tool CoDiPack [36]. The adjoint equations are solved using the same discretization schemes as those used in the primal solver, and their solutions exhibit similar convergence behavior as that of the flow equations.

Table 3.1: Design variables needed for the three-dimensional parametrization of fin surfaces with the camber-	
thickness approach.	

Variable name	Symbol
Number of span-wise sections	$N_{\rm span}$
Number of chord-wise sections	$N_{ m chord}$
Leading edge control points	$x_{\mathrm{le}}, z_{\mathrm{le}}$
Leading edge abscissa	y_{le}
Trailing edge control points	$x_{\text{te}}, z_{\text{te}}$
Stagger angle	ξ
Inlet and exit metal angles	$\theta_{\mathrm{in}}, \theta_{\mathrm{out}}$
Inlet and exit tangent proportions	$\zeta_{\mathrm{in}}, \zeta_{\mathrm{out}}$
Inlet and exit radii of curvature	$r_{\rm in}, r_{\rm out}$
Upper and lower thickness distributions	t^{u} , t^{l}

To compute the sensitivities of the cost functions (J, \mathbf{c}) with respect to the design variables (α) , the optimization problem can be expressed (similar to Ref. [37, 38]) in the Lagrangian formulation as

$$\mathcal{L}(\boldsymbol{\alpha}, \mathbf{X}_{\text{vol,f}}, \mathbf{X}_{\text{vol,s}}, \mathbf{U}_{\text{f}}, \mathbf{U}_{\text{s}}, \boldsymbol{\lambda}_{\text{f}}, \boldsymbol{\lambda}_{\text{s}}, \boldsymbol{\sigma}_{\text{f}}, \boldsymbol{\sigma}_{\text{s}}) = J(\mathbf{X}_{\text{vol,f}}, \mathbf{X}_{\text{vol,s}}, \mathbf{U}_{\text{f}}, \mathbf{U}_{\text{s}})$$

$$+ \boldsymbol{\lambda}_{\text{f}}^{\text{T}} [\mathcal{G}_{\text{f}}(\mathbf{X}_{\text{vol,f}}, \mathbf{U}_{\text{f}}, \mathbf{U}_{\text{s}}) - \mathbf{U}_{\text{f}}] + \boldsymbol{\lambda}_{\text{s}}^{\text{T}} [\mathcal{G}_{\text{s}}(\mathbf{X}_{\text{vol,s}}, \mathbf{U}_{\text{f}}, \mathbf{U}_{\text{s}}) - \mathbf{U}_{\text{s}}]$$

$$+ \boldsymbol{\sigma}_{\text{f}}^{\text{T}} [\mathcal{M}_{\text{f}}(\boldsymbol{\alpha}) - \mathbf{X}_{\text{vol,f}}] + \boldsymbol{\sigma}_{\text{s}}^{\text{T}} [\mathcal{M}_{\text{s}}(\boldsymbol{\alpha}) - \mathbf{X}_{\text{vol,s}}], \quad (3.1)$$

where $\mathbf{U}=(\mathbf{U}_f,\mathbf{U}_s)$ represents the solution state defined by the fixed-point iterators \mathcal{G}_f and \mathcal{G}_s , \mathcal{M}_f and \mathcal{M}_s are the mesh mapping operators. Finally, the Lagrange multipliers (adjoint states) are represented by $\boldsymbol{\lambda}_f,\boldsymbol{\lambda}_s,\boldsymbol{\Phi}_f,\boldsymbol{\Phi}_s$, where the subscript denotes the zone index.

By following the derivation approach documented in Ref. [37] and differentiating the Lagrangian function (\mathcal{L}) with respect to its variables, the adjoint equations can be derived as

$$\lambda_{j}^{\mathrm{T}} = \frac{\partial J}{\partial \mathbf{U}_{j}} + \sum_{i=\mathrm{f,s}} \lambda_{i}^{\mathrm{T}} \frac{\partial \mathcal{G}_{i}}{\partial \mathbf{U}_{j}} \quad \text{for } j = \mathrm{f,s},$$
(3.2)

$$\boldsymbol{\Phi}_{j}^{\mathrm{T}} = \frac{\partial J}{\partial \mathbf{X}_{\mathrm{vol},j}} + \boldsymbol{\lambda}_{j}^{\mathrm{T}} \frac{\partial \mathcal{G}_{j}}{\partial \mathbf{X}_{\mathrm{vol},j}} \quad \text{for } j = f, s,$$
(3.3)

where the adjoint states account for the coupling of physics in the fluid and solid domains. The solution to Equation 3.2 can be obtained by following the iterative approach documented in Ref. [17, Sec. 3.2], which utilizes reverse mode of AD and block-Gauss-Seidel iterations. The gradient of the objective function with respect to the design variables is obtained by

$$\frac{\mathrm{d}J}{\mathrm{d}\boldsymbol{\alpha}} = \boldsymbol{\Phi}_{\mathrm{f}}^{\mathrm{T}} \frac{\mathrm{d}\mathcal{M}_{\mathrm{f}}}{\mathrm{d}\boldsymbol{\alpha}} + \boldsymbol{\Phi}_{\mathrm{s}}^{\mathrm{T}} \frac{\mathrm{d}\mathcal{M}_{\mathrm{s}}}{\mathrm{d}\boldsymbol{\alpha}}.$$
 (3.4)

The total derivative of the mesh mapping operator for each zone with respect to the

design variables can be calculated using the chain rule as

$$\frac{\mathrm{d}\mathcal{M}}{\mathrm{d}\boldsymbol{\alpha}} = \frac{\mathrm{d}\mathbf{X}_{\mathrm{vol}}}{\mathrm{d}\mathbf{X}_{\mathrm{surf}}} \cdot \frac{\mathrm{d}\mathbf{X}_{\mathrm{surf}}}{\mathrm{d}\boldsymbol{\alpha}},\tag{3.5}$$

where $\frac{dX_{vol}}{dX_{surf}}$ is the sensitivity of the volume mesh coordinates with respect to the surface coordinates and $\frac{dX_{surf}}{d\alpha}$ represents the sensitivity of the surface coordinates with respect to the design variables. Thus, the sensitivity of the objective function with respect to the design variables can be computed as

$$\frac{\mathrm{d}J}{\mathrm{d}\boldsymbol{\alpha}} = \boldsymbol{\Phi}_{\mathrm{f}} \cdot \frac{\mathrm{d}\mathbf{X}_{\mathrm{vol,f}}}{\mathrm{d}\mathbf{X}_{\mathrm{surf,f}}} \cdot \frac{\mathrm{d}\mathbf{X}_{\mathrm{surf,f}}}{\mathrm{d}\boldsymbol{\alpha}} + \boldsymbol{\Phi}_{\mathrm{s}} \cdot \frac{\mathrm{d}\mathbf{X}_{\mathrm{vol,s}}}{\mathrm{d}\mathbf{X}_{\mathrm{surf,s}}} \cdot \frac{\mathrm{d}\mathbf{X}_{\mathrm{surf,s}}}{\mathrm{d}\boldsymbol{\alpha}}.$$
(3.6)

3.3. CASE STUDY

The automated design framework is applied to the shape optimization of a heat sink with pin fins. This case study is inspired by Ref. [10], where pin fin shapes are optimized to enhance the thermal-hydraulic performance of a water-cooled heat sink operating under uniform heat flux.

3.3.1. HEAT SINK GEOMETRY

The baseline geometry of the heat sink consists of two rows of cylindrical pin fins in a staggered arrangement, with each row consisting of 7 pins. Figure 3.3 illustrates the heat sink geometry, and its dimensions are listed in Table 3.2.

Table 3.2: Geometry parameters defining the configuration of the heat sink.

Parameter	Description	Value [×10 ⁻³ m]
d	Pin fin diameter	4.0
Н	Height	20.0
W	Width	20.0
L	Length	100.0
pt_{lg}	Longitudinal pitch	13.0
pt _{tv}	Transverse pitch	7.0

3.3.2. Numerical model

Conjugate heat transfer simulation is performed on the computational domain shown in Figure 3.3. A uniform velocity of 0.13 m/s and a temperature of 300 K are prescribed at the inlet boundary of the fluid domain. A gauge pressure of 0 Pa is imposed at the outlet boundary, implying atmospheric pressure conditions. No-slip condition is prescribed at the interface between the fluid and the solid domain through the CHT coupling described in subsection 3.2.2. A uniform heat flux (q_b'') of 50,000 W/m² is applied to the bottom heated surface, which corresponds to an overall heat load of 100 W. The rest of the walls are modeled as adiabatic surfaces. The material properties of water in the fluid domain and aluminum in the solid domain are assumed to be constant and are reported in Table 3.3.

55

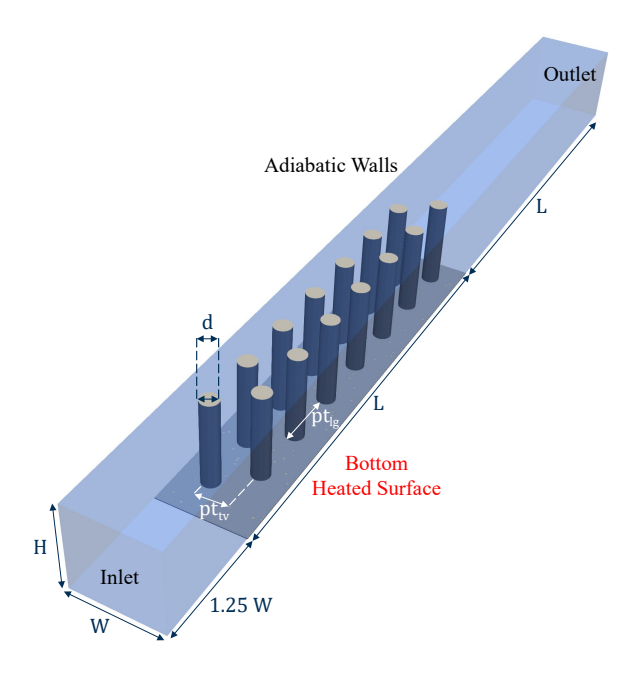


Figure 3.3: Computational domain (with boundary markers and geometry parameters) corresponding to the baseline design.

Table 3.3: Thermo-physical properties of water and aluminum.

Material	Density (ρ) [kg/m³]	Specific Heat (C_p) $[J/(kg \cdot K)]$	Viscosity (μ) [Pa·s]	Thermal Conductivity (k) $[W/(m \cdot K)]$
Water	997	4182	0.85×10^{-3}	0.6
Aluminum	2700	897		237

The flow conditions correspond to a Reynolds number of about 3050, considering the hydraulic diameter of the flow channel

$$D_{\rm h} = \frac{4{\rm WH}}{2({\rm W} + {\rm H})},\tag{3.7}$$

as the characteristic length. The turbulence is modeled using the one-equation Spalart-Allmaras model, which has a proven accuracy for heat transfer problems in internal flows [39].

The convective fluxes were reconstructed using the Flux-Difference-Splitting scheme with the MUSCL approach for second-order accuracy in the discretized form of the low-Mach flow equations documented in Ref. [35]. The scalar upwind method was used for the convective fluxes of the turbulent equations. The Green–Gauss method was used to compute the spatial gradients for both solid and fluid domains. The steady-state solutions were obtained using a time-marching method using the Euler implicit time integration, with a CFL of 40. The linearized governing equations of the coupled system were solved

using the FGMRES method with ILU preconditioning [35]. The maximum number of iterations per cycle of the linear solver for the fluid domain was 10 with a convergence tolerance of 10^{-4} , while for the solid domain, their values were 5 and 10^{-15} . To obtain the coupled solutions using the block-Gauss-Seidel algorithm, 12000 iterations were performed. This setup achieved a residual reduction of 10 orders of magnitude for the pressure and velocity state variables, and 5 orders of magnitude for the temperature variables in both fluid and solid domains. Although further residual reduction could be obtained with additional iterations, the limit of 12000 iterations was chosen as a trade-off between computational cost and solution accuracy. With this setting, a Cauchy convergence criterion of 10^{-7} was satisfied for all relevant thermal-hydraulic quantities.

3.3.3. GRID INDEPENDENCE STUDY AND MODEL VALIDATION

To perform the grid independence study, three hybrid unstructured meshes, consisting of hexahedral and prismatic elements, were generated using a commercial meshing tool [40]. The 3D meshes were generated by extruding 2D meshed surfaces along the height of the domain following a non-uniform progression as shown in Figure 3.5. In the fluid domain, the hexahedral elements are clustered around the walls to ensure y^+ values of less than 1. The mesh refinement was performed by following a consistent approach that led to approximately doubling the total number of mesh elements across different meshes while keeping the inflation layer thickness and its progression fixed.

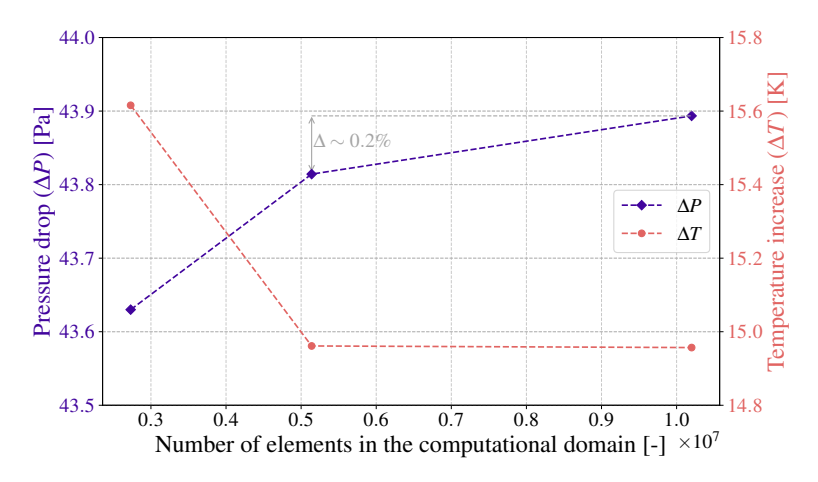


Figure 3.4: Variation of performance parameters with mesh density.

The variation of the relevant thermal-hydraulic quantities – temperature increase (ΔT) and pressure drop (ΔP) – with mesh density was investigated in the grid independence study. The temperature increase (ΔT) is computed as the difference between the average temperature of the heated surface ($T_{\rm avg}$) and the free-stream fluid temperature and is given by

$$\Delta T = T_{\text{avg}} - T_{\text{in}},\tag{3.8}$$

where $T_{\rm in}$ is the water temperature at the inlet, and it approximates the free-stream temperature since the increase in water temperature in the flow domain is rather limited.

3.3. CASE STUDY 57

Hence, ΔT can be related to the average heat transfer coefficient of the heat sink when applying constant heat flux. Lower values of ΔT and $T_{\rm avg}$ correspond to a higher convective heat transfer coefficient. Furthermore, the so-called pumping losses are estimated from the pressure drop computed by

$$\Delta P = P_{\rm in} - P_{\rm out}. \tag{3.9}$$

The variation of ΔT and ΔP is depicted in Figure 3.4, which shows a monotonic convergence of their values with the increase in mesh density. It can be observed that the mesh consisting of 5.1 million elements resulted in a deviation of approximately 0.18% and 0.03% in ΔP and ΔT values, compared to the finest mesh. Therefore, the mesh of 5.1 million elements (shown in Figure 3.5) was selected for the optimization study.

Additionally, the values of ΔP and ΔT obtained using the grid-independent mesh were compared with the experimental results derived from Ref. [41]. The comparison showed good agreement, with the results from the numerical model falling within the experimental uncertainty band of 4%.

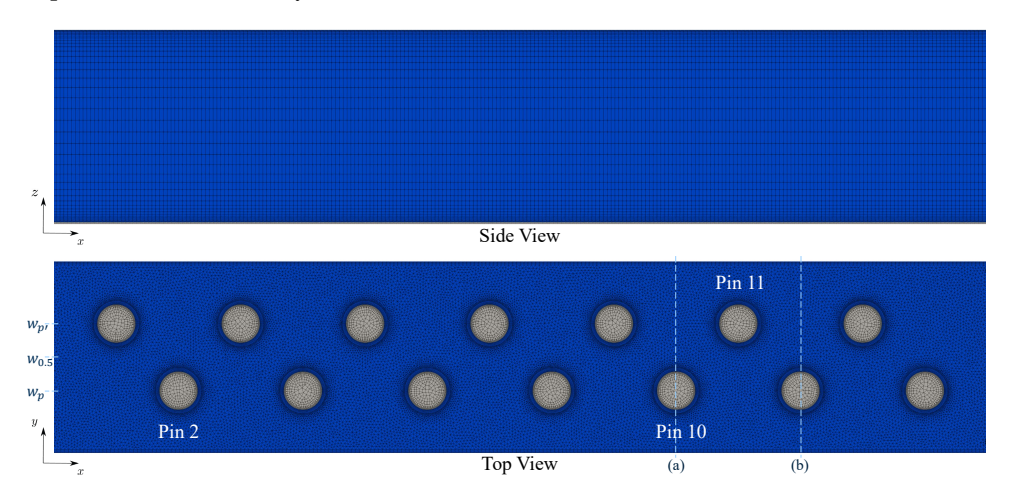


Figure 3.5: Discretized computational domain selected from the grid independence study. The side view illustrates the height-wise progression of the extruded 2D mesh shown in the top view. The labels correspond to the pin index as well as the locations at which slices and lines are used for data visualization.

3.3.4. OPTIMIZATION PROBLEM

The goal of the optimization study is to simultaneously increase the heat transfer coefficient and reduce the pumping losses. Thus, the optimization objective is expressed in terms of minimization of the temperature increase and the pressure drop across the heat sink. The optimization problem can then be formulated as

$$\min_{\alpha} \quad 0.8 \frac{\Delta T(\alpha)}{\Delta T_0} + 0.2 \frac{\Delta P(\alpha)}{\Delta P_0}, \quad (3.10)$$

subject to
$$\alpha_1 \le \alpha \le \alpha_{11}$$
, (3.11)

where α represents the design variables, ΔP and ΔT are calculated using Equation 3.9 and Equation 3.8 respectively, and the subscript 0 represents their values obtained with

the baseline geometry. The values of the weights in the objective function were selected according to Ref. [10]. This choice was validated through a preliminary parametric study, which revealed that to achieve a balanced improvement in both thermal and hydraulic performance, a higher weighting factor for ΔT is necessary.

The design variables (α) are the CAD parameters of the geometry of the fins that define the thickness distributions around the camber surface ($t^{\rm u}$, $t^{\rm l}$) and x-coordinates of the leading and trailing edges ($x_{\rm le}$, $x_{\rm te}$). Bounds are imposed on the design variables such that the variation of the design surface is within a radial distance of 1 to 3×10^{-3} m from the center of the cylindrical pins of the baseline geometry. Specifically, the bounds on $t^{\rm u}$, $t^{\rm l}$ are $\left[\frac{\rm d}{4},\frac{3\rm d}{4}\right]$, and those on $x_{\rm le}$, $x_{\rm te}$ are $\left[x_0-\frac{0.45\rm d}{2},x_0+\frac{0.45\rm d}{2}\right]$, where x_0 denotes their corresponding baseline values and d is the pin fin diameter (see Table 3.1) These bounds on the design variables reflect minimum wall thickness constraints and are also informed by the limitations of the mesh deformation algorithm in maintaining acceptable mesh quality. The verification of the gradient of the objective function with respect to the design variables is documented in Appendix 3.A. To obtain fins with identical shapes, the sensitivities of the design variables corresponding to different pins were averaged using the CP-AS approach documented in Chapter 2. Additionally, geometric symmetry of the fins was ensured by averaging the sensitivities corresponding to the design variables of the upper and lower thickness distributions, as also done in Chapter 2.

3.4. RESULTS

Figure 3.6 depicts the evolution of the objective function with the design iterations. The optimization leads to ~20% reduction in the value of the objective function in 37 design steps. This performance improvement is achieved by a simultaneous reduction in pressure drop and a reduction in the average temperature of the bottom part of the heat sink. In particular, the optimized geometry features an 18.8% lower pressure drop with a 3 K lower average temperature of the heated surface (corresponding to 20.5% lower ΔT defined by Equation 3.8). The optimization process reduced the optimality, defined as the degree of satisfaction of the first-order Karush-Kuhn-Tucker conditions computed by SNOPT, by 2 orders of magnitude and the L2 norm of the gradient by 78%. Each primal and adjoint evaluation required ~2 hours with 222 cores and 444 GB of memory on a high-performance computing platform equipped with *Intel Xeon E5-2680v4* having 2.8 GHz clockspeed.

The average heat transfer coefficient (\bar{h}) and Fanning friction factor (f) corresponding to the baseline and optimized geometries are reported in Table 3.4. The average heat transfer coefficients for the finned heat sinks are computed using

$$\bar{h} = \frac{q_b'' A_b}{(A_{ub} + \eta_{fin} A_{surft}) \Delta T},$$
(3.12)

where $A_{\rm b}$ is the area of the bottom heated surface, $A_{\rm ub}$ is the unfinned area of the base exposed to convection, $A_{\rm surf,t}$ is the total surface area of all the fins, and $\eta_{\rm fin}$ is the fin efficiency. To compute the fin efficiency for the two designs, additional simulations were performed with isothermal boundary conditions set on the bottom plate of the heat sink. The imposed temperature corresponds to the value of $T_{\rm in} + \Delta T_0$ (see Equation 3.8).

3.4. RESULTS 59

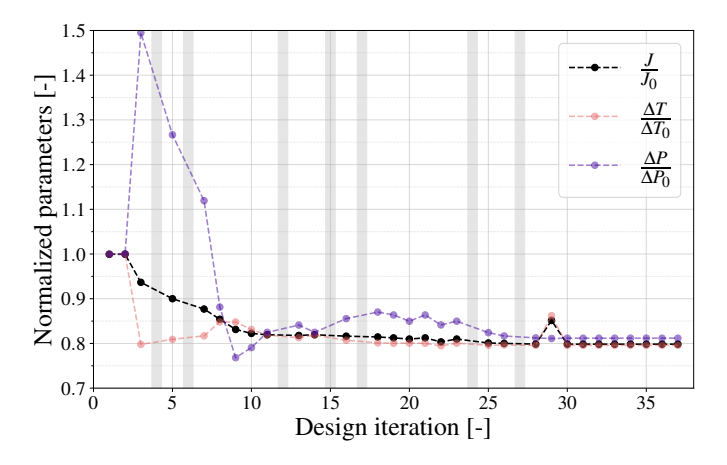


Figure 3.6: Evolution of the normalized objective function and performance parameters with design iterations. The design iterations that led to a divergence of the CHT solver due to poor mesh quality are indicated by in the optimization history.

Subsequently, the fin efficiency was computed as

$$\eta_{\rm fin} = \frac{q_{\rm fin,cht}}{q_{\rm fin\ max}},\tag{3.13}$$

where $q_{\mathrm{fin,cht}}$ is the heat transfer rate across the fins obtained from CHT simulations and $q_{\text{fin,max}}$ is the heat transfer rate with the fin surfaces at the same temperature as the bottom plate.

Table 3.4: Comparison of averaged heat transfer coefficient (\bar{h}) , Fanning friction factor (f) and fin efficiency (η_{fin}) estimated for the baseline and optimized geometries.

	Units	Baseline	Optimized
$ar{h}$	$W/(m^2 K)$	2133	2647
f	_	0.26	0.21
$\eta_{ m fin}$	_	0.37	0.44
$A_{\text{surf},t}$	m^2	0.00352	0.00347
$A_{ m ub}$	m^2	0.00182	0.00165

The Fanning friction factor can be computed using

$$f = \frac{\Delta P}{\frac{1}{2}\rho V_{\text{mean}}^2} \cdot \frac{D_{\text{h}}}{4L},\tag{3.14}$$

where $V_{\rm mean}$ is the mean velocity in the channel, $D_{\rm h}$ is the hydraulic diameter of the channel and L is the length of the heat sink. Table 3.4 shows a 24.1% increase in the heat transfer coefficient and an 18.8% decrease in friction factor, in analogy with the obtained reductions of ΔP and ΔT .

The analysis of the thermo-hydraulic performance of the heat sink designs is presented as follows. Firstly, the obtained 3D heat sink geometry, along with the temperature fields, is documented. Then, the shape of the optimized fin is compared to the baseline in terms of various geometric properties. Next, the performance achieved with the optimized heat sink geometry is analyzed and compared to that of the baseline design through heatmaps depicting the local heat transfer rates and heat transfer coefficients. The hydraulic performance is thereafter examined in terms of normalized pressure drop. The thermal-hydraulic analysis is first supported by 2D contours and then corroborated with line plots of the flow properties.

The 3D temperature fields in the solid domains of the baseline and optimized designs are presented in Figure 3.7. Additionally, Figure 3.7 depicts the velocity contours at representative horizontal ($z_{0.5}$) and vertical planes ($w_{p'}$) in the flow domain. It can be noted that the optimized design leads to a temperature decrease at the bottom solid plate, in particular in correspondence to the root of the fins. Moreover, it can be observed in Figure 3.7 that the optimized design features fins with a larger base but a slender profile in the central bulk-flow region (around $\frac{z}{H} = 0.5$).

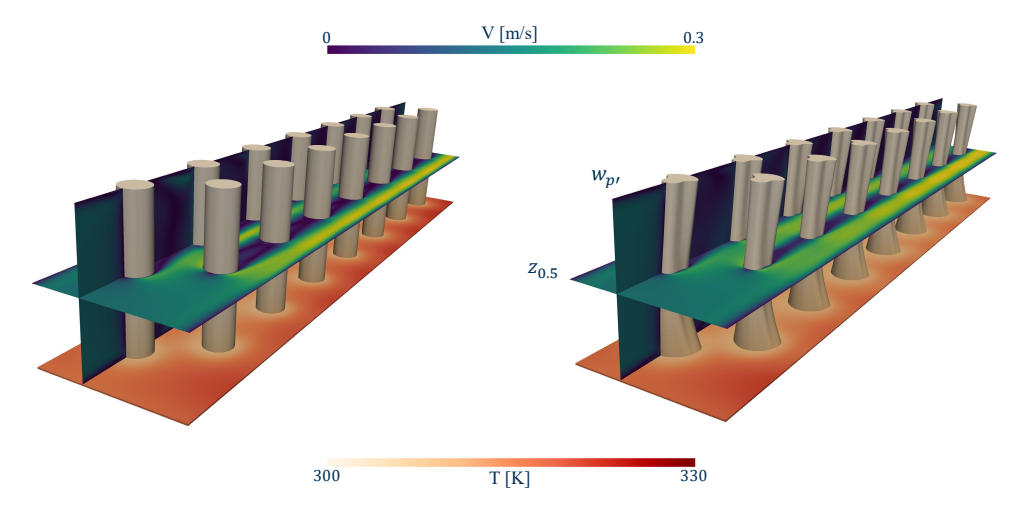


Figure 3.7: 3D temperature field contours in the solid domains of the baseline (left) and the optimized (right) designs, with 2D velocity contours at the planes $z_{0.5}$ and $w_{p'}$ in the fluid domains. The plane at $z_{0.5}$ is a horizontal cross-section at half the height of the fin, i.e. $\frac{Z}{H} = 0.5$, while the plane $w_{p'}$ is a vertical slice passing through the center of the odd-numbered pins (see Figure 3.5).

The shape of the baseline cylindrical fin and the optimized fin are compared in Figure 3.8. Additionally, Figure 3.8 depicts the variation of geometric properties, such as the cross-sectional area (a), perimeter (p), and projected frontal length ($l_{\rm fr}$), with the height of the fin/channel. The optimized fin geometry features a cross-sectional area at the bottom of the fin that is twice that of the baseline cylindrical geometry (see $\frac{a}{a_0}$ subplot in Figure 3.8). This increase in the base area results in more heat conduction through the fins given the applied uniform heat flux at the heat sink bottom plate. Moreover, the increased wetted surface of the pin in the bottom region (approximately 40% larger than in the baseline geometry) is beneficial for increasing convective heat transfer. Additionally,

the enlarged fin root warrants a higher fin efficiency. Furthermore, the optimized fin exhibits a reduced frontal area ($A_{\rm fr}$), resulting in less blockage to the flow. This reduction in blockage is most significant around the fin midspan (about z=0.4H), where $l_{\rm fr}$, the maximum width of the fin projected normal to the streamwise direction, is about 40% smaller than the baseline.

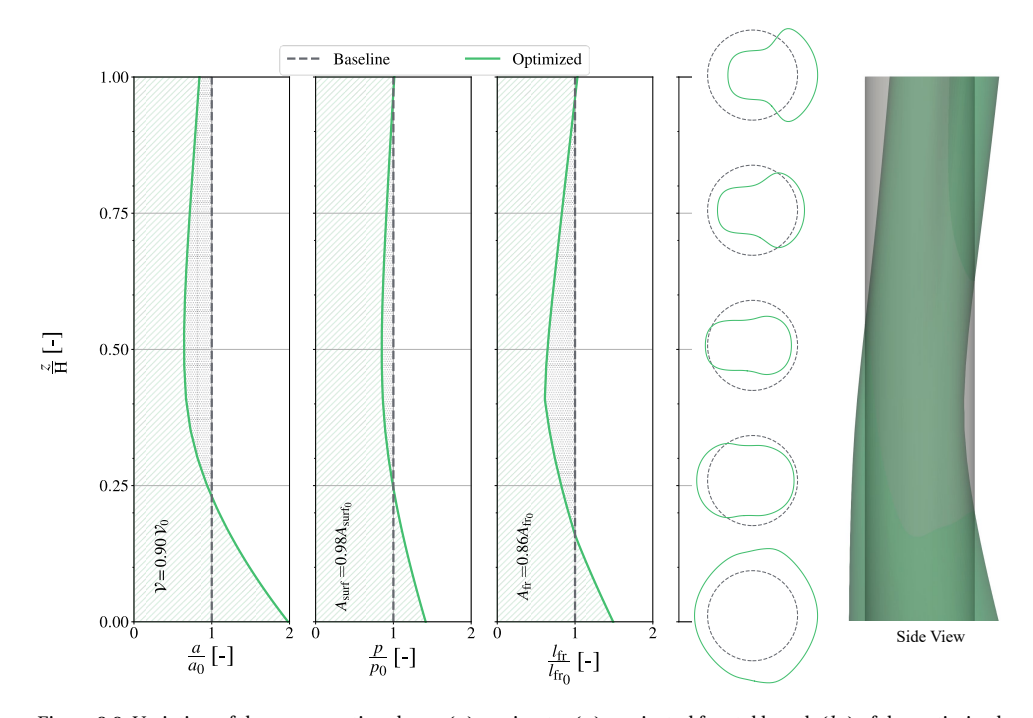


Figure 3.8: Variation of the cross-sectional area (a), perimeter (p), projected frontal length $(l_{\rm fr})$ of the optimized fin along the height, normalized by the baseline values (subscript 0). The integrals of these geometrical quantities over the height correspond to the fin volume (\mathcal{V}) , surface area $(A_{\rm surf})$, and frontal area $(A_{\rm fr})$, respectively. The side view of the baseline and optimized fin geometries is shown on the right.

The fin volume (V), surface area (A_{surf}), and frontal area (A_{fr}) for the optimized geometry are reduced by 10%, 2%, and 14%, respectively, compared to the original cylindrical fin.

Figure 3.9 presents the heat transfer rate distribution along the height of the fins through so-called heatmaps. The heatmaps are obtained by dividing the fins into four zones along the span and determining the heat transfer rate in each zone. The optimized geometry achieves a higher heat transfer rate than the baseline in all zones below fin midspan, i.e., below $z_{0.5}$. Conversely, for the region above $z_{0.75}$, the baseline geometry has a higher heat transfer rate, while for the zone between $z_{0.5}$ and $z_{0.75}$, the optimized geometry has a higher heat transfer rate only in the first four fins. The reason is that the bluff-body profile of the upper part of the optimized fins promotes a redistribution of the coolant flow (see Figure 3.12 at $w_{0.5}$) toward the heated plate (0.2 < $\frac{z}{H}$ < 0.5), at the expense of a reduction in heat transfer in the upper zones of the fins.

The variation of the local heat transfer coefficient along the fin height is displayed by means of heatmaps generated by averaging the local heat transfer coefficient across the

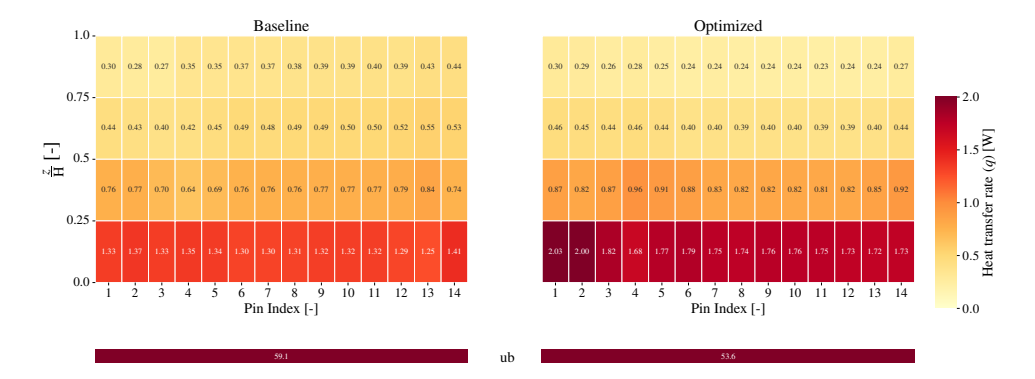


Figure 3.9: Comparison of heat transfer rate between the baseline and optimized designs. The heatmaps depict the heat transfer rate along the vertical axis of the fins for both design solutions. Four zones are considered along the fin height. Their extension is defined by the distance between the normalized heights $\frac{z}{H}$ of 0, 0.25, 0.5, 0.75, and 1. The heat transfer rate across the base plate ('ub') is also displayed.

four zones into which the fins are subdivided. The zone-wise heat transfer coefficient is computed by

$$\bar{h}_z = \frac{1}{A_{\text{surf},z}} \int_{A_{\text{surf},z}} \frac{q''}{T - T_{\text{in}}} \, \mathrm{d}A_{\text{surf}},\tag{3.15}$$

where q'', T are local heat flux and temperature values, and $A_{\text{surf},z}$ is the surface area corresponding to each zone. Note that the computation of the heat transfer coefficients is performed with the heat flux estimated by means of the simulations with isothermal solid surface used for the computation of $q_{\text{fin,max}}$ in Equation 3.13. This approach ensures the accuracy of the estimation of the heat transfer coefficient since the effect of fin efficiency is explicitly excluded from the computation. The optimum geometry features higher

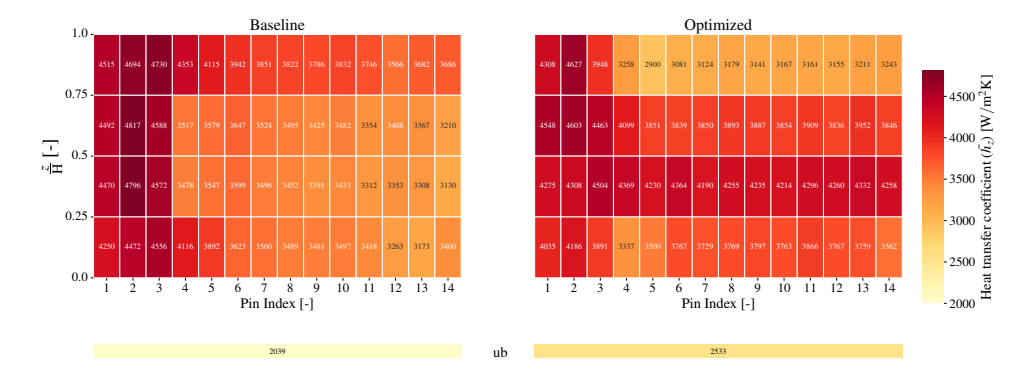


Figure 3.10: Comparison of heat transfer coefficients estimated for the baseline and optimized designs along each fin height. The extension of the four zones in which the fins are subdivided is defined by the distance between the normalized heights $\frac{z}{H}$ of 0, 0.25, 0.5, 0.75, and 1. The average heat transfer coefficient at the base plate ('ub') is also displayed.

heat transfer coefficient values than the baseline one in most of the zones below the fin

midspan, i.e., below $z_{0.5}$, except in correspondence to the initial pins. Additionally, the heat transfer coefficient at the unfinned base plate is higher than in the baseline design. Since the heat transfer coefficients are higher in the region near the heat source, the heat dissipation is enhanced with the optimized design.

The effect of enhanced heat dissipation is reflected in the temperature distributions presented in Figure 3.11. It can be seen from the temperature contours at the bottom heat sink surface (the plane indicated as z_b in the figure) that the optimized design results into a lower average temperature at the base along with a more uniform temperature distribution. The improved performance can be attributed to the following flow features observable in the velocity contours in Figure 3.11. Firstly, in correspondence to the central bulk-flow region (0.25 < $\frac{z}{H}$ < 0.75), the slender shape of the optimized fin allows the flow to remain attached over a larger extent of the fin profile than in the baseline design (see in Figure 3.11 the velocity field at $z_{0.5}$), ultimately enhancing the local heat transfer coefficient. Furthermore, the larger hub profile of the pin leads to more pronounced recirculation zones near the bottom heated region (illustrated by Figure 3.11 at $z_{0,1}$). The net effect is the enhancement in flow mixing (see Appendix 3.B), which in turn results in higher heat transfer rates in the bottom part of the pins and a higher heat transfer coefficient along the unfinned part of the base plate (see Figure 3.9 and Figure 3.10). The recirculation zones are also present near the top wall of the channel, as the fin features a bluff-body profile in the aft part. A key benefit of such unconventional pin geometry is the promotion of flow redistribution towards the higher temperature regions (see Figure 3.12 at $w_{0.5}$). Finally, the optimized fins are leaned in the z-direction (see the side view in Figure 3.8 and w_p in Figure 3.12). This leads to a decrease in the frontal area and the associated flow blockage for the same pin wetted area (see also Figure 3.8).

Hydraulic performance is investigated by computing viscous dissipation across each pin, expressed in terms of non-dimensionalized Euler number (Eu), and comparing it for the two designs in Figure 3.13. Eu corresponding to each pin i is computed by

$$Eu_i = \frac{\Delta P_{t,i}}{\frac{1}{2}\rho V_{\text{mean}}^2},\tag{3.16}$$

where $\Delta P_{t,i}$ is the total pressure drop across the i^{th} pin, ρ is the density of water and V_{mean} is the mean velocity in the channel. The total pressure drop (ΔP_{t}) across any pin, for example, Pin 11 (see Figure 3.5), is computed as

$$\Delta P_{\rm t,11} = P_{\rm (a)} + \frac{1}{2} \rho V_{\rm mean,(a)}^2 - P_{\rm (b)} - \frac{1}{2} \rho V_{\rm mean,(b)}^2, \tag{3.17}$$

which denotes the difference in average static and dynamic pressure between locations (a) and (b) defined by the cross-sectional planes at the centers of preceding and succeeding pins. Across all pins, the Eu number for the optimized design is consistently lower than that calculated for the baseline geometry, thus indicating lower viscous dissipation. The reduction in pressure drop achieved with the optimized design results from the lower blockage to the flow caused by the fins in the bulk-flow region (around $0.25 < \frac{z}{H} < 0.75$, see $\frac{l_{\rm fr}}{l_{\rm fr_0}}$ subplot in Figure 3.8). Furthermore, due to the slender profiles, the flow separation is delayed (see Figure 3.12 at $w_{0.5}$), leading to a smaller recirculation zone and, thus, lower mixing losses.

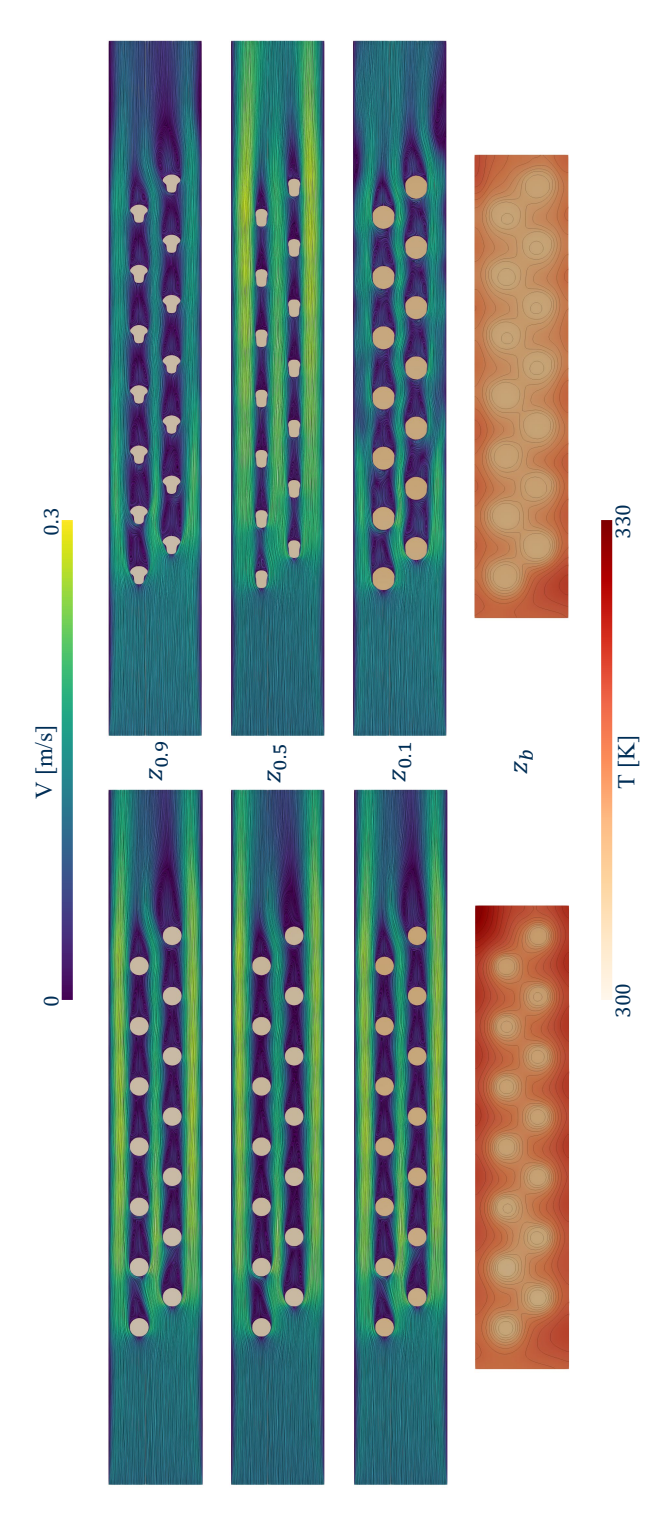
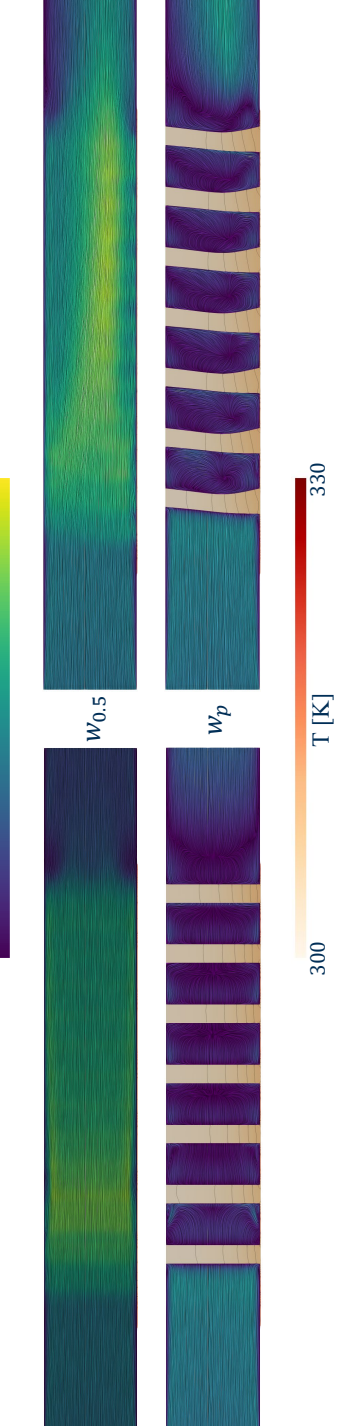


Figure 3.11: Comparison of the velocity contours in the fluid domain at selected spanwise cross-sections and the temperature contours in the solid domain at the bottom heated surface (z_b) for the baseline (left) and the optimized (right) designs. The horizontal slices in the fluid domain are taken at normalized heights $\frac{z}{H}$ of 0.9, 0.5, and 0.1.

65



0.3

Figure 3.12: Comparison of the velocity contours in the fluid domain and the temperature contours in the solid domain at selected vertical cross-sections for the baseline (left) and the optimized (right) designs. The vertical cross-sections are taken at half the channel width $(w_{0.5})$, as well as at a plane w_p passing through the center of the even-numbered pins (see Figure 3.5).

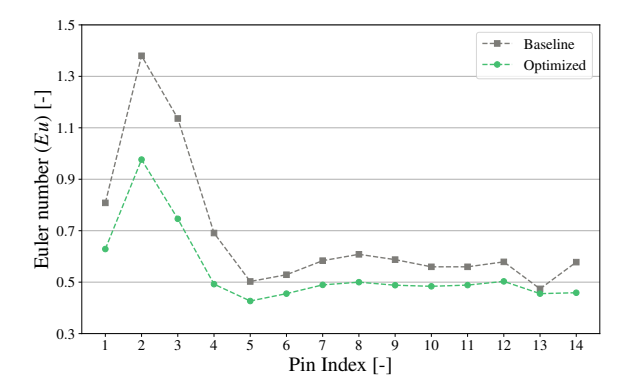


Figure 3.13: Comparison of Euler number between the baseline and optimized designs.

The trend in the Eu number and the improved thermal-hydraulic performance of the optimized design is further corroborated by means of line plots of flow properties along the heat sink. The variation of gauge pressure in the streamwise direction is illustrated in Figure 3.14. Apart from the inlet region where the entrance effects ($\sim \frac{x}{L} < 0.2$) are prominent, the pressure along the main flow direction features a steady decline, with the optimized design exhibiting a more gradual decrease as a consequence of the better aerodynamic profile of the fins.

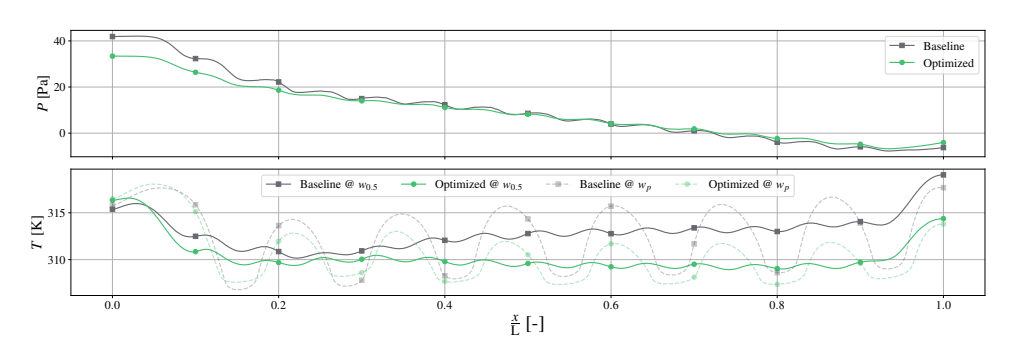


Figure 3.14: Pressure and temperature variation along the streamwise direction at specific locations in the fluid and solid domains, respectively. The top plot shows the pressure distribution along a line positioned at mid-height and mid-width of the fluid domain, while the bottom plot presents the temperature distribution at the bottom heated surface at half the width of the channel ($w_{0.5}$), and along a line w_p passing through the centers of even-numbered pins (see Figure 3.5).

The temperature variation along the length of the heat sink at the center of the bottom heated surface is shown in Figure 3.14. The optimized design features a more uniform temperature distribution on the heat sink base plate. In contrast, for the baseline design, the temperature rises monotonically along the streamwise direction. The analysis of the temperature variation on the bottom heated surface along an axis passing through the center of the pins (see Figure 3.5) reveals that the temperature has large fluctuations, whose period is equal to the longitudinal pin pitch. Notably, the local minima in the

temperature distribution correspond to the positions of the pins. Moreover, the fluctuations are more pronounced for the baseline design. In the first pin rows ($\sim \frac{x}{L} < 0.3$), the temperature at the base of the baseline pins is lower than in the case of the optimized design. This is due to the higher average heat transfer coefficient established in the initial part of the heat sink (see Figure 3.10), as a result of larger flow accelerations.

Figure 3.15 shows the variation of the temperature of the heated surface along the line (a) indicated in Figure 3.5, namely along the width of the channel in correspondence to fin 10. At this distance from the entrance, the flow is fully developed for both designs. The temperature of the base plate at location (a) varies in a range of 13 K for the baseline geometry while in an interval of about 7.5 K for the optimized geometry. The lower temperature variation is a consequence of the more uniform temperature distribution achieved with the optimized fin shape.

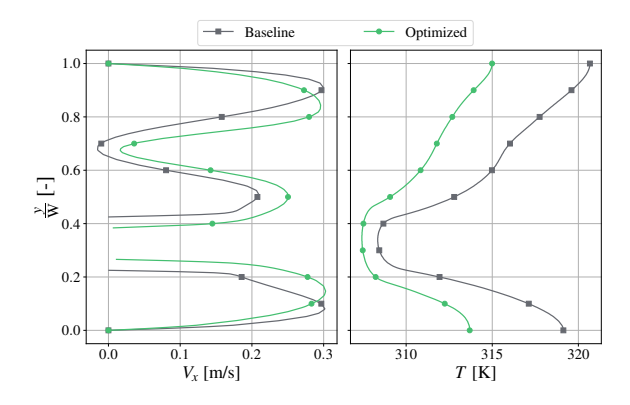


Figure 3.15: Velocity and temperature distributions at lines normal to the streamwise direction in the fluid and solid domains at the location of Pin 10 (see line (a) in Figure 3.5). The velocity distribution is sampled at $z_{0.5}$ while the temperature distribution corresponds to the bottom heated surface $z_{\rm b}$

The plots in Figure 3.15 also present the variation of the streamwise velocity component (V_x) along the channel width and at the fin midspan $(z_{0.5})$ in correspondence to the line (a) in Figure 3.5. The reduction in V_x observed around $\frac{y}{W} \sim 0.66$ is associated with the location of Pin 9 and its wake. In the case of the baseline design, the velocity becomes negative at $\frac{y}{W} \sim 0.66$. This indicates that the wake region of Pin 9, and, in general, of all the cylindrical fins, extends further in the streamwise direction than in the case of the optimized fins. Moreover, for the optimal design, the average velocity magnitude along the line (a) is higher. This is particularly noticeable near Pin 10, i.e. in the interval $0.2 < \frac{y}{W} < 0.5$. The reason for this difference in the velocity magnitude is twofold. First, the optimized fin features a smaller frontal area at midspan. Second, the coolant mass flow rate is higher at the center of the channel (see Figure 3.12 at $w_{0.5}$).

Finally, the temperature distributions along the vertical axis of Pin 2 and Pin 10 are presented in Figure 3.16. The plot shows that the temperature distribution in the fins differs only marginally from Pin 2 to Pin 10 for the optimized design, while for the baseline design, the average temperature of the pins increases significantly passing from Pin 2 to Pin 10.

Overall, the optimized fins allow for a lower and more uniform temperature in the heat

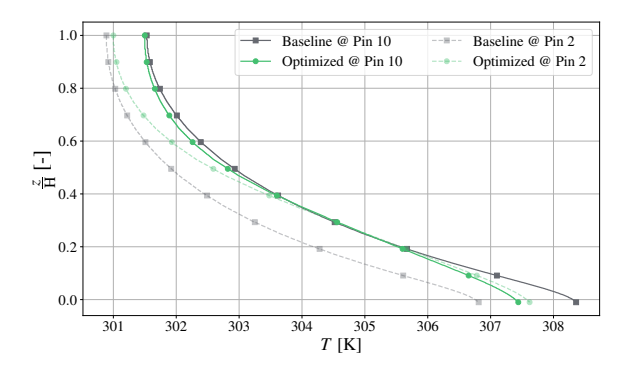


Figure 3.16: Temperature distributions along the vertical axis of Pin 10 and Pin 2 (see Figure 3.5).

sink base plate thanks to the higher heat transfer coefficients in the lower half of the fins. This results from a reduction of the fin wake in the bulk-flow region, larger recirculation zones, and then flow mixing near the bottom heated plate, as well as higher flow rates in the lower part of the heat sink. The reduction in pressure drop is due to reduced blockage and delayed separation in the bulk-flow region. In addition, a wider base of fins leads to increased fin efficiency. Furthermore, the solution of the optimization problem with the CP-LS formulation has the potential to obtain optimized fin geometries with distinct shapes (see Appendix 3.C) that could result in further performance improvements, especially for cases with non-uniform heat flux. To apply the method to such cases, careful consideration must be given to the mesh corresponding to the baseline geometry and the capabilities of the mesh deformation method, accounting for the bounds on the design variables. The findings of the study documented in this chapter demonstrate that significant improvement in the thermal-hydraulic performance of heat sinks can be achieved with reasonable computational cost using a method that combines adjoint-based shape optimization with CAD-based parametrization.

3.5. CONCLUSIONS

The research work documented in this paper focused on the development of a method to perform shape optimization for conjugate heat transfer problems using the adjoint method and CAD-based parameterization. The design framework, comprising the open-source CFD software SU2 [26] with adjoint capabilities and a CAD-based parametrization tool [27] was applied to optimize the shape of the fins of a water-cooled heat sink.

The main conclusions of the work can be summarized as follows.

- 1. The optimization resulted in an unconventional fin geometry, enabling an increase in the average heat transfer coefficient by 23.3% while reducing the pressure drop by 18.8%, compared to the original cylindrical fins.
- 2. The optimized fins feature a larger cross-section at the hub, leading to more heat conduction through the pins, and a slender profile in the 25% 75% range of the span, enhancing convective heat transfer and minimizing flow blockage.

3.5. CONCLUSIONS 69

3. The improvement in the thermo-hydraulic performance of the heat sink is achieved also through a redistribution of the flow towards the heated base plate.

4. Though the design method proved to be robust and enabled the attainment of unconventional fin shapes, further improvements can be envisaged if the current limitations of the adopted mesh deformation method to handle large grid displacements will be addressed.

This chapter demonstrates the capability of the method in generating innovative designs for fins. Future work will focus on incorporating a more sophisticated mesh deformation based on radial basis functions and applying the design framework to cases with non-uniform heat flux. In addition, the use of local sensitivities to optimize the individual fin shapes will be explored.

3

APPENDIX 3.A: GRADIENT VERIFICATION

The gradients obtained using the design chain with the adjoint (ADJ) method are verified by comparing their values with those obtained by the first-order forward finite difference (FD) method. The approach for gradient verification was similar to the one in Ref. [25] and included the considerations of the 3D parameterization and multi-zone domains. The gradient verification was performed for fewer design variables due to the high computational cost associated with the 3D CHT simulations. The randomly selected 50 design variables included the thickness parameters associated with pins interacting with the freestream flow as well as those in the wake. From a preliminary parametric study, two FD step sizes, 0.1% and 0.05%, were selected for the computation of gradients using FD. Figure 3.17 presents the comparison of the values of the gradient of the objective function computed using the two methods, with an FD step size value that resulted in a better quantitative agreement. Using this approach, the average deviation obtained for most variables was less than 5%. Using a more suitable step size for each design variable, the relative discrepancies can be reduced to below 0.5%. However, such a parametric study was constrained by the high computational cost of the 3D CHT simulations, which is further impeded by the slow convergence of the CHT solver. For the purpose of the optimization case study, the gradient verification presented in Figure 3.17 is considered sufficient.

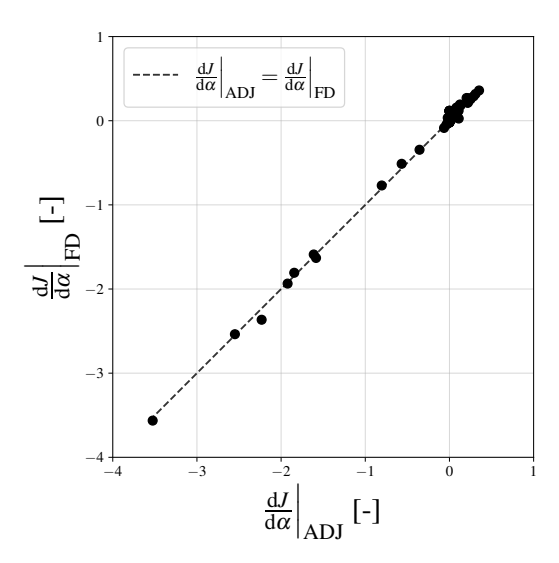


Figure 3.17: Gradient verification plot for design variables of the case study.

APPENDIX 3.B: QUANTIFICATION OF MIXING IN RECIRCULATION ZONES

The mixing in recirculation zones near the heated bottom plate in the optimized design is quantified in terms of standard deviation and coefficient of variance of temperature.

Lower values of these quantities indicate a more homogeneous temperature field in the fluid caused by improved mixing. The coefficient of variation of temperature in a control volume is given by:

$$COV_T = \frac{\sigma_T}{\bar{T}},\tag{3.18}$$

where \bar{T} is the volume-average temperature and σ_T is standard deviation computed by

$$\sigma_T = \sqrt{\frac{1}{V} \int_V (T - \bar{T})^2 \, dV}.$$
 (3.19)

To analyze the mixing associated with the recirculation zones near the heated bottom plate (depicted by the velocity contours in Figure 3.11 at $z_{0.1}$), control volumes are selected in the wake of Pin 2 and Pin 10. The control volumes, represented in Figure 3.18, span from the bottom heated surface (z_b) to $z_{0.1}$. The computed parameters corresponding to the baseline and optimized designs are reported in Table 3.5.

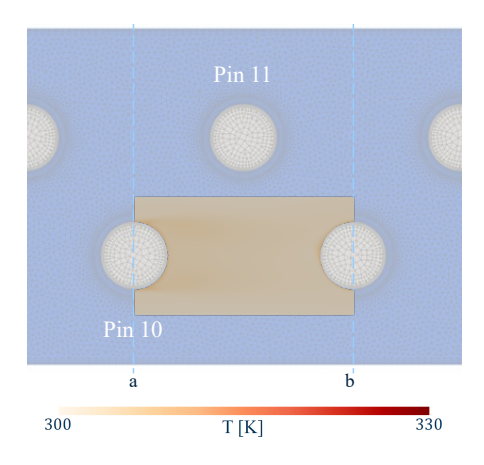


Figure 3.18: Representation of the control volume selected for quantification of mixing in the wake corresponding to Pin 10 (see Figure 3.5) along with its temperature distribution. The control volume spans from the bottom heated surface z_b to $z_{0.1}$.

Table 3.5: Comparison of volume-averaged temperature (\bar{T}) , standard deviation (σ_T) , and coefficient of variation (COV_T) in the wake regions behind the Pin 2 and Pin 10 for the baseline and optimized geometries.

	Baseline Pin 2 Pin 10		Optir	nized
Metric			Pin 2	Pin 10
$\bar{T}[K]$	302.39	303.12	302.10	302.11
$\sigma_T[K]$	8.59	8.58	2.38	2.05
COV_T	0.0284	0.0283	0.0079	0.0068

The optimized geometry leads to more than \sim 60% reduction in σ_T and COV_T values compared to those corresponding to the baseline. This is because the optimized design

promotes mixing and leads to more homogeneous fluid temperatures in the analyzed region.

APPENDIX 3.C: OPTIMIZATION WITH THE CP-LS FORMULATION

A variation of the optimization problem described in subsection 3.3.4 was investigated with the CP-LS formulation. This formulation, as described in subsection 2.2.6, utilizes local sensitivities whereby the resulting optimized fin geometries feature distinct, non-identical shapes. The observations and challenges associated with the progress of the optimization process are documented in the following.

The optimization history contained a large number of design iterations that led to the divergence of the CHT solver. Nearly every alternate design iteration led to divergence, resulting in a higher number of diverged design points than for the CP-AS formulation, i.e., the formulation that results in identical shapes of fin geometries. The key reason for the divergence of the CHT solver was the deteriorated mesh quality obtained with the mesh deformation algorithm based on the linear elasticity method. The limitations of the mesh deformation method were especially evident in the design steps with larger variations in the curvatures of individual fins as well as their proximity to those of the surrounding non-identical fins (see exemplary design in Figure 3.19). The design iterations with poor mesh quality that led to divergence of the CHT solver simulations were penalized as failed evaluations to be able to proceed with the optimization, similar to Figure 3.6. After 50 design iterations, the optimization process led to ~18.5% reduction in the value of the objective function. Thus, the performance improvements achieved are less than those achieved with CP-AS. It can be hypothesized that the mesh deformation algorithm and solver divergence affect the design exploration. To investigate this further, an additional optimization run was performed with the CP-LS formulation, albeit with the initial geometry corresponding to the optimal solution obtained from the CP-AS setup. The results achieved a marginal improvement of $\sim 1\%$. Therefore, it may be hypothesized that for the case study investigated in this chapter, the potential improvements with the CP-LS formulation are inherently limited.



Figure 3.19: Illustration of the heat sink design obtained with CP-LS formulation.

To enable a more conclusive assessment of the optimization with CP-LS formulation, future work will investigate improved mesh-deformation algorithms, including their application to configurations with non-uniform heat flux.

BIBLIOGRAPHY

- [1] B. J. Brelje and J. R. Martins, "Electric, hybrid, and turboelectric fixed-wing aircraft: A review of concepts, models, and design approaches", *Progress in Aerospace Sciences*, vol. 104, pp. 1–19, 2019, ISSN: 0376-0421. DOI: 10.1016/j.paerosci.2018.06.004.
- [2] M. Asli *et al.*, "Thermal management challenges in hybrid-electric propulsion aircraft", *Progress in Aerospace Sciences*, vol. 144, p. 100 967, 2024. DOI: 10.1016/j.paerosci.2023.100967.
- [3] M. Coutinho *et al.*, "A review on the recent developments in thermal management systems for hybrid-electric aircraft", *Applied Thermal Engineering*, vol. 227, p. 120427, 2023. DOI: 10.1016/j.applthermaleng.2023.120427.
- [4] H. E. Ahmed, B. Salman, A. S. Kherbeet, and M. Ahmed, "Optimization of thermal design of heat sinks: A review", *International Journal of Heat and Mass Transfer*, vol. 118, pp. 129–153, 2018. DOI: 10.1016/j.ijheatmasstransfer.2017.10.099.
- [5] M. M. A. Bhutta, N. Hayat, M. H. Bashir, A. R. Khan, K. N. Ahmad, and S. Khan, "CFD applications in various heat exchangers design: A review", *Applied Thermal Engineering*, vol. 32, pp. 1–12, 2012. DOI: 10.1016/j.applthermaleng.2011.09.001.
- [6] Y. Wang, L.-C. Wang, Z.-M. Lin, Y.-H. Yao, and L.-B. Wang, "The condition requiring conjugate numerical method in study of heat transfer characteristics of tube bank fin heat exchanger", *International journal of heat and mass transfer*, vol. 55, no. 9-10, pp. 2353–2364, 2012. DOI: 10.1016/j.ijheatmasstransfer.2012.01.029.
- [7] M. Ahmadian-Elmi, A. Mashayekhi, S. Nourazar, and K. Vafai, "A comprehensive study on parametric optimization of the pin-fin heat sink to improve its thermal and hydraulic characteristics", *International Journal of Heat and Mass Transfer*, vol. 180, p. 121 797, 2021. DOI: 10.1016/j.ijheatmasstransfer.2021.121797.
- [8] M. Kim, M. Y. Ha, and J. K. Min, "A numerical study on various pin–fin shaped surface air–oil heat exchangers for an aero gas-turbine engine", *International Journal of Heat and Mass Transfer*, vol. 93, pp. 637–652, 2016. DOI: 10.1016/j.ijheatmas stransfer.2015.10.035.
- [9] K. Hu, C. Lu, B. Yu, L. Yang, and Y. Rao, "Optimization of bionic heat sinks with self-organized structures inspired by termite nest morphologies", *International Journal of Heat and Mass Transfer*, vol. 202, p. 123735, 2023, ISSN: 00179310. DOI: 10.1016/j.ijheatmasstransfer.2022.123735.

74

- [10] N. P. Nguyen, E. Maghsoudi, S. N. Roberts, and B. Kwon, "Shape optimization of pin fin array in a cooling channel using genetic algorithm and machine learning", *International Journal of Heat and Mass Transfer*, vol. 202, p. 123769, 2023. DOI: 10.1016/j.ijheatmasstransfer.2022.123769.
- [11] C. Yu, X. Zhu, Z. Li, Y. Ma, M. Yang, and H. Zhang, "Optimization of elliptical pin-fin microchannel heat sink based on artificial neural network", *International Journal of Heat and Mass Transfer*, vol. 205, p. 123 928, 2023. DOI: 10.1016/j.ijheatmasstransfer.2023.123928.
- [12] M. E. Polat and S. Cadirci, "Artificial neural network model and multi-objective optimization of microchannel heat sinks with diamond-shaped pin fins", *International Journal of Heat and Mass Transfer*, vol. 194, p. 123 015, 2022, ISSN: 00179310. DOI: 10.1016/j.ijheatmasstransfer.2022.123015.
- [13] J. Nocedal and S. J. Wright, *Numerical Optimization* (Springer Series in Operations Research and Financial Engineering), 2nd ed. New York: Springer, 2006, ISBN: 9780387303031. DOI: 10.1007/978-0-387-40065-5.
- [14] K. Gkaragkounis, E. Papoutsis-Kiachagias, and K. Giannakoglou, "The continuous adjoint method for shape optimization in conjugate heat transfer problems with turbulent incompressible flows", *Applied Thermal Engineering*, vol. 140, pp. 351–362, 2018.
- [15] K. T. Gkaragkounis, E. M. Papoutsis-Kiachagias, and K. C. Giannakoglou, "Adjoint-assisted Pareto front tracing in aerodynamic and conjugate heat transfer shape optimization", *Computers & Fluids*, vol. 214, p. 104753, 2021, ISSN: 0045-7930. DOI: 10.1016/j.compfluid.2020.104753.
- [16] J. L. Anibal, C. A. Mader, and J. R. Martins, "Aerodynamic shape optimization of an electric aircraft motor surface heat exchanger with conjugate heat transfer constraint", *International Journal of Heat and Mass Transfer*, vol. 189, p. 122 689, 2022, ISSN: 0017-9310. DOI: 10.1016/j.ijheatmasstransfer.2022.122689.
- [17] O. Burghardt, P. Gomes, T. Kattmann, T. D. Economon, N. R. Gauger, and R. Palacios, "Discrete adjoint methodology for general multiphysics problems: A modular and efficient algorithmic outline with implementation in an open-source simulation software", *Structural and Multidisciplinary Optimization*, vol. 65, no. 1, p. 28, 2022. DOI: 10.1007/s00158-021-03117-5.
- [18] P. He, C. Psenica, L. Fang, and M. Leader, "Aerothermal shape optimization of actively-cooled battery packs using conjugate heat transfer", in *AIAA SCITECH 2025 Forum*, American Institute of Aeronautics and Astronautics, Jan. 2025. DOI: 10.2514/6.2025-1559.
- [19] S. Vitale, M. Pini, and P. Colonna, "Multistage turbomachinery design using the discrete adjoint method within the open-source software SU2", *Journal of Propulsion and Power*, vol. 36, no. 3, pp. 465–478, 2020, ISSN: 1533-3876. DOI: 10.2514/1.B37 685.

BIBLIOGRAPHY 75

[20] L. Mueller and T. Verstraete, "CAD integrated multipoint adjoint-based optimization of a turbocharger radial turbine", *International Journal of Turbomachinery*, *Propulsion and Power*, vol. 2, no. 3, 2017, ISSN: 2504186X. DOI: 10.3390/ijtpp2030014.

- [21] N. Anand, S. Vitale, M. Pini, and P. Colonna, "Assessment of FFD and CAD-based shape parametrization methods for adjoint-based turbomachinery shape optimization.", in *Proceedings of Global Power and Propulsion Society, Montreal, Canada*, 2018, pp. 1–8. DOI: 10.5281/zenodo.1344595.
- [22] S. Xu, D. Radford, M. Meyer, and J.-D. Müller, "CAD-Based Adjoint Shape Optimisation of a One-Stage Turbine With Geometric Constraints", in *Proceedings of Turbo Expo: Power for Land, Sea, and Air*, vol. Volume 2C: Turbomachinery, Jun. 2015, V02CT45A006. DOI: 10.1115/GT2015-42237.
- [23] M. Chávez-Modena, L. M. González, and E. Valero, "Numerical optimization of the fin shape experiments of a heat conjugate problem surface air/oil heat exchanger (SACOC)", *International Journal of Heat and Mass Transfer*, vol. 182, p. 121 971, 2022. DOI: 10.1016/j.ijheatmasstransfer.2021.121971.
- [24] O. R. Imam-Lawal, "Adjoint based optimisation for coupled conjugate heat transfer.", Ph.D. dissertation, Queen Mary University of London, 2020.
- [25] P. Pai Raikar, N. Anand, M. Pini, and C. De Servi, "Concurrent optimization of multiple heat transfer surfaces using adjoint-based optimization with a CADbased parametrization", *International Journal of Heat and Mass Transfer*, vol. 236, p. 126 230, 2025, ISSN: 0017-9310. DOI: 10.1016/j.ijheatmasstransfer.2024 .126230.
- [26] T. D. Economon, F. Palacios, S. R. Copeland, T. W. Lukaczyk, and J. J. Alonso, "SU2: An open-source suite for multiphysics simulation and design", *AIAA Journal*, vol. 54, no. 3, pp. 828–846, 2016. DOI: 10.2514/1.J053813.
- [27] R. Agromayor, N. Anand, J. D. Muller, M. Pini, and L. O. Nord, "A unified geometry parametrization method for turbomachinery blades.", *Computer Aided Design*, vol. 133, no. 102987, pp. 1–16, 2021. DOI: 10.1016/j.cad.2020.102987.
- [28] Various Authors, Parablade, version v1.0, 2020. DOI: 10.5281/zenodo.3894778.
- [29] A. B. Lambe and J. R. R. A. Martins, "Extensions to the Design Structure Matrix for the Description of Multidisciplinary Design, Analysis, and Optimization Processes", *Structural and Multidisciplinary Optimization*, vol. 46, pp. 273–284, 2012. DOI: 10.1007/s00158-012-0763-y.
- [30] P. E. Gill, W. Murray, and M. A. Saunders, "SNOPT: An SQP algorithm for large-scale constrained optimization", *SIAM Review*, vol. 47, no. 1, pp. 99–131, 2005. DOI: 10.1137/S0036144504446096.
- [31] N. Wu, G. Kenway, C. A. Mader, J. Jasa, and J. R. R. A. Martins, "pyOptSparse: A Python framework for large-scale constrained nonlinear optimization of sparse systems", *Journal of Open Source Software*, vol. 5, no. 54, p. 2564, 2020. DOI: 10.211 05/joss.02564.

76 BIBLIOGRAPHY

[32] R. Dwight, "Robust mesh deformation using the linear elasticity equations", in *Computational Fluid Dynamics* 2006, Jan. 2009, pp. 401–406, ISBN: 978-3-540-92778-5. DOI: 10.1007/978-3-540-92779-2 62.

- [33] L. Piegl and W. Tiller, *The NURBS book*, 2nd. Springer Science & Business Media, 2012. DOI: 10.1007/978-3-642-59223-2.
- [34] T. Kattmann, "Efficient adjoint-based design capability for unsteady conjugate heat transfer problems", Ph.D. dissertation, Rheinland-Pfälzische Technische Universität Kaiserslautern-Landau, 2025, pp. XIV, 131. DOI: 10.26204/KLUED0/9056.
- [35] T. D. Economon, "Simulation and adjoint-based design for variable density incompressible flows with heat transfer", *AIAA Journal*, vol. 58, no. 2, pp. 757–769, 2020, ISSN: 00011452. DOI: 10.2514/1.J058222.
- [36] M. Sagebaum, T. Albring, and N. R. Gauger, "High-Performance Derivative Computations using CoDiPack", *ACM Trans. Math. Softw.*, vol. 45, no. 4, 2019, ISSN: 0098-3500. DOI: 10.1145/3356900.
- [37] R. Sanchez, T. Albring, R. Palacios, N. R. Gauger, T. D. Economon, and J. J. Alonso, "Coupled adjoint-based sensitivities in large-displacement fluid-structure interaction using algorithmic differentiation", *International Journal for Numerical Methods in Engineering*, vol. 113, no. 7, pp. 1081–1107, 2017. DOI: 10.1002/nme.5700.
- [38] O. Burghardt, N. R. Gauger, and T. D. Economon, "Coupled adjoints for conjugate heat transfer in variable density incompressible flows", *AIAA*, no. 2019-2668, 2019.
- [39] P. He, C. A. Mader, J. R. Martins, and K. J. Maki, "Aerothermal optimization of a ribbed u-bend cooling channel using the adjoint method", *International Journal of Heat and Mass Transfer*, vol. 140, pp. 152–172, 2019. DOI: 10.1016/j.ijheatmass transfer. 2019.05.075.
- [40] I. Pointwise, *Pointwise*, https://www.pointwise.com, version 18.5 R2, [Computer software], 2022.
- [41] N. P. Nguyen, E. Maghsoudi, S. N. Roberts, D. C. Hofmann, and B. Kwon, "Understanding heat transfer and flow characteristics of additively manufactured pin fin arrays through laser-induced fluorescence and particle image velocimetry", *International Journal of Heat and Mass Transfer*, vol. 222, p. 125 198, 2024. DOI: 10.1016/j.ijheatmasstransfer.2024.125198.

4

TOWARDS CFD-BASED OPTIMIZATION IN SYSTEM DESIGN

Parts of this chapter to appear in:

P. Pai Raikar, F. Beltrame, N. Anand, M. Pini, and C. De Servi, *Application of adjoint-based shape optimization to the design of heat exchangers for airborne ORC waste heat recovery system,* Proceedings of ASME Turbo Expo 2026: Turbomachinery Technical Conference & Exposition (in preparation).

Abstract

The use of an integrated design methodology in which both system-level process variables and the design variables defining HEX geometry are optimized synergistically has the potential to yield significant improvements in the performance of energy conversion systems. This chapter presents the initial steps toward the development of a design chain combining the adjoint-based shape optimization method documented in Chapter 2 with a procedure for optimal system design, wherein component preliminary sizing and process characteristics are optimized simultaneously using a multi-objective genetic algorithm. This optimization framework is applied to the design of an ORC unit that recovers thermal energy from the exhaust gases of an aircraft APU. Due to the computational burden of the overall design methodology, shape optimization is performed only for the most promising solution from the Pareto set obtained in the system-level preliminary design. Moreover, given the exploratory nature of the study, this CFD-based design method is applied only to refine the condenser geometry of the ORC unit, which consists of a circular tube bundle. The results show that the shape optimization method identifies a non-conventional tube profile for the condenser geometry that enables a 24% reduction in the cooling air pressure drop. This improvement yields a 3.5% increase in system power output compared to the original solution obtained during system-level design.

4.1. Introduction

The performance of an energy conversion system is determined by the efficiency of its thermodynamic processes and the effectiveness of its components. This dependency is heightened in aerospace applications, as fuel consumption during aircraft mission is influenced by more than just energy conversion efficiency. Key factors also include system weight, induced drag, and size, all of which are closely tied to component-level design choices. In the case of recuperated engines or thermal management systems aboard the aircraft, heat exchangers are the most critical components [1].

Traditional design approaches typically address the definition of the thermodynamic process and the sizing of the main system components in a sequential manner. However, this stepwise procedure often leads to multiple design iterations and may result in suboptimal solutions, particularly in aerospace applications. The alternative to such a consolidated design practice consists of adopting an integrated design methodology, wherein both system-level and component-level parameters are treated as design variables within a unified optimization framework. This approach has been shown to yield significant performance improvements, as demonstrated in Ref. [2], in which the authors document the development of an integrated design method for an aircraft environmental control system. The optimization variables included both the parameters defining the characteristics of the thermodynamic cycle, specifically an inverse Brayton cycle, and those specifying the geometry of the heat exchangers of the system.

The integration of HEX preliminary sizing procedures into system-level design optimization frameworks has been explored also in more recent studies. For example, an integrated design approach is reported in Ref. [3] for a recuperated Brayton cycle system coupled with a nuclear reactor for stationary power generation. Such a design approach enabled a better design solution, achieving a 54% increase in system power output despite a 7% reduction in the effectiveness of the main heat exchanger compared to the baseline

4.1. Introduction 79

design. A similar integrated design approach was adopted by Beltrame et al. [4] to investigate the technical feasibility of an organic Rankine cycle (ORC) for waste heat recovery from the exhaust gases of a turboshaft engine. Given the space limitations and the need to minimize the pressure drop in the exhaust gases and the cooling air, the performance and weight of the ORC system are essentially driven by the design of the condenser and the heat exchanger used to recover thermal energy. Compared to a sequential design strategy, the integrated approach yields solutions with approximately 10% lower system mass for a given power output of the combined turboshaft-ORC engine. In another recent work, Ascione et al. [5] presented an integrated design method for a vapor compression cycle system for air conditioning aboard aircraft. The main innovative feature of the proposed technology is the use of a high-speed, low-power capacity centrifugal compressor. Due to the strong coupling between the thermodynamic cycle characteristics, the size of the HEXs, the induced drag, and the feasibility of the compressor design, a simultaneous optimization of both the cycle configuration and the parameters defining the geometry of the components was essential to achieving viable and efficient system designs.

In all the studies mentioned above, the models used for preliminary HEX design typically rely on empirical correlations to estimate heat transfer coefficients and pressure drops. As a consequence, the applicability of these models is limited to the specific geometries and operating conditions for which the empirical correlations were developed. CFD-based models offer, in principle, a solution to such limitations by providing more physics-based predictions for any arbitrary geometry. However, their application in system-level simulations remains limited, primarily to the calibration of lumped parameter models that can be efficiently integrated into system models. For example, in the context of propulsion systems, El-Soueidan et al. [6] developed a lumped parameter model for the preliminary design of the HEXs of the Water-Enhanced Turbofan (WET) engine concept. The HEX model was calibrated with CFD results for the operating condition corresponding to the design point of the engine. At present, only a few studies have explored the synergistic use of CFD models in combination with system-level simulations. The most relevant is the work of Misirlis et al. [7] on characterizing the thermo-hydraulic performance of novel HEX concepts through CFD simulations and to assess their potential for intercooled recuperated (IR) engines. To make the computational cost of the simulations feasible, the HEXs were modeled using the so-called porous media approach [8]. The results of the CFD analysis were then employed to calibrate the HEX models of the thermodynamic cycle calculation routine of the IR engine, thereby supporting the identification of the best design option. Recently, Adler et al. [9] applied CFD-based methods to design a ducted radiator for aircraft thermal management using a gradient-based method to concurrently optimize the shape of the duct along with HEX design and sizing. HEX thermal-hydraulic performance was estimated using empirical correlations, and this lumped-parameter model was bidirectionally coupled with the RANS-based CFD model of the flow in and around the duct. However, the application of CFD-based shape optimization methods in connection with system-level optimal design remains unexplored.

The objective of the work documented in this chapter is to assess the feasibility of integrating an adjoint-based shape optimization method for the design of heat transfer surfaces into the design procedure of an energy conversion system for which HEXs

are critical components. To achieve this objective, an optimization framework is proposed that couples a system-level design method, whose degrees of freedom include the main HEX geometry characteristics, with the shape optimization method proposed in Chapter 2. Considering the cost of function evaluations and the number of design variables, a gradient-free optimization algorithm is adopted for the system design, whereas the CFD-based shape optimization relies on a gradient-based method. The proposed methodology is applied to the design of an ORC system for waste heat recovery from the auxiliary power unit of an aircraft. In the current implementation of the design framework, shape optimization is performed only for the ORC condenser after the preliminary design of the waste heat recovery system has been optimized. No iterative coupling is established between the system and the shape optimization design stages. The following sections present the results for the case study, followed by an analysis of the performance improvement obtained by shape optimization at both the component and system levels.

4.2. METHODOLOGY

Figure 4.1 illustrates the conceived optimization framework for system design, which integrates system-level simulations with CFD-based shape optimization of heat exchangers. The system design variables ($\alpha_{\rm sys}$) comprise the parameters defining the thermodynamic cycle characteristics as well as those used in the preliminary sizing of HEXs. The system model determines the values of the objective functions of interest based on the predictions of a thermodynamic cycle analysis routine, and the pressure drops and size of the HEXs obtained by solving the preliminary design procedure for each of these components. In this design stage, the HEX models are based on a one-dimensional discretization of the flow path of both the hot and cold streams, and rely on empirical correlations to estimate heat transfer coefficients and friction factors. The outcome of the system-level optimization is a set of optimal solutions forming a Pareto front with respect to the considered objective functions ($J_{\rm sys}^*$).

Given the computational burden of shape optimization, this method can be applied to the design of the HEXs of only the most promising solutions on the Pareto front. This selection is performed using the epsilon-constraint method [10, Ch. 9]. Next, the geometric characteristics of the HEXs corresponding to the selected system design points are used to define the computational domain and boundary conditions of the CFD model in SU2 [11, 12]. The heat transfer surfaces are parametrized as NURBS curves controlled by a set of design variables (α_{cfd_i}) by means of the tool Parablade, as described in Chapter 2. The values of the shape optimization objective function and constraint ($J_{\mathrm{cfd}_i}^*$, $c_{\mathrm{cfd}_i}^*$) are then used to estimate the performance of the whole heat transfer device (f_{hex}^*). Finally, this information is fed, if necessary, into the thermodynamic cycle analysis routine to estimate the overall performance of the system (J_{sys}^*).

4.3. CASE STUDY

The proposed methodology combining CFD-based optimization of HEXs with system design is tested with the case study of an ORC system designed as the bottoming unit of the auxiliary power unit (APU) of an Airbus A320 aircraft. Although the APU is in operation only when the aircraft is on-ground, its integration with a waste heat recovery

4.3. CASE STUDY 81

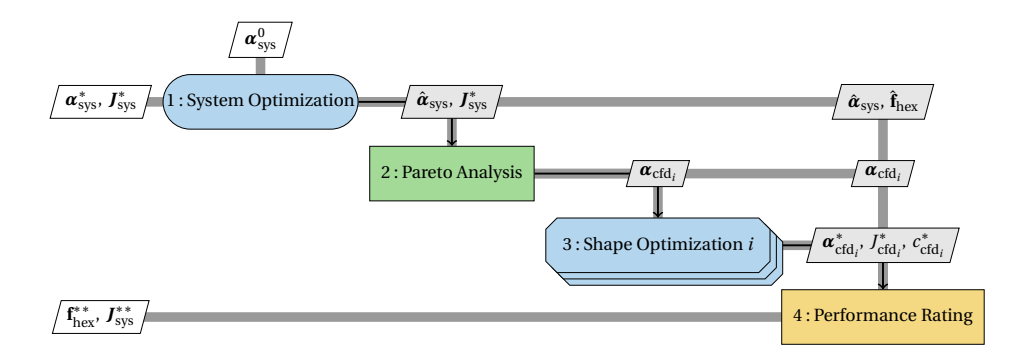


Figure 4.1: XDSM diagram [13] depicting the optimization framework for system design based on component shape optimization.

unit can yield sufficient fuel savings due to the typical low efficiency of APUs. This test case also serves as a preliminary step towards applying the methodology to more complex combined-cycle engine concepts, which may enable more consistent emission savings. The design specifications for the combined ORC-APU system are based on the work of Beltrame et al. [4], and its process flow diagram is illustrated in Figure 4.2. A supercritical configuration is selected for the ORC system, with cyclopentane as the working fluid. This bottoming unit is designed for a specified operating condition corresponding to the nominal power output of the APU, namely 250 kW. The exhaust gases exiting the gas turbine are assumed to have uniform velocity and temperature. In particular, the flow is characterized by a mass flow rate of 0.8 kg/s, a temperature of 847.15 K, and a pressure of 1.04 bar. These conditions are treated as fixed model inputs and remain constant throughout the ORC system design process. Furthermore, only the geometry of the condenser is optimized in this study, while that of the evaporator has been defined according to the results reported in Ref. [4]. Accordingly, CFD-based shape optimization is employed solely for the design of the condenser. The numerical models used for systemlevel simulations and CFD-based optimization of the condenser heat transfer surface are described in the following sections.

4.3.1. NUMERICAL MODELS FOR SYSTEM DESIGN

ORC SYSTEM MODEL

The thermodynamic cycle calculations for the evaluation of the ORC unit performance are performed using an in-house tool named *pycle*. The thermodynamic properties of the ORC working fluid, i.e., cyclopentane, are modeled using the Helmholtz-energy explicit equation of state (HEOS) implemented in CoolProp [14], while the ideal gas model is adopted for the APU exhaust gases. The evaporator has the same configuration as in Ref. [4]: it consists of a multi-pass staggered bare-tube bundle operating in a countercrossflow configuration. The geometry of the evaporator is fixed, with a tube outer diameter (d_0) of 1.8 mm, and longitudinal ($x_1 = s_1/d_0$) and transverse ($x_t = s_t/d_0$) pitch ratios of 3 and 1.25, respectively. Additionally, the frontal area is set to 0.28 x 0.28 m², in accordance with the size of the APU exhaust duct. The condenser consists of a single-

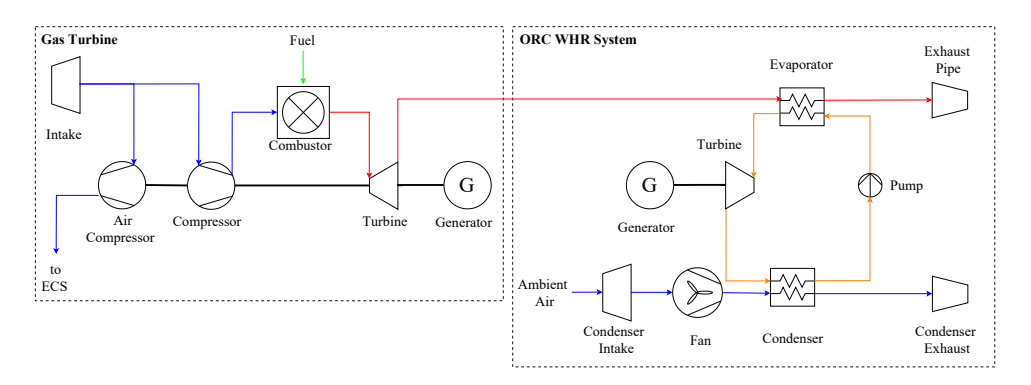


Figure 4.2: Process flow diagram of the CC-APU system, adapted from Ref. [4].

pass bare-tube bundle that operates with a crossflow arrangement. The tube bundle may feature either a staggered or an inline layout. Its geometry is determined using a dedicated HEX sizing model, as described in the following subsection. The considered condenser configurations, along with their geometric parameters, are illustrated in Figure 4.3.

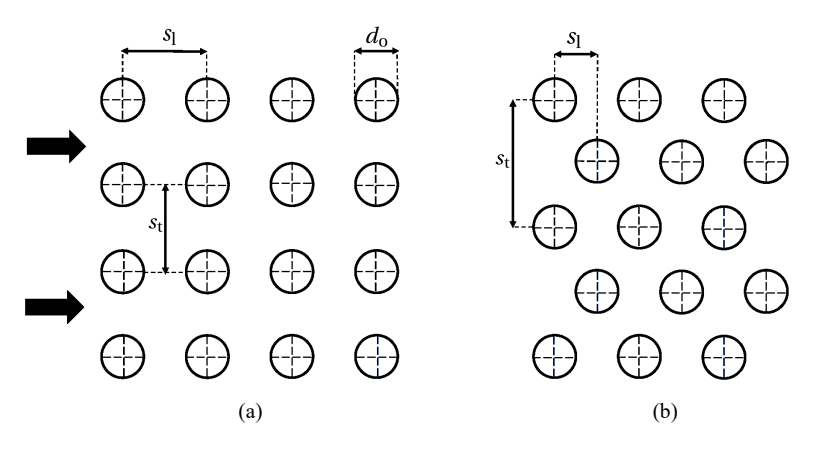


Figure 4.3: Illustration of the condenser tube layout in the case of an a)inline and b)staggered configuration.

The net power output of the ORC-WHR unit ($\dot{W}_{\rm net}$) is computed as

$$\dot{W}_{\rm net} = \dot{W}_{\rm turb} - \frac{\dot{m}_{\rm air} \Delta P_{\rm air}}{\rho_{\rm air} \eta_{\rm is,f} \eta_{\rm m,f}} - \frac{\dot{m}_{\rm wf} \Delta H_{\rm p}}{\eta_{\rm is,p} \eta_{\rm m,p}}$$
(4.1)

where $\dot{W}_{\rm turb}$ is the turbine power, from which the power consumption of the fan, used to supply the necessary air mass flow rate $(\dot{m}_{\rm air})$ to the condenser, and of the centrifugal pump driving the working fluid $(\dot{m}_{\rm wf})$ are subtracted. The turbine power $\dot{W}_{\rm turb}$ is computed assuming the same values of isentropic, mechanical, and generator efficiencies adopted in Ref. [4]. These efficiency values are reported in Table 4.1 along with those associated with the fan and the pump.

4.3. CASE STUDY 83

Table 4.1: Efficiencies of the components of the WHR unit. Subscripts denote: t = turbine, f = fan, p = pump, g = generator, is = isentropic, m = mechanical.

$\eta_{\mathrm{is,t}}$ 0.94	$\eta_{ m is,f}$ 0.60	$\eta_{\rm is,p}$ 0.65	$\eta_{ m g}$ 0.97
$\eta_{\mathrm{m,t}}$ 0.99	$\eta_{ m m,f}$ 0.98	$\eta_{\mathrm{m,p}}$ 0.98	

The mass of the ORC system ($M_{\rm ORC}$) is calculated as the sum of different contributions: the masses of the main ORC system components, namely the turbogenerator, fan, pump, evaporator, and condenser, along with the mass of the working fluid and the balance-of-plant. The mass of the turbogenerator is estimated assuming a specific power of 5.5 kW/kg for this component [15], while that of the centrifugal pump is determined based on a specific power of 4 kW/kg [16]. The combined mass of the fan and the balance-of-plant is assumed to account for 10% of the overall system mass. Finally, the mass of the HEXs and the corresponding working fluid inventory are obtained by solving the preliminary sizing procedure for each of the heat transfer devices.

HEX SIZING

HEX sizing is performed by means of an in-house Python tool named HeXacode [4], whose accuracy has been previously verified against results from a commercial software [17]. The tool relies on empirical correlations for the Nusselt number and friction factor, as listed in Ref. [4], to model the thermohydraulic characteristics of HEXs. The sizing procedure aims at determining the heat transfer area ($A_{\rm ht}$) needed to achieve the desired heat duty (\dot{Q}) for given inlet temperatures, pressures, and mass flow rates of the cold and hot streams. To account for the variation in thermodynamic properties and, consequently, in the heat transfer coefficients along the flow path, the HEX geometry is discretized into a few control volumes. The solution of the preliminary design involves an iterative computation of the heat transfer area in each control volume using the relation

$$A_{\rm ht}^i = \frac{\dot{Q}^i}{F^i \Delta T_{\rm ml}^i U^i} \tag{4.2}$$

where $\Delta T_{\rm ml}^i$ is the mean logarithmic temperature difference in cell i, F^i is its correction factor and U^i is the local overall heat transfer coefficient. For the specific condenser topology considered in this study, the HEX frontal area represents a design input, and the output of the sizing procedure is the depth along the cooling air flow path, or equivalently the number of tubes in the streamwise direction (n_z) . Additional model outputs include the HEX mass and the pressure drops across the HEX for both streams. For more details about HeXacode and the solution procedure to size tube bundle HEXs, the reader is referred to Ref. [18].

4.3.2. Numerical model for CFD-based shape optimization

The numerical models and methods utilized for this study are similar to those reported in Chapter 2. The air-side flow across the tube bundle forming the condenser is simulated using the SU2 solver for incompressible flows based on RANS with the Spalart-Allmaras

turbulence model. The working fluid side of the condenser is not included in the simulation domain. An isothermal wall boundary condition is imposed on the outer surface of the tubes, with the wall temperature set equal to the condensation temperature of the working fluid. The inlet boundary conditions, specifically temperature and velocity, are prescribed based on the results from the HEX sizing model, while 0 Pa gauge pressure is imposed on the outlet boundary. To further reduce the computational burden of the simulations, the airflow through the tube bundle is modeled as a two-dimensional channel flow. Geometric symmetry in the bare-tube bundle configuration is also exploited to minimize the size of the computational domain. The fluid properties are assumed to be constant, with their values evaluated at the average bulk temperature of the fluid estimated in the preliminary sizing procedure. The steady-state solution is achieved by means of a time-marching scheme with Euler implicit time integration, and the flow simulations were terminated after residual reductions of more than 5 orders of magnitude.

4.3.3. OPTIMIZATION PROBLEMS

The objectives of the system optimization are to minimize the mass of the ORC unit and to maximize its net power output, while satisfying the constraint on the working fluid pressure drop ($\Delta P_{\rm wf}$) and the bounds imposed on the design variables. The optimization problem is thus formulated as

$$\min_{\boldsymbol{\alpha}_{\text{sys}}} -\dot{W}_{\text{net}}(\boldsymbol{\alpha}_{\text{sys}}), M_{\text{ORC}}(\boldsymbol{\alpha}_{\text{sys}}), \tag{4.3}$$

subject to
$$\Delta P_{\text{wf}} \le 0.03 P_{\text{wf,in}},$$
 (4.4)

$$\alpha_{\text{sys},L} \le \alpha_{\text{sys}} \le \alpha_{\text{sys},U},$$
 (4.5)

where $\alpha_{\rm sys}$ represents the system design variables, $P_{\rm wf,in}$ is the inlet pressure of the working fluid. The system design variables include the minimum ($T_{\rm min,ORC}$) and maximum ($T_{\rm max,ORC}$) working fluid temperatures, the maximum cycle pressure ($P_{\rm max,ORC}$), the evaporator and the condenser pinch point temperature differences ($\Delta T_{\rm pp,evap}$, $\Delta T_{\rm pp,cond}$), along with the geometric parameters of the condenser, namely the tube outer diameter (d_0), longitudinal and transverse pitch ratios (x_1 , x_t), and the aspect ratio (AR) of the frontal area. The lower and upper bounds for the design variables $\alpha_{\rm sys}$ are provided in Table 4.2 and Table 4.3. The multi-objective system design problem is solved using the NSGA-II [19] optimization algorithm implemented in the Python library pymoo [20]. The initial population size is set to eight times the number of design variables. Moreover, the optimization process is run for a generation count equal to approximately ten times the number of design variables to ensure adequate convergence.

Table 4.2: Design variables associated with the WHR unit system model and corresponding bounds in the optimization.

Parameter	$T_{ m min,ORC}$ [K]	T _{max,ORC} [K]	$P_{ m max,ORC}$ [bar]	$\Delta T_{ m pp,evap}$ [K]	$\Delta T_{ m pp,cond}$ [K]
Min	367	517.12	47.4	10	10
Max	378	547.84	67.7	50	50

Table 4.3: Condenser geometry parameters and corresponding bounds in the system optimization. The lower bound of the longitudinal pitch ratio x_l differs between the inline (i) and staggered (s) configurations, whereas all other bounds are identical for both layouts.

Parameter	d _o [mm]	<i>x</i> _l [-]	<i>x</i> _t [-]	AR [-]
Min	1.8	1.25 (i) 0.85 (s)	1.6	0.5
Max	2	3	3	

With respect to the shape optimization problem, the objective is to minimize the air-side pressure drop across the condenser, subject to a constraint on the minimum required heat transfer rate. The mathematical formulation of the optimization problem is formulated as follows

$$\min_{\boldsymbol{\alpha}_{\text{cfd}}} \quad \Delta P_{\text{air}}(\boldsymbol{\alpha}_{\text{cfd}}), \tag{4.6}$$

subject to
$$\dot{Q} \ge \dot{Q}_0$$
, (4.7)

$$a \ge a_0, \tag{4.8}$$

$$\alpha_{\text{cfd,L}} \le \alpha_{\text{cfd}} \le \alpha_{\text{cfd,U}}.$$
 (4.9)

Here, $\alpha_{\rm cfd}$ denotes the design variables of the shape optimization procedure, with subscripts L and U representing their respective lower and upper bounds. The term $\Delta P_{\rm air}$ refers to the air-side pressure drop, \dot{Q} is the heat transfer rate, and \dot{Q}_0 is the required heat transfer rate. a and a_0 correspond to the areas enclosed within each tube for the current and the baseline geometry, respectively. The shape optimization variables ($\alpha_{\rm cfd}$) include the CAD parameters controlling the thickness distributions ($t^{\rm u}$, $t^{\rm l}$) around the camber line, which thus determine the tube surface profiles. Sensitivities are averaged according to the CP-AS approach documented in Chapter 2, to obtain optimal tube geometries with identical and symmetric shapes. Finally, the optimization problem is solved by employing the SLSQP algorithm [21], accessed via the SciPy Python library [22].

4.4. RESULTS

4.4.1. SYSTEM OPTIMIZATION AND PARETO ANALYSIS

The system design results, obtained by solving the multi-objective optimization problem corresponding to Equation 4.3, are illustrated in Figure 4.4. A Pareto front is obtained for both the inline and staggered configurations considered for the condenser. It can be observed that the optimal solutions for the system adopting a condenser with an inline tube layout dominate those obtained in the case of a staggered tube bundle configuration if $\dot{W}_{\rm net} > 50$ kW. Conversely, the solutions corresponding to the staggered tube layout feature a lower system mass, albeit at the cost of higher pressure drop in the airflow across the condenser and, subsequently, of lower net power output of the ORC system. Moreover, the slopes of both Pareto fronts become steeper beyond a certain system power output, indicating that only marginal gains in power $\dot{W}_{\rm net}$ are achieved with significantly large increases in system mass.

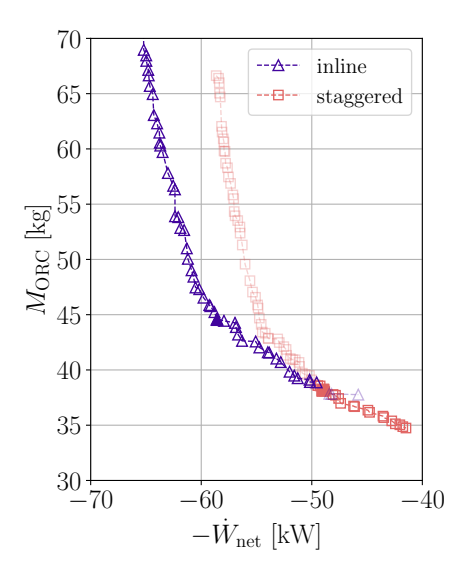


Figure 4.4: Pareto fronts illustrating the ORC WHR unit system design trade-offs for the inline and staggered condenser configurations. The optimal solutions selected using the epsilon-constraint method are marked with filled symbols.

The second step of the proposed methodology consists of selecting the most promising solutions identified through the multi-objective design optimization at the system level, followed by applying shape optimization to refine the condenser geometry and further improve performance. This selection is performed for both the Pareto sets plotted in Figure 4.4, using the so-called epsilon-constraint method [10, Ch. 9]. The relevant characteristics and model inputs corresponding to the two selected design options are reported in Table 4.4. The most promising solution in the case of a condenser with an inline tube configuration features an ORC system mass of approximately 45 kg, while that for the Pareto set related to the staggered arrangement yields a mass of around 39 kg. It is worth noting that the selected solution for the ORC system with a condenser adopting a staggered tube layout corresponds to the non-dominated point with the highest power output, whereas the chosen design option among those featuring a condenser with an inline tube layout lies on the Pareto front just before the sharp increase in its slope.

4.4.2. COMPARISON BETWEEN CFD AND LUMPED PARAMETER MODEL RESULTS

CFD simulations are performed for the condenser configurations corresponding to the two design points selected from the Pareto fronts in Figure 4.4. A grid independence study similar to the one documented in Chapter 2 is first performed to identify the most appropriate mesh size for the CFD simulations. Subsequently, the results obtained using the RANS-based CFD model are compared to the output of the empirical HEX model utilized to perform condenser sizing in the system design. This comparison is provided

Table 4.4: Main characteristics of the two ORC system design solutions selected as test cases for shape optimization of the condenser geometry.

Parameter	Description	Units	Inline	Staggered
$\dot{W}_{ m net}$	Net power output	kW	58.57	49.71
$\dot{W}_{ m fan}$	Fan power consumption	kW	3.32	7.39
$T_{ m min,ORC}$	Minimum temperature of ORC	K	370.65	377.81
$T_{ m max,ORC}$	Maximum temperature of ORC	K	532.33	530.22
$P_{ m max,ORC}$	Maximum cycle pressure	bar	53.02	54.96
$\Delta T_{ m pp,evap}$	Evaporator pinch point temperature difference	K	48.01	49.41
$\Delta T_{\rm pp,cond}$	Condenser pinch point temperature difference	K	32.71	34.84
$M_{ m ORC}$	Mass of the ORC system	kg	44.58	38.70
$M_{ m cond}$	Mass of the condenser	kg	13.36	9.28
$\dot{Q}_{ m cond}$	Condenser heat transfer rate	kW	298.27	295.92
$d_{ m o}$	Outer diameter of the condenser tubes	mm	1.839	1.840
x_{l}	Longitudinal pitch ratio	-	1.288	1.295
x_{t}	Transverse pitch ratio	-	2.878	2.919
AR	Aspect ratio	-	0.748	0.582
$n_{\rm z}$	Number of tubes in the streamwise direction	-	28	20

in Table 4.5, which lists the values of pressure drop and heat transfer rate, expressed in terms of temperature increase in the cooling airflow, obtained using the two modeling approaches for the condenser geometries corresponding to the selected design solutions, along with the relative differences between the two sets of predictions. For the condenser geometry with an inline tube layout, the CFD model predicts a pressure drop and heat transfer rate that are approximately 71% and 65% lower, respectively, than those estimated by the model for HEX preliminary sizing. Conversely, for the staggered tube condenser configuration, the pressure drop predicted by CFD simulations is about 40% higher than the estimate of the HEX lumped parameter model, while the heat transfer rate is underpredicted by 8%. Note that, based on the trends observed in the grid independence study, the discretization error with the selected mesh size is below 1% for the pressure drop and under 0.2% for the heat transfer rate. Furthermore, the uncertainty in the predictions of the HEX lumped parameter model is in the range of $\pm 15\%$. The results from CFD simulations corresponding to the two configurations are further discussed in the following.

INLINE TUBE CONFIGURATION

The values of tube pitch ratios lie close to the validity bounds of the empirical correlations used for predicting the heat transfer coefficients and friction factors, thereby increasing the uncertainty in the results. Nonetheless, the discrepancies in the estimated pressure drop and heat transfer rate between the lumped parameter model for HEX sizing and the CFD simulations are significantly larger than the uncertainty range expected for the two modeling approaches, suggesting potential limitations of the RANS model in accurately capturing flow characteristics throughout the tube bundle. This interpretation is supported by the analysis of the flow field obtained from the CFD simulations and by findings documented in the literature regarding flow and heat transfer in cylindrical tube banks.

The challenges faced by RANS turbulence models, such as the Spalart–Allmaras model, in accurately predicting flow separation, wake interactions, and turbulence intensities [23–26], are particularly evident for inline tube configurations.

Table 4.5: Comparison of pressure drop and cooling air temperature increase predicted by the CFD and the lumped-parameter HEX models for both the inline and staggered tube bundle condensers.

Case	ΔP _{cfd} [Pa]	ΔP _{hex} [Pa]	$% \operatorname{diff}_{\Delta P} = [-]$	$\Delta T_{ m cfd}$ [K]	$\Delta T_{ m hex}$ [K]	$\% \mathrm{diff}_{\Delta T}$ [-]
Inline	81.81	286.8	-71.47		32.48	-64.96
Staggered	1024.1	731.7	39.96		36.33	-8.25

Figure 4.5 displays the velocity and temperature fields obtained from the CFD simulations for an array of aligned tubes. It can be observed that only in the first tube row, which is directly exposed to the uniform approach flow, most of the wetted area is covered by attached flow. In contrast, as shown in Figure 4.6, the downstream tubes are primarily immersed in the recirculation zones that form in the gap between consecutive tubes.

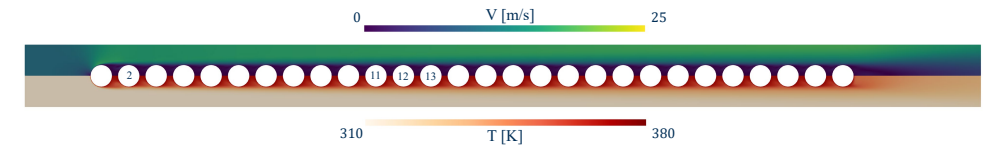


Figure 4.5: Velocity and temperature fields for the inline bare-tube condenser, with row numbers labeled on selected tube rows for reference.

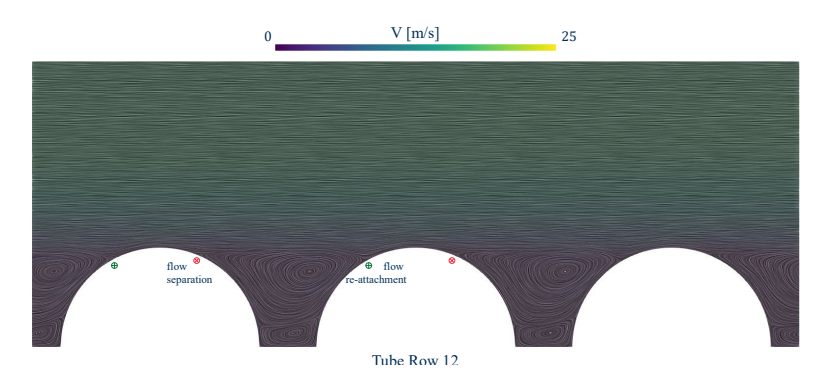


Figure 4.6: Velocity contours and flow streamlines around the 12th tube row of the inline bare-tube condenser. The flow separation re-attachment points are marked for tube rows 11 and 12.

This flow pattern in which most of the flow passes straight through the horizontal lanes defined by the tube arrays is commonly reported in the literature for inline tube bundles with a longitudinal pitch ratio (x_l) less than 2 [27]. For this characteristic, the flow in the region between the transverse spacing of the tubes is typically referred to as a jet-type bulk flow [28]. Moreover, from the second row onward, each tube is in the

wake or "shadow" of the one preceding it [29]. Therefore, the accurate prediction of flow separation, flow re-attachment (see Figure 4.6), turbulent mixing in the wake, and bulk mean velocity is essential for accurately estimating the overall heat transfer rate and total pressure losses in flows across inline tube bundles.

Most RANS-based studies in the literature that focused on predicting the characteristics of flows around inline tube arrays have relied on unsteady simulations (URANS) with turbulence models of various levels of complexity, achieving however inconsistent and generally unsatisfactory results [30]. The suitability of URANS for the simulation of flows around cylinders is arguable, as the equivalent Reynolds stresses introduced by the time averaging of the solution may dominate those associated with the turbulence model itself [24, 31]. Moreover, most turbulence models have been calibrated using stationary data and steady simulations, with the consequence that URANS models inherently overestimate the average drag or heat transfer coefficient compared to RANS simulations with the same turbulence model [32]. For inline tube bundles with x_1 less than 2, good agreement with experimental data has been reported in a few recent studies employing RANS solvers with modified versions of the k- ϵ turbulence model, such as the low-Re k- ϵ model by Lien et al. [33, 34] or the realizable k- ϵ model [35]. The higher accuracy observed for CFD simulations with the realizable k- ϵ model is arguably due to its suitability for jet-type flows [25]. However, before implementing an alternative turbulence model in SU2, its suitability for the current application must be thoroughly verified, for example, through comparison with higher fidelity CFD approaches, such as the detached eddy simulation (DES) method [36]. In any case, this activity falls outside the scope of the current study.

STAGGERED CONFIGURATION

The velocity and temperature fields obtained for the condenser configuration with staggered tubes are shown in Figure 4.7. It can be observed that the bulk flow is redirected by each tube row toward the tubes in the subsequent row, resulting in what is commonly referred to in the literature as a wavy flow pattern [29]. Heat transfer is enhanced compared to the inline configuration, as the flow remains attached over a larger portion of the wetted surface of the tubes. Additionally, the fluid temperature in the wake of the tubes is lower than in the case of an inline tube layout, thanks to the increased mixing occurring at the edges of the recirculation regions driven by the higher momentum of the deflected bulk flow. Steady RANS models have been reported in the literature to yield more accurate predictions of flow phenomena in staggered tube bundles [37]. This is reflected in the closer agreement between the outputs of the CFD and lumped parameter models as shown in Table 4.5. Based on these considerations, shape optimization is applied only to the test case of the condenser with a staggered tube layout.

4.4.3. Shape optimization and performance improvements at both condenser and system level

The trend of the cost functions with design iterations is displayed in Figure 4.8. The optimization process results in about a 24% reduction in the value of the air-side pressure drop in 12 design iterations. The computational time required for each flow and adjoint simulation was about 8 minutes using 54 cores and 27 GB of memory on a high-performance

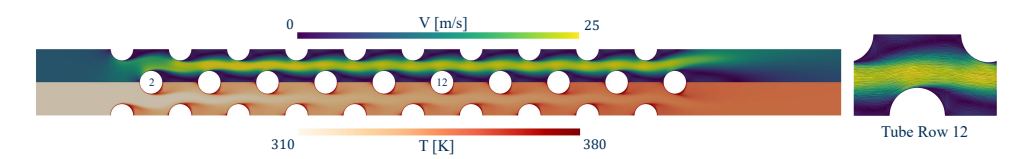


Figure 4.7: Velocity and temperature fields for the condenser with a staggered tube configuration, with row numbers labeled on selected tube rows for reference. The velocity field and flow streamlines around tube row 12 are displayed on the right.

computing platform equipped with Intel Xeon E5-2680v4 operating at 2.8 GHz.

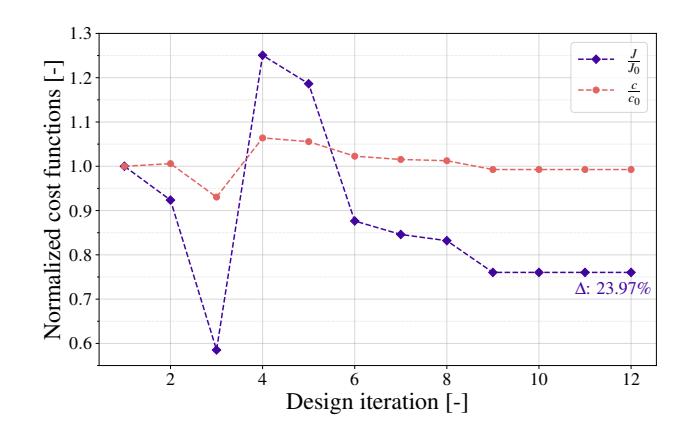


Figure 4.8: Optimization history depicting the trend of the cost functions normalized by their baseline values, i.e., those corresponding to the staggered configuration of the condenser geometry.

The velocity and temperature fields for the optimized geometry are depicted in Figure 4.9. The optimized design provides reduced flow blockage, resulting in lower velocity peaks and, consequently, decreased fluid-dynamic losses. Furthermore, in the fully developed region (12th tube row selected for analysis), as depicted in Figure 4.10, the flow remains attached over a larger portion of the wetted surface compared to the baseline geometry. This characteristic is reflected in the comparison of the pressure coefficient $(C_{\rm p})$ and the heat flux (q'') displayed in Figure 4.11. For the optimized tube profile, a large adverse pressure gradient develops only in the final quarter of the chord length, whereas in the baseline case, flow separation occurs at approximately half of the chord length. As a result, the region between the point of flow re-attachment (from the wake of the previous tube) and that of flow separation is larger and exhibits higher heat flux levels for the optimized tube shape. However, despite these local differences, the total heat transfer rate across the whole tube bundle remains comparable between the two geometries. Compared to the optimized geometries with identical tubes reported in Chapter 2, the shape obtained in this case study features a less slender profile and is broader at the leading and trailing edges. This difference is attributed to the influence of the baseline geometry, specifically the circular profile and the transverse pitch.

The 24% reduction in pressure drop in the cooling airflow enabled by the shape opti-

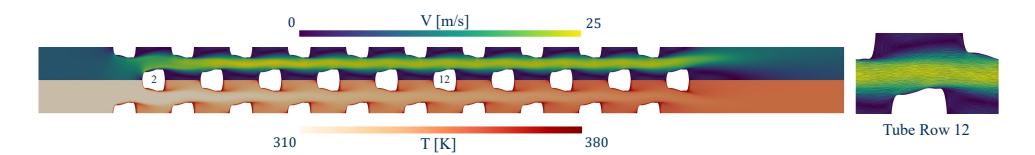


Figure 4.9: Velocity and temperature fields for the optimized condenser geometry, with row numbers labeled on selected tube rows for reference. The velocity field and the flow streamlines around the 12th tube row are displayed on the right.

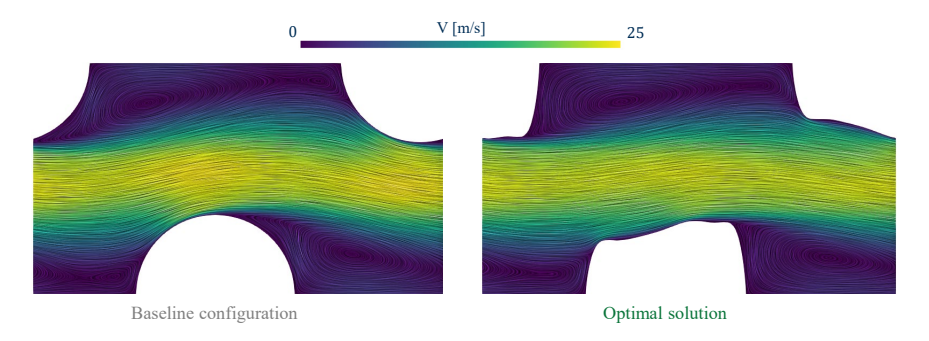


Figure 4.10: Comparison of velocity contours and flow streamlines around the 12th tube row between baseline and optimized geometries (staggered tube bundle configuration).

mization method corresponds to a decrease in the fan pumping power of about 1.8 kW. Since the heat transfer rate of the overall condenser and the flow area within the tubes remain essentially the same as those of the baseline design, this reduction in pumping losses directly translates into an increase in the net power output of the system, without any significant change in the mass of the ORC unit. Consequently, the optimized geometry yields about a 3.5% increase in net power output and an absolute gain of about 0.5 percentage points in ORC net efficiency. One could question the accuracy of the obtained performance gain, given the discrepancy between the HEX performance estimates from the system-level analysis and those obtained through CFD simulations (see Table 4.5). In this regard, it is important to highlight that the reduction in pressure drop obtained by shape optimization is estimated using a consistent modeling approach. Furthermore, RANS-based models are generally reliable in predicting relative changes in flow properties between design variants, even if the absolute values of their predictions may deviate significantly from experimental data or results from higher-fidelity simulations [38].

The obtained results thus demonstrate that optimizing heat transfer devices using the methodology proposed in this work can yield non-negligible improvements in system efficiency. Even larger performance gains are expected for the analyzed application if the pressure drop margin enabled by shape optimization is leveraged to redesign an ORC system recovering more thermal energy from the APU exhaust gases.

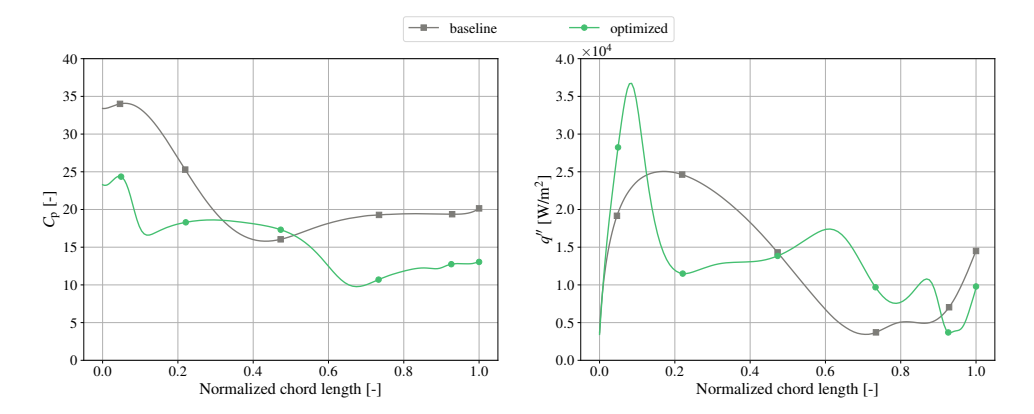


Figure 4.11: Comparison of pressure coefficient and heat flux distributions along tube surface for the baseline and optimum designs. The tube selected for the comparison is from the 12th row, where the flow is fully developed.

4.5. CONCLUSIONS

The aim of the research documented in this chapter was to explore the integration of CFD-based design methods with system-level preliminary design for energy conversion systems in which HEXs are critical components. In particular, two optimization problems are solved: a system-level optimization using a gradient-free genetic algorithm, with design variables including the thermodynamic cycle parameters and those defining the HEX geometry; and shape optimization based on the adjoint method at the component level to reduce fluid dynamic losses in the HEX. In this second optimization problem, the design variables are the CAD inputs that control the NURBS curves representing the HEX geometry. The proposed methodology was applied to design an ORC system for waste heat recovery from an aircraft APU. The ORC condenser consists of a bundle of circular bare tubes arranged either in an inline or staggered configuration. As the first step of the design methodology, the condenser preliminary design is optimized concurrently with the thermodynamic cycle process variables. The resulting geometry is then further refined using adjoint-based shape optimization.

The key outcomes of this study can be summarized as follows:

- The Pareto front obtained from the multi-objective system design of the ORC unit shows that condenser designs with an inline tube configuration enable higher system power output, while those with a staggered configuration should be preferred if system mass is to be minimized.
- 2. Two design points on the Pareto fronts were selected, one for each condenser tube arrangement, to evaluate the performance enhancement achievable by applying shape optimization to the design of the condenser. To this end, a RANS-based CFD model was implemented for both tube bundle layouts. For the inline configuration, significant discrepancies emerged between the CFD predictions and the results from the lumped parameter model used for HEX preliminary design. This can be

attributed to the inherent limitations of RANS models in accurately capturing the flow physics observed in inline tube bundles.

- 3. Shape optimization was performed only for the condenser with a staggered tube configuration with the objective of reducing the air-side pressure drop while constraining the heat transfer rate and internal area of the cross-section of the tubes at the same values as the baseline design. The resulting optimal solution leads to a pressure drop reduction of about 24%.
- 4. By adopting the condenser geometry obtained through shape optimization, the net power output of the ORC WHR unit could be increased by about 1.8 kW or 3.5% with no apparent increase in the system mass.

This study represents an initial step toward enhancing the performance of energy conversion systems through the application of adjoint-based shape optimization to the design of HEXs. Future work will be devoted to establishing a two-way coupling between the system-level design and shape optimization methods, to leverage improvements in HEX performance enabled by unconventional heat transfer geometries and further enhance overall system design. Moreover, to increase confidence in the estimation of the performance gains, future work should include simulations with higher fidelity models, such as DES, along with a multi-fidelity uncertainty quantification to assess the impact of model inconsistencies and approximations in the information transfer between the different models of the whole design chain.

BIBLIOGRAPHY

- [1] D. Krempus, "Organic Rankine Cycle Waste Heat Recovery Systems for Aircraft Engines", Ph.D. dissertation, Delft University of Technology, 2025. DOI: 10.4233 /UUID:5E565F99-A9F4-4208-95E9-2C542FD720F8.
- [2] J. V. Vargas and A. Bejan, "Integrative thermodynamic optimization of the environmental control system of an aircraft", *International Journal of Heat and Mass Transfer*, vol. 44, no. 20, pp. 3907–3917, 2001, ISSN: 0017-9310. DOI: 10.1016/S0017-9310(01)00033-3.
- [3] J. Guo and X. Huai, "Optimization design of heat exchanger in an irreversible regenerative Brayton cycle system", *Applied Thermal Engineering*, vol. 58, no. 1, pp. 77–84, 2013, ISSN: 1359-4311. DOI: 10.1016/j.applthermaleng.2013.03.0 61.
- [4] F. Beltrame, D. Krempus, P. Colonna, and C. De Servi, "Reduced order modelling of optimized heat exchangers for maximum mass-specific performance of airborne ORC waste heat recovery units", in *Proceedings of the 7th International Seminar on ORC Power Systems*, International Seminar on ORC Power Systems, Seville, Spain, 2023.
- [5] F. Ascione, P. Colonna, and C. De Servi, "Integrated design optimization method for novel vapour-compression-cycle-based environmental control systems", *Applied Thermal Engineering*, vol. 236, p. 121 261, 2024, ISSN: 1359-4311. DOI: 10.1016/j.applthermaleng.2023.121261.
- [6] M. El-Soueidan, M. Schmelcher, J. Häßy, and A. Görtz, "The Coupling of a Preliminary Design Method With CFD Analysis for the Design of Heat Exchangers in Aviation", in AIAA AVIATION FORUM AND ASCEND 2024, Las Vegas, Nevada, United States, 2024, p. 4036.
- [7] D. Misirlis *et al.*, "Optimization of heat exchangers for intercooled recuperated aero engines", *Aerospace*, vol. 4, no. 1, 2017, ISSN: 2226-4310. DOI: 10.3390/aerospace 4010014.
- [8] K. Sbutega, D. Geb, and I. Catton, "Modeling of multiscale heat transfer systems using volume averaging theory", in *Advances in Heat Transfer*. Elsevier, 2015, pp. 1–165. DOI: 10.1016/bs.aiht.2015.08.001.
- [9] E. J. Adler, A. H. R. Lamkin, and J. R. R. A. Martins, "Aircraft Ducted Heat Exchanger Aerodynamic Shape and Thermal Optimization", *ASME Journal of Heat and Mass Transfer*, vol. 147, no. 1, Jan. 2025, ISSN: 2832-8469. DOI: 10.1115/1.4066438.
- [10] J. R. R. A. Martins and A. Ning, Engineering Design Optimization. Cambridge, UK: Cambridge University Press, Jan. 2022, ISBN: 9781108833417. DOI: 10.1017/97811 08980647.

96 BIBLIOGRAPHY

[11] T. D. Economon, F. Palacios, S. R. Copeland, T. W. Lukaczyk, and J. J. Alonso, "SU2: An open-source suite for multiphysics simulation and design", *AIAA Journal*, vol. 54, no. 3, pp. 828–846, 2016. DOI: 10.2514/1.J053813.

- [12] T. D. Economon, "Simulation and adjoint-based design for variable density incompressible flows with heat transfer", *AIAA Journal*, vol. 58, no. 2, pp. 757–769, 2020, ISSN: 00011452. DOI: 10.2514/1.J058222.
- [13] A. B. Lambe and J. R. R. A. Martins, "Extensions to the Design Structure Matrix for the Description of Multidisciplinary Design, Analysis, and Optimization Processes", *Structural and Multidisciplinary Optimization*, vol. 46, pp. 273–284, 2012. DOI: 10.1007/s00158-012-0763-y.
- [14] I. H. Bell, J. Wronski, S. Quoilin, and V. Lemort, "Pure and pseudo-pure fluid thermophysical property evaluation and the open-source thermophysical property library coolprop", *Industrial & Engineering Chemistry Research*, vol. 53, no. 6, pp. 2498–2508, Jan. 2014, ISSN: 1520-5045. DOI: 10.1021/ie4033999.
- [15] M. van der Geest, H. Polinder, J. A. Ferreira, and M. Christmann, "Power density limits and design trends of high-speed permanent magnet synchronous machines", *IEEE Transactions on Transportation Electrification*, vol. 1, no. 3, pp. 266–276, Oct. 2015, ISSN: 2332-7782. DOI: 10.1109/tte.2015.2475751.
- [16] H.-D. Kwak, S. Kwon, and C.-H. Choi, "Performance assessment of electrically driven pump-fed LOX/kerosene cycle rocket engine: Comparison with gas generator cycle", *Aerospace Science and Technology*, vol. 77, pp. 67–82, 2018, ISSN: 1270-9638. DOI: 10.1016/j.ast.2018.02.033.
- [17] GRETh, *Echtherm*, version 3.2, 2023.
- [18] F. Beltrame, "On the preliminary design of aerospace-grade compact heat exchangers: From ram air cooling ducts to energy harvesting systems", Ph.D. dissertation, Delft University of Technology, 2026.
- [19] K. Deb, A. Pratap, S. Agarwal, and T. Meyarivan, "A fast and elitist multi-objective genetic algorithm: NSGA-II", English, *IEEE Transactions on Evolutionary Computation*, vol. 6, no. 2, pp. 182–197, Apr. 2002. DOI: 10.1109/4235.996017.
- [20] J. Blank and K. Deb, "Pymoo: Multi-objective optimization in python", IEEE Access, vol. 8, pp. 89 497–89 509, 2020, ISSN: 2169-3536. DOI: 10.1109/access.2020.299 0567.
- [21] D. Kraft, "A software package for sequential quadratic programming", DLR German Aerospace Center, Institute for Flight Mechanics, Koln, Germany, Tech. Rep. DFVLR-FB 88-28, 1988.
- [22] P. Virtanen *et al.*, "SciPy 1.0: Fundamental Algorithms for Scientific Computing in Python", *Nature Methods*, vol. 17, pp. 261–272, 2020. DOI: 10.1038/s41592-019-0686-2.
- [23] D. C. Wilcox, *Turbulence Modeling for CFD*, 3rd. DCW Industries, Inc., 2006, ISBN: 978-1-928729-08-2.

BIBLIOGRAPHY 97

[24] P. Spalart, "Strategies for turbulence modelling and simulations", *International Journal of Heat and Fluid Flow*, vol. 21, no. 3, pp. 252–263, 2000, ISSN: 0142-727X. DOI: 10.1016/S0142-727X(00)00007-2.

- [25] T. H. Shih, W. W. Liou, A. Shabbir, Z. Yang, and J. Zhu, "A new k– ε eddy-viscosity model for high reynolds number turbulent flows: Model development and validation", *Computers & Fluids*, vol. 24, no. 3, pp. 227–238, 1995. DOI: 10.1016/0045-7930(94)00032-T.
- [26] J. L. Blackall, H. Iacovides, and J. C. Uribe, "Modeling of in-line tube banks inside advanced gas-cooled reactor boilers", *Heat Transfer Engineering*, vol. 41, no. 19–20, pp. 1731–1749, Aug. 2019, ISSN: 1521-0537. DOI: 10.1080/01457632.2019.16404 86.
- [27] S. Ishigai and E. Nishikawa, "Structure of gas flow and its pressure loss in tube banks with tube axes normal to flow", *Transactions of the Japan Society of Mechanical Engineers*, vol. 43, no. 373, pp. 3310–3319, 1977, ISSN: 2185-9485. DOI: 10.1299/ki kai1938.43.3310.
- [28] M. Zdravkovich, *Flow Around Circular Cylinders: Volume 2: Applications.* OUP Oxford, 1997, ISBN: 9780198565611.
- [29] A. Zukauskas and R. Ulinskas, *Heat transfer in tube banks in crossflow*. Hemisphere Publishing, New York, NY, Jan. 1988.
- [30] A. West, "Assessment of computational strategies for modelling in-line tube banks", English, Ph.D. dissertation, The University of Manchester, United Kingdom, Sep. 2013.
- [31] A. Travin, M. Shur, P. Spalart, and M. Strelets, "On URANS solutions with LES-like behaviour", in *Proceedings of the ECCOMAS 2004 European Congress on Computational Methods in Applied Sciences and Engineering*, Jyväskylä, Finland, Jul. 2004.
- [32] P. A. Durbin, "Separated flow computations with the k-epsilon-v-squared model", *AIAA Journal*, vol. 33, no. 4, pp. 659–664, Apr. 1995, ISSN: 1533-385X. DOI: 10.2514/3.12628.
- [33] F. Lien, W. Chen, and M. Leschziner, "Low-reynolds-number eddy-viscosity modelling based on non-linear stress-strain/vorticity relations", in *Engineering Turbulence Modelling and Experiments*. Elsevier, 1996, pp. 91–100, ISBN: 9780444824639. DOI: 10.1016/b978-0-444-82463-9.50015-0.
- [34] L. B. Carasik, D. R. Shaver, J. B. Haefner, and Y. A. Hassan, "Steady RANS methodology for calculating pressure drop in an in-line molten salt compact crossflow heat exchanger", *Progress in Nuclear Energy*, vol. 101, pp. 209–223, Nov. 2017, ISSN: 0149-1970. DOI: 10.1016/j.pnucene.2017.07.017.
- [35] G. O. Bociar, "Challenges in the adjoint-based optimization of bare tube heat exchangers", Master's thesis, Delft University of Technology, Delft, The Netherlands, 2025.

98 BIBLIOGRAPHY

[36] A. Travin, M. Shur, M. Strelets, and P. Spalart, "Detached-eddy simulations past a circular cylinder", *Flow, Turbulence and Combustion*, vol. 63, no. 1–4, pp. 293–313, Jan. 2000, ISSN: 1573-1987. DOI: 10.1023/a:1009901401183.

- [37] R. Deeb, "Numerical analysis of the effect of longitudinal and transverse pitch ratio on the flow and heat transfer of staggered drop-shaped tubes bundle", *International Journal of Heat and Mass Transfer*, vol. 183, p. 122123, Feb. 2022, ISSN: 0017-9310. DOI: 10.1016/j.ijheatmasstransfer.2021.122123.
- [38] R. H. Bush, T. S. Chyczewski, K. Duraisamy, B. Eisfeld, C. L. Rumsey, and B. R. Smith, "Recommendations for Future Efforts in RANS Modeling and Simulation", in *AIAA Scitech 2019 Forum*, American Institute of Aeronautics and Astronautics, Jan. 2019. DOI: 10.2514/6.2019-0317.

CONCLUSIONS AND OUTLOOK

This dissertation documented an optimization framework for the design of thermal components based on the discrete adjoint method and CAD parameterization. The method developed as part of this research, based on the open-source CFD software SU2, has been demonstrated to be effective for thermal-hydraulic design of next-generation heat exchangers and heat sinks.

Based on the results documented in this dissertation, the following key conclusions can be drawn.

- Using the proposed design method, significant performance gains in terms of pressure drop reduction and heat transfer coefficient enhancement can be achieved with shape optimization compared to the conventional geometries (such as cylindrical tubes and pin fins) that are currently used in thermal components. Based on the results of two-dimensional shape optimization, it can be estimated that the pressure losses in condensers, evaporators, or radiators can be reduced by about 20-25% while maintaining the original heat transfer rate. With three-dimensional shape optimization methods, instead, the heat transfer coefficient in pin-fin heat sinks can be enhanced by about 25% and the pressure losses can be concurrently decreased by up to 20%. Therefore, future applications of this method can lead to high-performance aerospace-grade HEX with lower weight/volume and reduced drag/pumping losses.
- The proposed shape optimization method enables the concurrent design of multiple heat transfer surfaces with each of them featuring a different geometry (labelled CP-LS). This can lead to higher performance improvements as compared to a method in which the heat transfer surfaces are optimized with averaged sensitivity such that they retain an identical shape (labelled CP-AS). The reason thereof is related to the capability of the CP-LS method to optimize a heat transfer surface according to the local flow characteristics. However, some disadvantages could also arise: the CP-LS method can converge to local minima, resulting in sub-optimal HEX performance compared to that achieved with the CP-AS method. An effective strategy to circumvent the issue is to execute the two methods in sequence, and initialize the optimization with the CP-LS method with the solution from the CP-AS one.
- The CAD-based parametrization method typically used for the design optimization of turbomachinery blades is applicable to geometries of heat exchangers. This research has shown that the camber-thickness parametrization method can be effectively adopted to parametrize the primary surface of heat exchangers, such as tubes, as well as secondary surfaces, e.g., pin-fins. This NURBS-based geometry modeling facilitates smooth surfaces with G2-continuity and convenient imposition of geometric constraints. While such a method can be easily adapted to parametrize blades in axial, radial, and mixed flow turbomachines, the development of a unified CAD-based parametrization method that can be effortlessly tailored to optimize a wide variety of HEX geometries (e.g., offset strip-fins, wavy fins, louvered fins, etc.) is challenging and requires extensive implementation effort.
- Shape optimization for heat transfer problems can lead to large surface defor-

mations, which make the concurrent optimization of multiple design surfaces challenging. The key challenge is in preserving a reasonably good mesh quality during the design iterations. The mesh deformation algorithm used in this study, based on a linear elasticity method, was found to be a limiting factor in obtaining HEX geometries of unconventional shape. Suitable bounds on the design variables and geometric constraints were therefore imposed to avoid issues with the convergence of the CFD solver due to poor mesh quality.

The application of CFD-based HEX optimization in combination with system-level design can lead to significant improvements in overall system performance. In this research, a preliminary assessment of this integrated method was conducted for the test case of an ORC system designed for heat recovery from an aircraft auxiliary power unit. Due to the high computational cost involved, a one-way coupling strategy was adopted: the shape optimization of the ORC condenser was performed after selecting a system design solution from the Pareto front in the space ORC system weight and power output. The shape optimization of the condenser resulted in a pressure drop reduction of about 25%, leading to a corresponding increase in the power output of the ORC unit of about 3.5%. Such an integrated design method - targeting either pressure loss reduction or enhancement of the heat transfer coefficient to minimize HEX mass - can offer more substantial benefits for other combined cycle engines, such as the WET engine, where HEXs can constitute roughly 50% of the mass of the propulsion system. Furthermore, a fully integrated design framework with a concurrent optimization of the system design variables and HEX geometry is expected to yield even greater performance gains.

The outcomes of this work demonstrated the potential of adjoint-based shape optimization for the automated design of high-performance thermal components. Further developments of the method can make it industrially-strength, namely applicable to complex cases of industrial relevance. This will facilitate the design of novel aerospace-grade HEXs, helping to make aviation carbon-neutral. Since heat transfer devices are also key in the production process of carbon-neutral fuels, namely hydrogen and sustainable aviation fuels, as well as in many other industrial processes, the impact of advance design methods for HEXs in the pursuit of sustainability and decarbonization is arguably even larger than explored in this research.

OUTLOOK

The research conducted in this work has led to an improved understanding of the strengths and limitations of adjoint-based design methods based on CAD parameterization for heat transfer problems. Based on the lessons learned, the following directions are recommended for future research.

The performance evaluations reported in this work were conducted using a CFD model based on RANS. To verify the performance gains achieved using optimized geometries, higher fidelity models such as those based on detached eddy simulations (DES) need to be utilized. In SU2, the implementation of DES, i.e., a hybrid RANS-LES model, is available, where the near-wall flow modeling in the RANS

counterpart is based on the SA turbulence model, the same as that used in this work. A study based on DES on 3D geometries obtained from optimized pin profiles will serve to verify the accuracy of the RANS model, therefore of the design method, and will provide greater insights into the flow physics. Moreover, the recent advent of highly scalable GPU-based CFD tools like *Luminary* could pave the way to computations of the flow within the whole heat exchanger, deepening the understanding of loss and heat transfer mechanisms in these components. Furthermore, experimental validation needs to be performed. Facilities such as the *IRIS* at TU Delft or the one currently being developed at *EnergyVille* could be used for the measurements of pressure drop and temperature increase across heat exchangers designed with the automated design method.

- To apply the design method to a wide variety of heat exchanger configurations, the capability of the CAD parametrization tool needs to be extended. For example, geometries such as offset strip-fins, plate-fins, wavy fins, etc., cannot be parametrized using the camber-thickness parametrization used in the present work. Open-source tools such as the *OpenCascade* CAD kernel or that of *OpenVSP* may be utilized for the parametrization of different HEX geometries and integrated into the design chain. Considering the required development time, the benefits of CAD parametrization compared to FFD for a selected range of geometries should be investigated. Furthermore, it could be beneficial to develop a hybrid parametrization based on a combination of CAD and FFD for optimization of different heat transfer geometries within a HEX. For example, the framework of hierarchical FFDs available in the open-source tool *pyGeo* can be utilized to develop hybrid FFD-CAD parametrization methods. Such a hybrid parametrization would provide the benefits of convenient imposition of geometric constraints for geometries with CAD parametrization and a larger design freedom for those using FFD.
- Due to the large surface deformations obtained in the shape optimization of heat transfer applications, the development of a more effective re-meshing strategy should be prioritized. Improvements in mesh quality are expected using a more sophisticated mesh deformation algorithm, such as that based on Radial Basis Functions. There are ongoing efforts in the SU2 community for the integration of such a mesh deformation algorithm, which can then be applied to HEX configurations. For cases involving a large number of mesh cells, it would be beneficial to benchmark such a tool with alternatives such as *IDWarp*, which is based on an efficient analytic inverse-distance method. Additionally, future studies could also focus on identifying the conditions requiring mesh regeneration instead of mesh deformation. As an example, along with criteria based on mesh-quality metrics such as skewness, one criterion could be based on the variation of the sensitivity of the cost functions with mesh density. Furthermore, sophisticated mesh generation algorithms such as those utilizing deep reinforcement learning (DRL) coupled with CAD parametrization may be incorporated for automated mesh generation. A DRLbased method coupled with the camber-thickness CAD parametrization has been recently applied for automated mesh generation of computational domains around a single turbomachinery blade, and it needs to be extended to multiple design

surfaces, targeting HEX applications. These meshing deformation/regeneration algorithms could also be exploited for optimizing the HEX topology.

- The surface characteristics of geometries produced by AM-based methods are known to augment the heat transfer coefficient and friction factor compared to smooth surfaces. This effect should be taken into account in the design chain. Surface roughness is typically modeled by equivalent sand-grain thickness in CFD models utilizing wall functions. In shape optimization studies where the flow near the walls is resolved, further investigations are necessary to identify suitable models for incorporating the effect of non-smooth surface characteristics. For example, the SA turbulence model in SU2 can be extended to account for wall roughness based on the modifications to the SA model proposed by Aupoix and Spalart, and its suitability for HEX design needs to be investigated.
- To fully integrate adjoint-based shape optimization in the system-level design, it would be beneficial to perform a multi-fidelity uncertainty quantification of the predictions of the different models adopted for system simulation and component design. For example, a Gaussian process model can be applied to assess the discrepancy between the output of thermal-hydraulic performance computed by the RANS model and that estimated by an empirical model. Furthermore, response surface models can be used to map the performance improvements that can be obtained from shape optimization to the design points on the Pareto front obtained from the system-level study. Additionally, it could be of great interest to evaluate suitable optimization algorithms such as gradient-enhanced multi-fidelity Bayesian optimization.
- Achieving an industrially-strength method requires several further developments. For example, the robustness of the CHT solver in SU2 must be improved, which is especially critical for cases with variable thermo-physical properties of the fluid and for cases with higher Biot numbers (Bi>0.1). This can be achieved by utilizing suitable coupling conditions, such as the Robin-Robin boundary condition, and an improved solution method for the coupled system, such as the quasi-Newton method. In addition, incorporating AM-specific constraints and structural analysis in the optimization loop will make the method more suited to handle industrial test cases relevant to carbon-neutral aviation.



SOFTWARE

The software applied or extended as part of the research documented in this dissertation is as follows:

- **Parablade**: A Python-based tool for surface parametrization and optimization. The version of the code developed and extended as part of this work in the ESCO group at VITO may be accessed upon request to Dr. Nitish Anand¹.
- **SU2**: An open-source suite for multi-physics simulation and design, written in C++ and available at https://github.com/su2code. The versions of the code used in this work was the master branch of v7.5.0 (for Chapter 2) and v8.0.1 (for Chapters 3 and 4).
- Python-based software for preliminary HEX design (*HeXacode*) and thermodynamic cycle calculations (*pycle*) utilized in Chapter 4 of this dissertation were developed by members of the Propulsion & Power group and may be accessed upon request to Dr. Carlo De Servi².

¹nitish.anand@vito.be

²c.m.deservi@tudelft.nl

ACKNOWLEDGEMENTS

The journey of the past years that led to this dissertation fills me with gratitude towards all those who supported me along the way.

I am deeply grateful to my supervisors for their guidance, which played the most significant role in my development as a researcher. I would first like to thank my promotor, Matteo Pini, for his encouraging and inspiring feedback, timely and appropriate advice, direct mentoring in academic writing, and valuable guidance for both professional and personal growth. I am grateful to my co-promotor, Carlo De Servi, for initiating the possibility of pursuing this PhD and for his support, patience, and technical guidance throughout the process. I would like to thank Nitish Anand, my supervisor at VITO, for facilitating my development and for the many valuable introductions and experiences, from my first introduction to Delft and the AE faculty to training in software development, SU2, and Parablade. I am also grateful to my doctoral committee members who took the time to evaluate my dissertation and provided valuable feedback.

The opportunity to pursue and complete this PhD would not have been possible without the support of my program managers at VITO: Ann Wouters and Frank Stals. I am deeply grateful to my VITO colleagues from the ESCO and THES teams for playing an enriching part in this journey. Special thanks to Geert Buckinx for translating my summary to Dutch as well as for all the conversations, technical discussions, and learnings. I am also grateful to Johan Van Bael, Sanjay Vermani, and Francesco Tosto for all the exchanges during meetings and fun times beyond. Thanks to Francesco for also patiently answering my questions related to entropy generation and those related to the formalities of TU Delft graduate school.

My time at TU Delft was very memorable, mainly thanks to the people who made it so, even in the short period I was able to spend there. I would like to express my deep gratitude to Piero Colonna for being my guide in the initial years and for always motivating and inspiring me in professional and personal development. I am grateful to Fabio Beltrame for all the technical discussions over the years as my immediate colleague in Delft, as well as for the conversations and the tennis sessions. I would like to thank Octavian Bociar for the collaboration during his master's thesis, which greatly contributed to my learning and development. Over the years, I got to meet wonderful folks at TU Delft, particularly Matteo Majer, Floyd van Steen, Gioele Ferrante, Alessandro Porcarelli, Evert Bunschoten, Dabo Krempus, and Alessandro Cappiello; and I am grateful to them for their kindness, enthusiasm, help, and patience on many occasions. I would also like to thank my colleagues at P&P and AE, particularly office roommates from LR6.01, who always made me feel welcome and shared enjoyable coffee breaks. I got to enjoy my time at Delft thanks to Ved Dubhashi for helping me with accommodation and for organizing meet-ups for badminton and Goan food.

Beyond my time at VITO and TU Delft, I owe much to my friends who made this journey fun and enjoyable. Apart from the wonderful times spent with TDA friends in

different parts of the world, I am particularly grateful to Ameya Patil for the weekly catchups, which led to the weekly accountability, motivation when needed, and a broader perspective. I would also like to thank Vijit Maithel for initiating the regular chats that transformed into a weekly planner with Patil. I am grateful to my friends from Zurich days, especially Prakhar Mehta, for being there to provide advice and help me navigate the journey. I am also grateful to my other friends from Zurich days for inspiring me with their PhD journeys and all the enjoyable times and trips. I am grateful to my friends from Hasselt, particularly Mohamed Yasko, for all the useful and useless conversations. I would like to thank my friends from Toastmasters Fonkse Leuven, particularly Tim 'T Joncke, for the fun times along with personal development. I am equally grateful to my tennis friends at Tenkie particularly Yuriy Vdovichenko for the matches and practices sessions that re-energized me throughout this journey.

I would also take this opportunity to thank my teachers who played an instrumental role in shaping my path. I am deeply grateful to Vyankatesh Prabhudesai sir for providing a glimpse into the world of engineering, for inspiring me, and for making me believe in myself. I am equally grateful to Ranjit Patil sir for introducing me to the world of CFD and heat transfer, and to MK Deshmukh sir for inspiring me to pursue graduate studies and a career in clean energy technologies. I also wish to express my sincere gratitude to my guides and collaborators at the wonderful institutions I have had the pleasure and privilege of being part of. Above all, I thank all my teachers whose guidance and teachings have eventually led to this dissertation.

Finally, I would like to thank my close and extended family for their support, patience, and understanding over the past years. I am especially grateful to Maushi, Kaka, and Kaki for their advice and voice of reason. And, most importantly, I am deeply grateful to my parents. Their unconditional love, patience, and belief in me have been my greatest source of strength that has sustained me through every challenge. This journey would not have been possible without their endless support, for which I remain deeply grateful.

CURRICULUM VITÆ

Praharsh Pravin PAI RAIKAR

Born on 27 May 1995 in Margao, Goa, India

EDUCATION

2021 – 2025	PhD in Aerospace Engineering Delft University of Technology, The Netherlands
2016 – 2018	Master of Science in Energy Science and Technology Eidgenössische Technische Hochschule (ETH) Zürich, Switzerland
2012 – 2016	B.E. (Hons.) in Mechanical Engineering Birla Institute of Technology & Science (BITS) Pilani, Goa Campus, India

WORK EXPERIENCE

10/2018 – present	R&D Professional Thermal Energy Systems
	VITO NV - Flemish Institute for Technological Research, Belgium
02/2018 - 09/2018	Research Student Empa - Swiss Federal Laboratories for Materials Science and Technology
	Empa - 5wiss rederal Eaboratories for Materials Science and reciniology
07/2017 - 12/2017	Intern
	Effin'Art, Switzerland
06/2016 - 08/2016	Research Associate
	Atal Bihari Vajpayee Institute of Good Governance & Policy Analysis, India
05/2015 - 08/2015	Mitacs Globalink Research Intern
	University of Waterloo, Canada
05/2014 – 07/2014	Project Trainee
	Tata Technologies, India

LIST OF PUBLICATIONS

JOURNAL ARTICLES

- 3. N. Anand, **P. Pai Raikar**, and C. De Servi, "Reduced-order turbulent flow solver to simulate streamwise periodic fins with iso-thermal walls", *International Journal of Heat and Mass Transfer* (in preparation).
- P. Pai Raikar, N. Anand, M. Pini, and C. De Servi, "3D optimization of heat sink fins using adjoint-based optimization with a CAD-based parametrization", *International Journal of Heat and Mass Transfer* 255 (2026) 127722.
 DOI: 10.1016/j.ijheatmasstransfer.2025.127722.
- P. Pai Raikar, N. Anand, M. Pini, and C. De Servi, "Concurrent optimization of multiple heat transfer surfaces using adjoint-based optimization with a CAD-based parametrization", International Journal of Heat and Mass Transfer 236 (2025) 126230.
 DOI:10.1016/j.ijheatmasstransfer.2024.126230

CONFERENCE PROCEEDINGS & PRESENTATIONS

- 4. **P. Pai Raikar**, F. Beltrame, N. Anand, M. Pini and C. De Servi, "Adjoint-based shape optimization of heat exchangers in the design airborne ORC waste heat recovery system", *Proceedings of ASME Turbo Expo 2026: Turbomachinery Technical Conference & Exposition*, Milan, Italy, June 2026 (in preparation).
- P. Pai Raikar, O. Bociar, C. De Servi, and N. Anand, "Shape and layout optimization of bare-tube heat exchangers using the adjoint method and CAD-based parametrization", Proceedings of the 9th International Conference on Experimental and Numerical Flow and Heat Transfer (ENFHT 2024), London, United Kingdom, April 2024.
 DOI: 10.11159/enfht24.219.
- 2. **P. Pai Raikar**, N. Anand, M. Pini, and C. De Servi, "CAD-based shape optimization of a pin-fin heat sink using the CHT solver in SU2", *4th SU2 Conference*, Varenna, Italy, October 2023.
- 1. **P. Pai Raikar**, N. Anand, C. De Servi, and M. Pini, "Adjoint-based shape optimization of mini-channel radiator tubes using a CAD-based parametrization", *ASME 2022 Summer Heat Transfer Conference (SHTC 2022)*, Philadelphia, United States of America, July 2022.

